Chapter 1

Introduction

Wave-formed rippled sediment beds are a common bottom feature of coastal seas in regions where there is relatively shallow water with large areas of non-cohesive, unvegetated sediments [*Ardhuin et al.*, 2002]. They are extremely important to the processes that act on or across the sediment-water interface as they change the pressure distribution, through flow separation and wake formation, within the bottom boundary layer. This differential pressure distribution across the ripple form acts to: increase the exchange of materials across the water sediment interface [*Jorgensen and Boudreau*, 2001]; enhance the entrainment of sediment into the water column by ejecting sediment from the bed [*Huettel and Webster*, 2001]; and amplify wave dissipation by increasing the hydraulic roughness of the seafloor [*Dade et al.*, 2001]. During each wave period two vortices are shed in the lee of the ripple crest (refer to Figure 1.1) which are then advected up into the water column [*Fredsoe et al.*, 1999]. This in turn increases the turbulence within the bottom flow regime and increases the overall thickness of the wave-boundary layer [*Nielsen*, 1992]. Hence the formation of ripples under the action of waves enhances the overall wave induced bottom mixing of a water body [*Grant and Madsen*, 1986].

Of major interest to coastal researchers is the effect wave-formed ripples have on the littoral transport system of a given coastline. Bottom friction and velocity profiles are strongly influenced by the size and spacing of bed roughness elements [*Drake and Cacchione*, 1986; *Grant and Madsen*, 1986], such as wave-formed ripples. The growth and erosion of rippled beds affects the littoral system by changing the volume of sediment

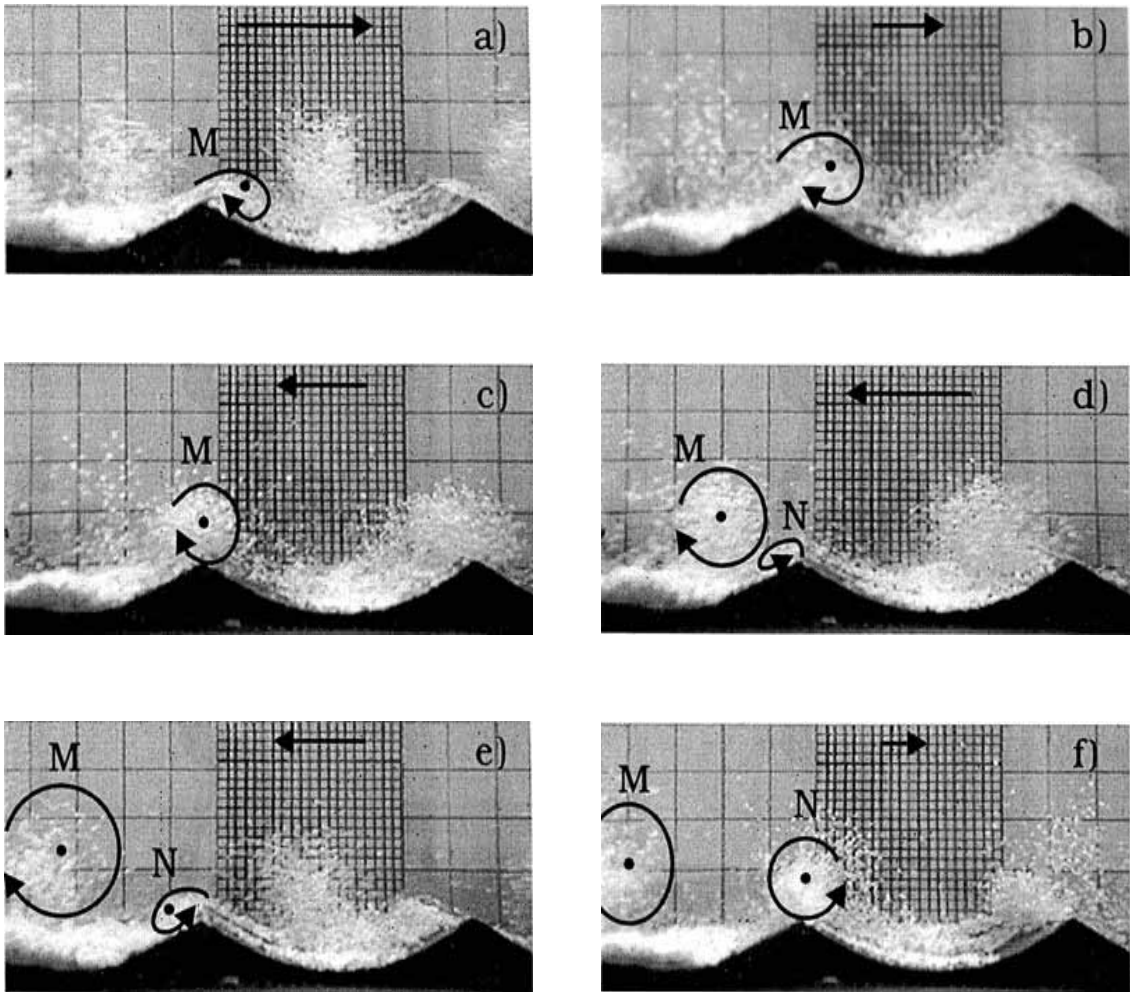

Figure 1.1 A sequence of photographs illustrating vortex shedding in the lee of ripple crests under wave induced motion. **Source:** *Fredsoe et al.* [1999]

being entrained into the water column each wave period and by changing wave energy levels impacting onto a coastline via an increase/decrease in the hydraulic roughness of the seafloor.

Ripples, by changing the hydraulic roughness of the seafloor, cause wave dissipation levels in shallow water to be dynamically linked to the surface wave conditions. As wave conditions increase from a calm period there is a corresponding increase in the hydraulic roughness of the seafloor due to the growth of rippled sediment beds [*Hay and Wilson*, 1994]. As the rippled bed grows there is an increase in both wave dissipation and sediment entrainment rates. This increase continues as wave conditions build; until a point is

reached when the volume of material being suspended by the waves, each period, causes the rippled bed to erode and upper plane bed (sheet flow) conditions to be established [*Wiberg and Harris*, 1994]. The erosion of the rippled bed results in a corresponding decrease in the hydraulic roughness of the seafloor. This in turn causes wave dissipation to decrease. Current theory suggests that rippled beds flatten during storms which will increase the wave energy impacting onto a coastline resulting in a possible elevation of erosion rates and storm damage.

A major complicating factor to account for the formation/erosion of wave-formed rippled beds in shallow water wave models is that ripples are highly irregular and dynamic. A large number of previous studies [*Amos et al.*, 1988; *Drake and Cacchione*, 1992; *Hay and Wilson*, 1994; *Wheatcroft*, 1994; *Bell and Thorne*, 1997; *Traykovski et al.*, 1999; *Hanes et al.*, 2001; *Doucette*, 2002; *Moore and Jaffe*, 2002; *Williams et al.*, 2004] have suggested that ripple parameters such as the height, length and ripple pattern can show quite substantial variation over small spatial and temporal scales under real field conditions. *Marsh et al.* [1999], based of the field work of *Vincent and Osborne* [1993], suggested that any change in ripple parameters requires the movement of a large quantity of sediment which requires significant energy and time.

This thesis presents the results of an experiential study which examined the variability and dynamic nature of rippled beds formed under an irregular surface wave field. The experimental results were utilised to develop a method to classify and predict rippled beds that are actively changing due to a change in the surface wave conditions. The method incorporates the spatial variability of the rippled field into the transient method through the use of the rippled bed's spectral density function.

1.1 RESEARCH BACKGROUND

This research has been funded by the Coast Protection Board of South Australia under the Australian Research Council's SPIRT scheme. The research was originally concerned with the modelling of waves in shallow water, specifically with the parameterisation of the bottom friction dissipation and the triad shallow water wave-wave interaction terms

in the coastal wave model SWAN [*Booij et al.*, 1999; *Ris et al.*, 1999]. However, after a substantial review of the current literature in regards to wave dissipation mechanisms due to bottom friction it was realised that the main area of inaccuracy was accounting for the highly dynamic nature of the bottom roughness height due to the formation/erosion of ripple beds in areas that have non-cohesive, un-vegetated sediment beds. Hence, the focus of the research was changed to the development a method to model these types of bed-forms.

Adelaide's metropolitan coastline extends some 26 km along the mid eastern coast of Gulf St Vincent (refer to Figure 1.2). Gulf St Vincent is a shallow water body with an average depth of 25 m and as shown in Figure 1.2, is largely protected from the extreme Southern Ocean swells by Yorke Peninsula to the west, Fleurieu Peninsula to the east and the land mass of Kangaroo Island to the south. The wave climate in the Gulf is mainly due to locally generated waves cause by local weather systems. Swell waves do pass into Gulf St Vincent through Investigator Straight and Backstairs Passage, but due to the relatively shallow depths in the Gulf the swell waves are quickly dissipated or refracted onto the southern coasts as they move north up the Gulf.

Adelaide's metropolitan coast had historically been protected by extensive seagrass meadows. However, since the 1930s there has been some 5,000 hectares of seagrass meadows lost along the metropolitan coastline. As the seagrass meadows have retreated large areas of the sandy seafloor have become exposed. Storms now impact the coastline with greater force and hence net erosion rates have increased dramatically over the last 70 years. The large scale loss of seagrass meadows has changed the hydraulic character of the seafloor from a relatively constant friction regime (seagrass canopy) to a dynamic friction regime (wave-formed ripples). Hence, the determination of the dynamic nature of ripples and wave dissipation rates is of interest of the Coast Protection Board and the coastal study group in the School of Civil and Environmental Engineering, The University of Adelaide, South Australia. This study focuses on the dynamic highly variable nature of ripple beds formed in coastal areas.

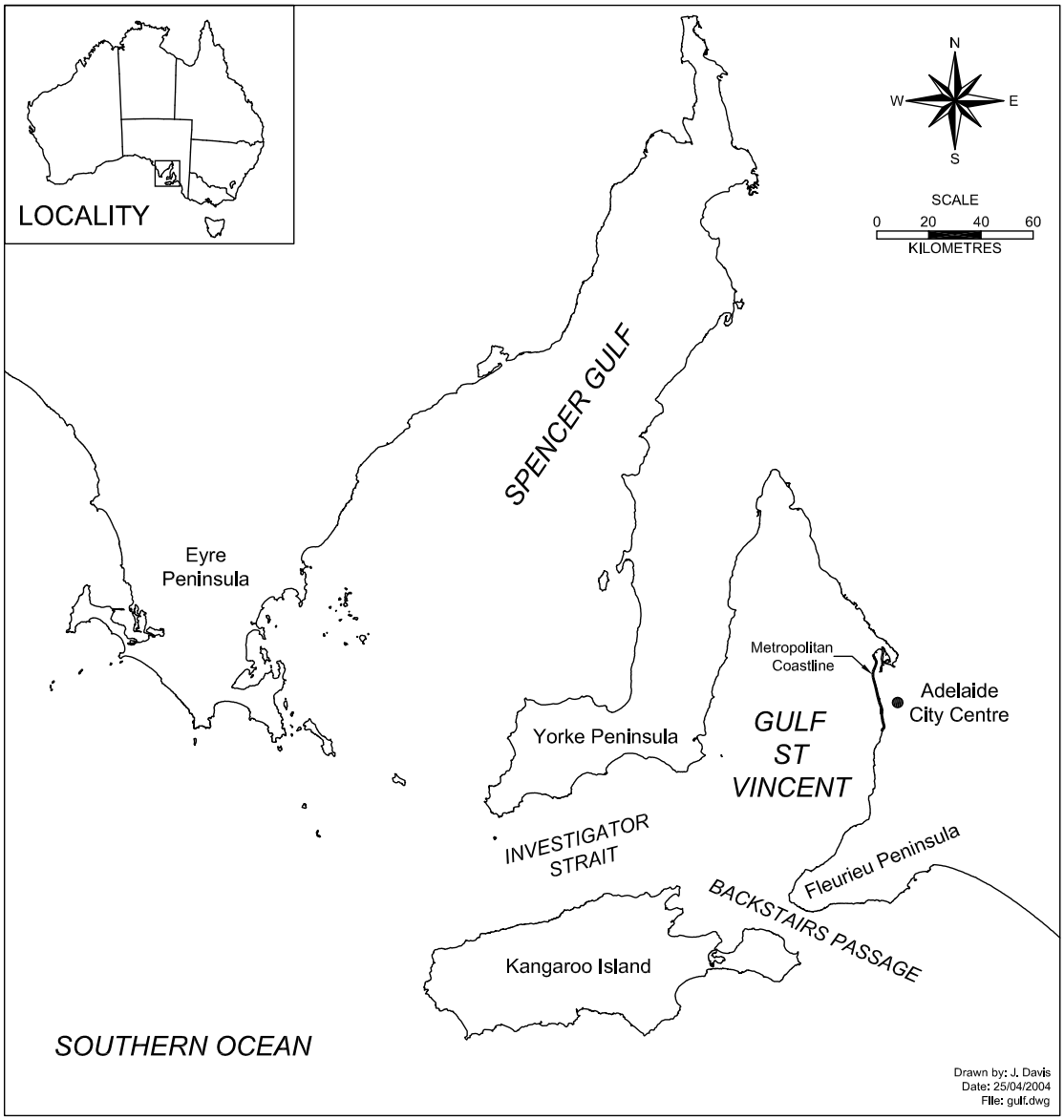

Figure 1.2 Location of Gulf St Vincent and the metropolitan coastline of Adelaide.

1.2 RESEARCH OBJECTIVES

The overall objective of the research was to attempt to build spatial and temporal variability into the way ripples are parameterised, predicted and modelled. This was to be achieved through the use of the spectral density function calculated from the rippled surface. Under this overall objective the study set a number of primary and secondary objectives. The primary objectives were to:

- Develop a new spectral-based method to parameterise wave-formed rippled beds which would allow the inherent variability of these types of bed forms to be taken into account with greater efficiency;
- Develop a method to predict the spectral parameterisation of the first objective for an equilibrium rippled bed given a set of flow parameters and sediment properties;
- Develop a new method to model the evolution of wave-formed rippled beds due to a change in surface wave conditions taking into account the time a rippled bed takes to transition from one equilibrium state to the another.

The secondary objectives were to:

- Undertake a series of experiments investigating the interaction between random surface waves and the sediment bed in a long wave flume;
- Develop apparatus to measure the rippled surface while waves were being run along the wave flume with a high degree of accuracy;
- Undertake a series of experiments that investigated the dynamic nature of rippled beds developing under a surface wave spectrum that was not in equilibrium with the ripple field.

1.3 LAYOUT AND CONTENTS OF THESIS

This thesis is structured to provide a logical progression through the work that has been completed regarding the variable nature of rippled beds. Each of the following paragraphs outline the specifics of each chapter.

Chapter 2 reviews the current literature in regard to wave-formed rippled beds. The chapter is broken up into three main sections each of which reviews the particular literature relevant for each area in this body of work. The first section starts with a presentation of some of the traditional ripple prediction methods that have been developed to predict ripples from flow conditions and sediment properties. This section then outlines major issues, that have been identified by field based observational studies, that make using the traditional methods under real sea states in coastal areas problematic. The second section critiques some of the approaches that have been undertaken to account for the temporal variation of rippled beds. These approaches are the so-called moveable bed models which have been used as part of large scale coastal models to determined a functional dependency of rippled parameters with time. The third section presents and discusses the current literature which outlines spectral approaches to describe the seafloor. Chapter 2 concludes with an overall discussion of the literature regarding wave-formed rippled beds and highlights the gap in the literature, that is to be addressed by this research.

Chapter 3 presents the overall experimental procedure in terms of the laboratory equipment used and the experimental method undertaken. The laboratory equipment section presents specific details of the three components of the equipment: the wave generation and dissipation systems; sand bed properties; and the ripple measurement system. Included in the equipment section are a description of some of the preliminary establishment tests for the flume and the design and development of the laser scanner used to measure the rippled beds. The experimental methods section outlines the method used for the three types of experimental tests undertaken being the growth, equilibrium and transition tests. The chapter concludes with a review of the overall experimental method.

Chapter 4 starts by highlighting the inherent variability of rippled beds formed under the action of irregular waves. This is done by examining the variability of the ripple

parameters measured by this study and those presented by *Williams et al.* [2004]. The chapter goes on to present a new spectral method to parameterise rippled beds which is able to take into account the spatial variability of ripple fields with greater ease. Issues such as the calculation and filtering of the bottom surface spectrum are also discussed in this chapter. The chapter concludes with a review of the effectiveness of the spectral parameterisation method.

Chapter 5 outlines a method that allows the ripple spectrum developed in Chapter 4 to be predicted from surface wave conditions and sediment properties. The ripple spectrum is predicted through the development of an empirically derived theoretical spectral form similar to the spectral forms that are widely used in surface wave applications. The chapter concludes with a discussion of the performance of the spectral method. This is done by comparing the ripple predictions gained from the spectral method with other more accepted ripple prediction methods.

Chapter 6 presents the development of a ripple evolution model that allows a wave-formed rippled bed to be modelled in time, based on the flow and sediment conditions. The ripple growth and transition tests presented in Chapter 3 are first discussed in terms of the overall trends observed in both the growth of rippled beds from a no-ripple condition and the transition of rippled beds between two equilibrium states. The chapter then moves on to derive the ripple evolution model. This model uses the well known Logistic non-linear differential equation which is fitted to the empirical data sets obtained from the ripple growth and transition experiments. The Logistic equation uses a constant known as the evolution rate and a functional dependence is derived to estimate this rate from flow conditions and sediment properties. The chapter concludes with a review of the evolution model.

Chapter 7 presents the major conclusions drawn from the three related areas of this research and highlights a number of recommendations for future work in the area of building spatial and temporal variability into the analysis of wave-formed rippled sediment beds.

A number of publications have resulted from the work presented in this thesis. Ap-

pendix A presents a list of conference papers written while undertaking this study. Appendix B contains a copy of a journal paper published in the Journal of Geophysical Research – Oceans in 2004.

Chapter 2

Literature Review: Wave-Formed Rippled Beds

The formation of rippled beds affects biological, chemical and physical processes acting on or across the sediment-water interface. Due to the importance of predicting ripple parameters and the effect ripples have on bottom boundary layer processes, there has been a large amount of literature published on rippled sediment beds formed under the action of either waves and/or currents. The current research focused on rippled beds formed under the action of irregular waves and therefore this review will concentrate on the literature pertaining to the study of rippled beds formed under the action of wave induced motion only.

Questions arising as to how sediment ripples form under the action of waves and how these ripples are related to the wave conditions that formed them have been posed for almost 100 years. The earliest paper to be found by the current study which discussed the formation of wave-formed rippled beds in terms of ripple marks and vortex shedding was published by *Ayrton* [1911]. However, it was not until the oscillating plate experiments of *Bagnold* [1946] that the field of study fully developed. Since then there have been a large number of publications dealing with the growth, observation and estimation of ripple parameters both in laboratory and field settings.

The first section of this chapter will highlight the need to build variability and time dependency into ripple parameterisations. Four of the more widely used mathematical re-

lationships to predict rippled bed morphology under constant oscillating flow regimes will be presented and compared. The problems of using these prediction methods will then be discussed in terms of the spatial variability and transient nature of rippled beds that have been observed under real sea conditions. The second section will review two methods, moveable bed roughness models and ripple development models, that are currently used to model rippled bed growth. This area, although very important in predicting wave-formed ripple parameters, has received limited attention in the literature. As outlined in Section 1.2 this thesis concerns itself with the development of a new method to model the variability and transient nature of rippled beds using the spectral density function of the sediment surface. Hence, the third section of this chapter will review the spectral analysis methods that are currently available to describe and parameterise rippled beds. The chapter will conclude with an overall discussion of the literature regarding wave-formed rippled beds and highlight the gap, that is to be filled by the current research.

2.1 TRADITIONAL RIPPLE PREDICTION METHODS

There have been a large number of studies that have developed ripple prediction methods for rippled beds formed under the action of waves. This work, although different, has essentially followed the same approach of determining simple ripple bed parameterisations, the characteristic ripple height and length, from sediment properties and steady flow conditions. This section will first present four of the more widely used and compared methods [*Nielsen*, 1981; *Grant and Madsen*, 1982; *Wiberg and Harris*, 1994; *Mogridge et al.*, 1994] to predict ripple parameters then outline some of the problems traditional methods, in general, have in predicting and modelling rippled beds under dynamic wave conditions.

2.1.1 Stable Ripple Prediction Methods

[*Nielsen*, 1981] was one of the earlier methods to predict a characteristic ripple height and length from surface wave conditions and sediment properties. His method has been

widely tested and verified within the literature. He was also one of the first to combine a number of data sets to develop relationships based on ripples formed under a number of different situations. He sought to derive ripple parameters based on a mobility number (ψ) given as:

$$\psi = \frac{(d_o\,\omega)^2}{4(s-1)gD} \tag{2.1}$$

where d_o is the orbital excursion diameter (m), ω is the radian frequency (rad/s), s is the relative sediment density (ρ_s/ρ_w), g is the gravity constant (m/s^2) and D is the sediment grain diameter (m). The mobility number can be viewed as the ratio of the disturbing forces acting to move sediment grains over the gravitational forces acting to hold them in place [*Nielsen*, 1992].

Nielsen [1981] suggested that two sets of equations were needed to predict ripple properties adequately, depending on whether the ripples were artificially generated in a laboratory or generated under irregular waves in a field situation. The size and shape of field ripples are linked to the irregularity of the surface wave field, hence ripples formed under irregular waves tend to be shorter and flatter than under regular waves [*Nielsen*, 1981]. Nielsen's equations for the length and height of laboratory formed ripples (under regular waves) were given as:

$$\frac{2\lambda}{d_o} = 2.2 - 0.345\psi^{0.34} \tag{2.2}$$

$$\frac{2\eta}{d_o} = 0.275 - 0.022\sqrt{\psi} \tag{2.3}$$

where λ is the ripple length (m) and η is the ripple height (m). His equations estimating ripple parameters formed under field waves (irregular waves) were given as:

$$\frac{2\lambda}{d_o} = \exp\left(\frac{693 - 0.37\ln^8\psi}{1000 + 0.75\ln^7\psi}\right) \tag{2.4}$$

$$\frac{2\eta}{d_o} = 21\psi^{-1.85} \tag{2.5}$$

Nielsen [1981] indicated that when field conditions were low ($\psi < 10$) equation 2.3 should be used to calculate the ripple height in preference to equation 2.5.

The mobility number used in equations 2.4 and 2.5 is based on the use of the significant wave height to characterise the surface wave spectrum. The orbital excursion diameter is calculated using linear wave theory from the water depth, significant wave height and peak frequency. The ripple length and height parameterisations of *Nielsen* [1981] have been widely compared to laboratory and field based studies in the recent literature [e.g., *Hay and Wilson*, 1994; *Marsh et al.*, 1999; *O'Donoghue and Clubb*, 2001; *Faraci and Foti*, 2002]. Separating laboratory and field based data sets has enabled two methods to be established that are specific to either case.

A different approach was taken by *Grant and Madsen* [1982] who, using the oscillating water tunnel data of *Carstens et al.* [1969], related ripple lengths to the ratio of Shields numbers calculated using the skin friction and the non-dimensional critical shear stress to initiate motion (ϑ/ϑ_c). The Shields number was calculated as:

$$\vartheta = \frac{0.5 f_w (d_o\,\omega)^2}{4(s-1)gD} \tag{2.6}$$

where f_w is the wave friction factor and is evaluated using the sand grain roughness. The Shields number is related to the mobility number as: $\vartheta = 0.5 f_w \psi$.

Grant and Madsen [1982] derived two sets of relationships for ripple height and steepness, one for an equilibrium range where ripple steepness is nearly independent of the stress ratio, and the other for a break off range, where ripple steepness becomes dependent on the stress ratio. *Li et al.* [1996] describe the equilibrium range as the stage in which the ripple length scales to the wave near bottom orbital excursion amplitude and the break off range as the stage where the ripple height will decrease due to higher flow conditions and the ripple length will stay relatively constant.

The relationships, derived by *Grant and Madsen* [1982], for the equilibrium range were given as:

$$\frac{\eta}{\lambda} = 0.16 \left(\frac{\vartheta}{\vartheta_c}\right)^{-0.04} \tag{2.7}$$

$$\frac{2\eta}{d_o} = 0.22 \left(\frac{\vartheta}{\vartheta_c}\right)^{-0.16} \tag{2.8}$$

while their relationship for the break off range was defined as:

$$\frac{\eta}{\lambda} = 0.28 S_*^{0.6} \left(\frac{\vartheta}{\vartheta_c} \right)^{-1.0} \tag{2.9}$$

$$\frac{2\eta}{d_o} = 0.48 S_*^{0.8} \left(\frac{\vartheta}{\vartheta_c} \right)^{-1.5} \tag{2.10}$$

in which

$$S_* = \frac{D\sqrt{(s-1)gD}}{4\nu} \tag{2.11}$$

is a non-dimensional sediment parameter, where ν is the kinematic viscosity (m^2/s). Wave orbital amplitude and skin friction are related via the wave friction factor. Their relationships are completely based on one set of laboratory data [*Carstens et al.*, 1969] and do not take into consideration the irregularity of the surface wave spectrum. However, the main aim of *Grant and Madsen* [1982] was to develop a movable bottom roughness model which will be presented in the next section.

Wiberg and Harris [1994] also developed expressions for ripples formed under laboratory and field waves from a number of combined data sets. However, they classify them as orbital, anorbital or an intermediate type suborbital ripples based on an earlier classification developed by *Clifton* [1976]. They noted that orbital ripples are generally formed in lower flow conditions and are the dominant ripple produced by shorter period regular laboratory generated waves. Conversely anorbital ripples are mainly formed by higher flow conditions that are typically found in field situations under irregular waves, but can be reproduced in the laboratory at longer periods. Interestingly they also commented that all three types of ripples can be found in close proximity given the right mix of sediment and flow conditions. *Wiberg and Harris* [1994] derived equations for the orbital ripple's height and length given as:

$$\lambda_{orb} = 0.62 d_o \tag{2.12}$$

$$\frac{\eta_{orb}}{\lambda_{orb}} = 0.17 \tag{2.13}$$

while their equations for the anorbital ripple height and length were given as:

$$\lambda_{ano} = 535D \tag{2.14}$$

$$\frac{\eta_{ano}}{\lambda_{ano}} = \exp\left[-0.095\left(\ln\frac{d_o}{\eta_{ano}}\right)^2 + 0.442\ln\frac{d_o}{\eta_{ano}} - 2.28\right] \tag{2.15}$$

Wiberg and Harris [1994] indicated that equation 2.13 should be used in preference to equation 2.15 when $d_o/\eta < 10$. Equation 2.15 needs to be solved iteratively for the ripple height. *Wiberg and Harris* [1994] established criteria, based on the ratio between the orbital excursion diameter over the ripple height, for deciding if ripples are orbital ($d_o/\eta_{ano} < 20$), anorbital ($d_o/\eta_{ano} > 100$) or suborbital ($20 < d_o/\eta_{ano} < 100$) which are all based on equation 2.15. Suborbital ripple parameters are calculated by taking a weighted geometric mean of the bounding values of the orbital and anorbital ripples, so that:

$$\lambda_{sub} = \exp\left[\left(\frac{\ln(d_o/\eta_{ano}) - \ln 100}{\ln 20 - \ln 100}\right)(\ln\lambda_{orb} - \ln\lambda_{ano}) + \ln\lambda_{ano}\right] \tag{2.16}$$

Wiberg and Harris [1994] did not include any variation of the surface wave spectrum into their parameterisations except through the use of the significant wave height and peak wave frequency, which are used to calculate the orbital excursion diameter from linear wave theory. Interestingly they did discuss the use of the *Miller and Komar* [1980] data set which contained measured ripple lengths generated under real sea conditions with a multiple-peaked surface wave spectra. *Wiberg and Harris* [1994] found that some of these data sets contain ripples classified as both orbital and anorbital ripples which would seem to indicate that a broad spectrum had caused the ripples to deviate from the predicted behaviour of ripples formed under monochromatic or narrow banded spectral waves. This suggests that the method does not work under these types of conditions. Calculating a single value of the ripple length and height will provide little information as to the overall variability that is evident on a rippled bed created under a spectrum of surface waves.

Mogridge et al. [1994] derived relationships for ripple parameters based on a period parameter (χ) defined as:

$$\chi = \frac{D}{(s-1)gT^2} \tag{2.17}$$

where T is the wave period (s). The period parameter was originally derived by ***Mogridge and Kamphuis*** [1972] and can be related to the mobility number (refer to equation 2.1) by:

$$\psi = \frac{(d_o\,\omega)^2}{4(s-1)gD} = \left[\frac{\pi d_o}{D}\right]^2 \left[\frac{D}{(s-1)gT^2}\right] = \left[\frac{\pi d_o}{D}\right]^2 \chi \tag{2.18}$$

Interestingly the period parameter has no dependence on the depth of water or the surface wave height. Their relationship for the ripple length formed under longer period waves ($\chi < 0.15 \times 10^{-6}$) was given as:

$$\frac{\lambda}{D} = 1394 \tag{2.19}$$

and for short period waves ($\chi > 0.15 \times 10^{-6}$) was given as:

$$\log_{10}\left(\frac{\lambda}{D}\right) = 13.373 - 13.772\chi^{0.02054} \tag{2.20}$$

Due to a lack of data at lower values of the period parameter (longer period waves), the ripple height was defined for all values of the period parameters as:

$$\log_{10}\left(\frac{\eta}{D}\right) = 8.542 - 10.822\chi^{0.03967} \tag{2.21}$$

Mogridge et al. [1994] based their equations on a wide variety of field and laboratory conditions, but did not make any distinction in their relationships between ripple forms generated by regular or irregular waves. However, the study did use the data of *Willis et al.* [1993] who investigated the effect that directional spreading of a wave field has on ripple development. *Willis et al.* [1993] ran a number of wave basin experiments in which the directional spread of the waves was altered. They concluded that ripples do not have a strong dependence on the directional spread of a wave field. However, their results were not conclusive, as they were based on a limited number of experiments which did not indicate a significant relationship. Based on field observations [*Traykovski et al.*, 1999; *Ardhuin et al.*, 2002] ripples will adjust their direction to align with the peak surface wave direction. It is currently not known how the rippled bed will react to a narrow or broad directional surface wave spectrum.

The four methods described [*Nielsen*, 1981; *Grant and Madsen*, 1982; *Wiberg and Harris*, 1994; *Mogridge et al.*, 1994] are only a few of the many ripple prediction methods that can be found in the currently literature. They have been chosen because these studies have been cited widely and give an appreciation for a number of different methods employed in the literature to predict ripple geometry.

2.1.2 Limitations of the Traditional Methods

The problem with traditional ripple prediction methods, in general, is that they do not take into account either the spatial or temporal variability of the ripple field. Factors such as irregularity in wave induced currents, sediment bed variability, benthic organism activity, storm and tidal induced currents all act to increase the variability of rippled beds over small spatial and temporal scales. Ripples formed under real sea states will contain a large number of ripple lengths, heights and ages which have been formed by the current and previous hydrodynamic conditions [*Amos et al.*, 1988; *Vincent and Osborne*, 1993; *Hay and Wilson*, 1994; *Traykovski et al.*, 1999; *Ardhuin et al.*, 2002]. Real sea waves are continually acting to change ripple dimensions and directions, which requires the movement of a large quantity of sediment, significant energy and time [*Marsh et al.*, 1999].

The four methods [*Nielsen*, 1981; *Grant and Madsen*, 1982; *Wiberg and Harris*, 1994; *Mogridge et al.*, 1994] presented in the previous section all use two values, the significant wave height and peak frequency, to parameterise an irregular wave field. In the ocean, irregular wave fields are composed of a large number of individual waves with a random distribution of periods, heights and directions. As random irregular waves move over a rippled bed the formation of eddies within the bottom boundary layer will also be random in nature, although more narrow banded than the surface wave field [*Mathisen and Madsen*, 1999]. *Madsen et al.* [1990] attribute the smaller heights, lower steepness and the more rounded shape of ripples formed under irregular waves compared with ripples formed under regular waves to the spectral components with less energy interacting with the ripple crests and flattening them. *Nielsen* [1981] also observed this effect in the ripples

formed under irregular wavefields.

Under an irregular wave field it is unclear to which flow length scale, if any, the ripple forms will scale. *Marsh et al.* [1999] compared the four methods, presented in the previous section, for predicting ripple properties generated in a laboratory setting under spectral, bichromatic and monochromatic wave simulations. They did this because rippled bed measurements, which were undertaken by *Vincent and Osborne* [1993] on a macro tidal beach where the water depth at high tide varied between 2 and 3 metres, compared poorly with previous published methods for ripple prediction. *Marsh et al.* [1999] found that all methods of ripple prediction generally over-estimated ripples formed under spectral wave conditions, except for the *Nielsen* [1981] field relationships (refer to equations 2.4 and 2.5), which generally under-estimated parameters. *Marsh et al.* [1999] indicated that under irregular waves, ripple forms were not found to show any significant scaling of ripple length with near bed orbital velocity. However, as the waves became more regular, ripple lengths became more dependent on orbital velocity. They suggested that current methods for predicting ripple geometry contain a bias toward laboratory based measurements and that the approach, as proposed by *Nielsen* [1981], of defining a separate set of equations for field (irregular) and laboratory (regular) formed ripples appeared to be the best option.

O'Donoghue and Clubb [2001] compared three [*Nielsen*, 1981; *Wiberg and Harris*, 1994; *Mogridge et al.*, 1994] of the above four ripple prediction methods (including a method by *Vongvisessomjai* [1984] which is not presented here) by plotting the non-dimensional ripple length and steepness determined from each method on two sets of axes (refer to Figure 2.1). Please note in Figure 2.1 d is the orbital excursion diameter (m), while d_m is the maximum orbital excursion diameter (m) for a given sand size and flow period (s). The maximum is defined as the value where the ripple length stops increasing and starts to decrease as the orbital diameter is increased. Hence, values of $d/d_m < 1$ indicate increasing ripple parameters while values of $d/d_m > 1$ indicate decreasing ripple parameters with a corresponding increase of orbital diameter. From Figure 2.1 comparisons between the methods can be observed.

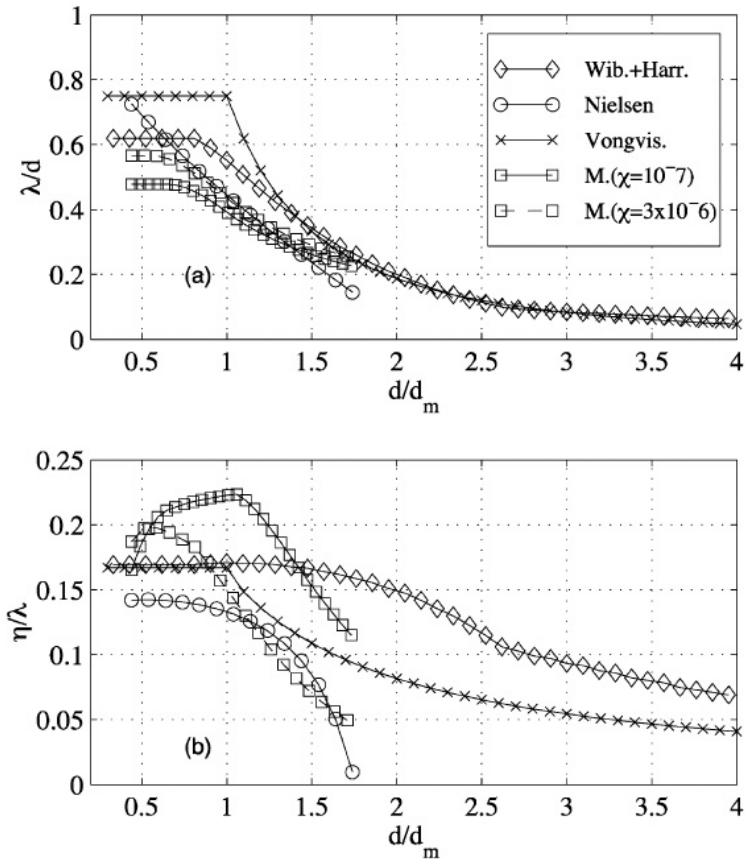

Figure 2.1 Comparison between ripple prediction methods: (a) presents the non-dimensional ripple length against the non-dimensional orbital diameter; (b) presents the ripple steepness against the non-dimensional orbital diameter. **Source:** *O'Donoghue and Clubb* [2001]

In Figure 2.1a the methods of *Mogridge et al.* [1994] and *Wiberg and Harris* [1994] predict the occurrence of orbital ripples (shown as a horizontal line at low values of d/d_m) while the method of *Nielsen* [1981] does not, however, the values predicted by *Nielsen* [1981] are comparable with the other methods. As the value of d passes into the decreasing ripple length regime the four methods show greater agreement in terms of the path taken as flow conditions are increased. In Figure 2.1b there is much less agreement between the four paths taken in either the increasing ($d/d_m < 1$) or decreasing ripple ($d/d_m > 1$) length regimes.

The main point of contention, for this study, in Figure 2.1 is the underling assumption

that rippled beds are in constant equilibrium with the flow conditions. *O'Donoghue and Clubb* [2001] produced the chart as a comparison between the methods, to allow other researches to estimate equilibrium ripple lengths and heights given certain flow conditions. A major issue is using these relationships to model ripples that are growing or decaying under changing surface wave conditions. There is no provision in the four relationships [*Nielsen*, 1981; *Vongvisessomjai*, 1984; *Mogridge et al.*, 1994; *Wiberg and Harris*, 1994] for a time lag between a change in flow conditions and a change in ripple parameters to be incorporated into the estimation. This assumption may be acceptable when flow conditions are changing very slowly, but would fail to estimate ripple properties adequately if there was a rapid change in flow conditions, such as during the onset of storm conditions after a calm period. *Hay and Wilson* [1994] indicated that the different rippled beds produced under storm conditions can be extremely complex, with multiple types of ripples existing on the bed all with a variety of ripple heights and lengths. Under such situations current methods of ripple prediction are unable to parameterise the resulting complex surface [*Hay and Wilson*, 1994]. Issues such as the time lag between a change in the hydrodynamic conditions and the development of a given bed will also be extremely important in such situations [*Hay and Wilson*, 1994].

The relationships shown in Figure 2.1 assume that ripples follow the same growth and erosion paths if the flow conditions are either increasing or decreasing. There has not been any substantial work undertaken determining if this will be the case and field studies observing ripple dynamics suggest that ripple growth/erosion paths will be different. *Traykovski et al.* [1999] observed ripples evolving under field conditions and suggested that ripples follow a hysteresis path based on flow and sediment conditions. Figure 2.2, which was presented by *Traykovski et al.* [1999], shows the temporal evolution, under real sea conditions, of a rippled bed over a 5 day period as a function of the surface wave conditions. From the field data shown in Figure 2.2 it is clear that evolving ripples under changing flow conditions will not follow the smooth transitional paths as suggested by traditional rippled bed prediction methods, but will step through a number of stages as they develop.

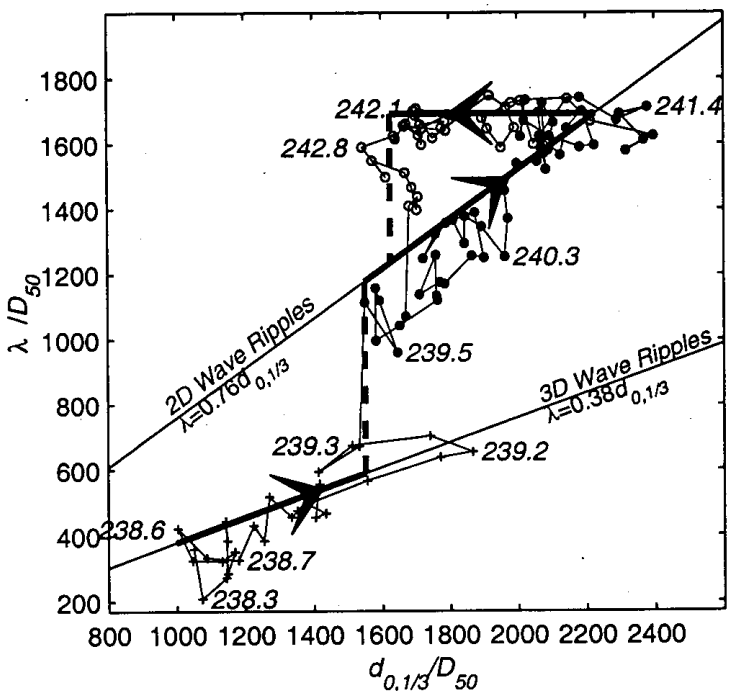

Figure 2.2 Rippled growth hysteresis showing the evolution of the ripple length as a function of the orbital excursion diameter with both quantities normalised by the 50 percentile grain size diameter. The crosses represent 3D ripples, the closed circles represent 2D ripples while the open circles represent relic ripples. The bold line with an arrow pointing to the left is the hysteresis path. The time of selected points is shown. **Source:** *Traykovski et al.* [1999]

.

The step like transitions shown in Figure 2.2 are very interesting. The abrupt transition suggests that the rippled bed is moving rapidly to a higher energy state. However, the large jump in the normalised ripple length may also be due to the method used to parameterise the three-dimensional rippled bed in terms of the characteristic ripple length. The ripple length is not a good parameter to use when discussing ripple energy levels.

In the recent ripple prediction literature, rippled sediment beds are generally thought of as long crested and uniform with a primary direction that aligns with the direction of wave travel. However, some rippled beds deviate from the typical idea of ripples with shorter crests, multiple directions and generally look disorganised and random. These types of beds are known as three-dimensional beds and have been observed by a large

number of previous field and laboratory studies [e.g., *Sleath*, 1984; *Vongvisessomjai*, 1984; *Amos et al.*, 1988; *Willis et al.*, 1993; *Hay and Wilson*, 1994; *Marsh et al.*, 1999; *Traykovski et al.*, 1999; *O'Donoghue and Clubb*, 2001]. To parameterise three-dimensional beds with current methods requires a characteristic ripple length and height to be determined from the beds. *Ardhuin et al.* [2002] discusses a spectral analysis technique for parameterising side scan sonar images of rippled beds in terms of their characteristic ripple length vector (both length and direction).

A number of authors have suggested formation mechanisms for three-dimensional beds, however, there has not been any conclusive agreement in the literature as to what these formation mechanisms are likely to depend upon. *O'Donoghue and Clubb* [2001] suggest that three-dimensional ripples form as an intermediate phase between smaller and larger two-dimensional vortex ripples, while *Sleath* [1984] suggests that three-dimensional forms only start to evolve after prolonged exposure of a sediment bed to oscillatory flows. *Vongvisessomjai* [1984] suggests that three-dimensional ripples are caused by flow regimes of higher energy that result in vortices being formed that have higher turbulence intensity which generates the lateral bed forms. The findings of *Marsh et al.* [1999] support this hypothesis by observing that ripples became progressively more three-dimensional in structure as the wave height, and hence the energy of the flow, increases. *Traykovski et al.* [1999] suggest that vortex ripples developing a sinuous three-dimensional form which allows the ripples to change direction without sections of the ripples migrating long distances. *Blondeaux* [2001] suggests two mechanisms for the formation of three-dimensional ripples. The first relates to centrifugal instabilities within the flow field which are associated with the finite curvature of the surface of a two-dimensional ripple, while the second is due to morphodynamic instabilities of the moveable sand bed [*Blondeaux*, 2001]. What is clear from the above studies is that a change in the bottom boundary flow field causes the ripples to break away from a standard two-dimensional form and develop a more three-dimensional pattern.

Another complicating factor in shallow seas is the effect benthic organisms have on the rippled field. Benthic organisms are continually acting to flatten ripple forms on the

bed. *Amos et al.* [1988] suggested that the rate of biodegedation on a sand bank at a depth of 22 m was between 1.1 and 1.7 $\times 10^{-4}\ kg\, m^{-1}\, s^{-1}$ (based on a ripple volume per unit width of 0.0015 m^3) and will degrade rippled beds to flat beds within 4 to 6 hours of flow conditions, too low to rework the bed, being established. However, the above rate would be very dependent on the local conditions such as the bio-activity and sediment size. *Wheatcroft* [1994] also observed the action of benthic organisms and suggested that they would cause rippled beds to flatten in less than 1 day. An interesting side effect of benthic animals was highlighted by *Briggs* [1989]. Benthic organisms will not only degrade the rippled bed, but cause the bed to lose its directional dependence. Wave-formed rippled beds are generally assumed to be anisotropic, while beds pitted by the action of organisms are isotropic.

The above discussion highlights the problems with the current methods to parameterise rippled beds under variable conditions. Factors such as: random fluctuations in the two-dimensional flow field; random spatial variation in sediment bed properties; benthic organism activity; historic ripples formed under previous wave conditions; and current formed ripples all add to the inherent variability that is to be expected on rippled beds formed in shallow seas. Wave-formed ripple parameterisations have largely ignored the spatial variability in rippled fields, however, there have been some attempts to account for the transient nature of rippled beds and these will be discussed in the next section.

2.2 RIPPLED BED GROWTH MODELS

There have been two main approaches employed to account for the transient nature of rippled beds. The first approach uses so-called moveable bed models in which the bottom roughness height (and hence ripple parameters) are re-calculated each time step as part of a hydrodynamic modelling simulation, based on the flow conditions. The second approach, which to the author's knowledge has not been undertaken before on wave-formed ripples, but has been undertaken on current formed ripples, attempts to develop a functional dependence on ripple parameters with time. These functions contain coefficients that are based on the flow and sediment properties and allow the time a rippled bed takes

to come to an equilibrium with the flow conditions to be estimated.

A limited set of previous laboratory studies have observed and recorded wave-formed ripples growing from flat bed conditions. *Lofquist* [1978] was the earliest study found. He used an oscillating water tunnel to generate large scale ripples in a number of different sands. His ripple observations were based on photos and notes taken over the experimental period. *Lofquist* [1978] presented the change of dimensionless ripple height ($2\eta/d_o$) and length ($2\lambda/d_o$) as a function of time. The time axis was scaled by the ratio of sediment diameter over orbital excursion amplitude (i.e. $2nD/d_o$) where n is the number of wave periods since ripples started to appear on the surface. *Lofquist* [1978] suggested that a rippled bed would obtain equilibrium with the flow conditions when the scaled time was greater than unity ($2nD/d_o > 1$), however, he did not attempt to develop a model of ripple growth from his data set. *Marsh et al.* [1999], based on a series of wave flume experiments, suggested that wave-formed ripples would attain equilibrium with the flow conditions after 30 to 40 minutes. This time was determined by visually observing the bed. The authors presented a number of ripple profiles with time, but this was done to confirm that the bed had reached equilibrium not to model ripple growth. *O'Donoghue and Clubb* [2001] undertook a series of experiments using a oscillating water tunnel that investigated ripple formation under both high and low mobility conditions. They found that under high mobility conditions, wave-formed ripples became stable after approximately 30 minutes while under low mobility conditions the ripples could take many hours to attain equilibrium with the flow conditions. As with *Marsh et al.* [1999] they based their estimate of the equilibrium time on visual observations of the developing ripple bed. *Faraci and Foti* [2002] undertook a series of flume based tests using irregular waves. From their tests they indicated that wave-formed ripples would take in the order of 15 minutes to reach equilibrium. However, their estimate may have been slightly low due the focuss being on individual ripples not the rippled bed as a whole. However, *Faraci and Foti* [2002] did measure and plot ripple parameters developing over time as the ripples grew from flat bed conditions, but did not attempt to develop a growth model from their data set.

The study of *Faraci and Foti* [2002] highlights the problem with using traditional methods to classify a changing rippled bed. Traditional methods parameterise rippled beds using a single value of the ripple height and length. Under the action of an irregular wave field rippled beds have been found to develop as patches across a surface [*Faraci and Foti*, 2002]. By concentrating on a single ripple the total energy of the bed is not taken into consideration as the bed develops, but the results are biased towards that one area of the bed that is growing at that particular time. This biasing tends to underestimate the time it takes rippled beds to come to equilibrium with the flow conditions.

This section will critique the two main methods, moveable bed roughness models and ripple development models, which are currently used to account for the transient nature of rippled beds.

2.2.1 Moveable Bed Roughness Models

The determination of bed roughness is an important factor in the calculation of wave attenuation rates in shelf seas [*Young and Gorman*, 1995; *Ardhuin et al.*, 2001]. The concept of bed roughness enables a relationship to be developed between the bottom shear stress and the physical boundary roughness conditions [*Grant and Madsen*, 1982] caused by the growth and decay of rippled beds.

The equivalent or effective sand grain roughness height K_N was introduced by Nikuradse in 1932, to take into account arbitrary bottom roughness elements in a given flow regime [*Van Rijn*, 1993]. In the case of moveable bed conditions such as when a rippled bed is evolving, a number of authors [*Grant and Madsen*, 1982; *Graber and Madsen*, 1988; *Tolman*, 1994, 1995; *Ardhuin et al.*, 2001] have used the effective sand grain roughness height to develop relationships for the different roughness factors based on the physical condition of the bed which are updated as flow conditions change. The effective roughness height can be separated into two main component roughness elements associated with the frictional resistance felt by a fluid as it passes over a movable sedimentary bed [*Van Rijn*, 1993]. These components take into account the friction forces due to the sediment grains k_g and the form drag pressure forces acting on the individual bed forms

Table 2.1 Form drag proportionality coefficients

Proportionality coefficients, α	Reference
25	*Swart* [1974]
28	*Grant and Madsen* [1982]
16	*Raudkivi* [1988]
20.3	*Bagnold* [1946], fitted by *Nielsen* [1992]
8	*Nielsen* [1992]

k_f. The total effective roughness can be estimated by the sum of these two components as:

$$K_N = k_g + k_f \tag{2.22}$$

There have been a large number of expressions developed for the grain roughness height, k_g. [e.g., *Raudkivi*, 1988; *Nielsen*, 1992; *Van Rijn*, 1993]. This study, however, will not present these relationships as it is concerned with the growth and evolution of rippled beds. The form drag roughness, due to ripple forms, has generally been assumed to be proportional to the ripple height and steepness [*Nielsen*, 1992]. This can be expressed mathematically as:

$$k_f \propto \eta\frac{\eta}{\lambda} \Longrightarrow k_f = \alpha\frac{\eta^2}{\lambda} \tag{2.23}$$

where α is a proportionality constant. A number of authors have used the above expression for bed form roughness with proportionality coefficients ranging from 8 to 28 (refer to Table 2.1).

There is a substantial difference in the values of the proportionality coefficient shown in Table 2.1. However, what is interesting about Table 2.1 is that all of the above authors agree on the very simple form of the ripple roughness expression (equation 2.23).

Madsen et al. [1990] suggested a different expression for the form roughness based on the ripple prediction method of *Grant and Madsen* [1982]. The expression they developed was:

$$\frac{2k_f}{d_o} = 1.5\left(\frac{\vartheta}{\vartheta_c}\right)^{-2.5} \qquad for \quad \frac{\vartheta}{\vartheta_c} \geqslant 1.2 \tag{2.24}$$

where the ϑ/ϑ_c is ratio of the Shields number ϑ over the critical value for initiation of motion ϑ_c (refer to equation 2.6). As shown in equation 2.6, ϑ is a function of the wave friction factor f_w which is in turn a function of the total effective roughness height. *Swart* [1974] provides an example of a functional dependence between the wave friction factor and the total effective roughness height. This relationship is given as:

$$f_w = \exp\left(5.213\left[\frac{K_N}{d_o/2}\right]^{0.194} - 5.977\right) \tag{2.25}$$

As outlined at the start of this section, by using the above expressions for the bottom roughness height, a number of authors [*Grant and Madsen*, 1982; *Graber and Madsen*, 1988; *Tolman*, 1994, 1995; *Ardhuin et al.*, 2001] have developed moveable bed roughness models to account for the highly dynamic nature of wave-formed rippled beds. This dynamic nature is then incorporated into flow and sediment transport models. The concept of moveable bed roughness models is very simple. The model first calculates the flow conditions at some time step, from this estimation ripple parameters are predicted which are then used to calculate a value of the bottom roughness height to use in the next time step. The ripple prediction step can be skipped, using the method developed by *Madsen et al.* [1990], but a similar process is followed. *Ardhuin et al.* [2001] indicated that the use of a moveable bed model routine enabled a greater degree of agreement between the measured observations and the modelling results to be achieved.

The main problem with the current application of moveable bed roughness models, however, is that they do not contain ripple evolution sub-models [*Tolman*, 1995]. The assumption is that ripple growth rates are much higher than the rate at which flow conditions change. This assumption implies that the rippled beds are in constant equilibrium with the flow conditions. Thus, current movable bed models suffer from the same limitations as wave-formed ripple prediction methods (refer to Section 2.1.2).

2.2.2 Ripple Development Models

As outlined above moveable bed roughness models do not have ripple evolution sub-models which allow ripple parameters to be estimated as a function of the flow conditions,

sediment properties and time. This subsection will outline some of the work undertaken in developing growth models for current-formed ripples growing from flat bed conditions. The main focus of these studies has been to determine the rate at which the ripples grow within fluvial environments given a set of flow and sediment parameters. A number of these relationships for unidirectional flows will be presented and compared as part of this section. To the author's knowledge there have been no such expressions developed for wave-formed ripples.

Nikora and Hicks [1997] reviewed the methods that were currently available to model the growth of ripple parameters with time. Some of the original references of these relationships were unavailable to the author because of language and availability issues. The review of the earlier methods presented here is largely based on a review undertaken by *Nikora and Hicks* [1997].

Nikora and Hicks [1997] indicated that one of the first methods to model the growth of sand waves from a flat bottom was developed by *Shuliak* [1971] and was given as:

$$\frac{p_o(t)}{p_e} = 1 - e^{-\gamma(t/T_e)} \tag{2.26}$$

where p_e is the equilibrium value of parameter p_o (either the ripple height or length), γ is a coefficient which is dependent on the flow conditions and sediment properties, t is the time and T_e is the time it takes the bed to reach equilibrium.

Nikora and Hicks [1997] reported that from theoretical considerations *Tsujimoto and Nakagawa* [1983] obtained the following relationship:

$$p_o(t) = K\sqrt{t} \tag{2.27}$$

where K is a function of the flow and sediment properties.

Based on dimensional considerations a power function was proposed by *Grinvald and Nikora* [1988] which was given as [*Nikora and Hicks*, 1997]:

$$\frac{p_o(t)}{p_e} = \left(\frac{t}{T_e}\right)^{\alpha} \tag{2.28}$$

where α is a scaling exponent equal to 0.28 for both the height and length parameters [*Nikora and Hicks*, 1997] which indicates a constant steepness for current formed ripples.

After reviewing the currently available methods to model ripple growth with time *Nikora and Hicks* [1997] developed a spectral method which was very similar to the power function relationship given by *Grinvald and Nikora* [1988] (refer to equation 2.28).

More recently *Baas* [1999] developed two empirical expression for the development of current-formed ripple parameters based on a number of experimental tests undertaken in a flume setting. These equations were given as:

$$\frac{\eta_t}{\eta_e} = 1 - (0.01)^{t/T_e(\eta)} \tag{2.29}$$

$$\frac{\lambda_t - \lambda_o}{\lambda_e - \lambda_o} = 1 - (0.01)^{t/T_e(\lambda)} \tag{2.30}$$

where η_t and λ_t are the bed form height and length at time t, η_e and λ_e are the equilibrium height and length, λ_o is the length of the first bed forms appearing on the flat bed, and $T_e(\eta)$ and $T_e(\lambda)$ are the equilibrium time for the height and length respectively. *Baas* [1994] suggests that T_e can be considered the time it takes a parameter to reach 99% of its final equilibrium value.

Figure 2.3 provides a comparison between the above four methods used to model the growth of ripple parameters with time. The plot shows a fictitious simulation where the ripples are developing from a flat bed state to a fully developed bed over a period of 100 minutes. The final equilibrium height and length of the rippled bed is 10 and 40 mm respectively. The coefficients used for each equation were as follows: equation 2.26 $\gamma = 0.6$ based on *Nikora and Hicks* [1997]; equation 2.27 $K = P_e/T$; equation 2.28 $\alpha = 0.28$ based on *Nikora and Hicks* [1997], and equation 2.30 $\lambda_o = 5\ mm$.

In Figure 2.3, all methods show a rapid growth of ripple parameters at the start of the simulation with a flattening off of ripple parameters with time. All methods shown pass through the equilibrium point at a time of 100 minutes, however, only two of the relationships, those of *Shuliak* [1971] and *Baas* [1999], predict the equilibrium values at times greater than the equilibrium time. The relationships of *Tsujimoto and Nakagawa* [1983] and *Grinvald and Nikora* [1988] show ripple parameters continually increasing as the time tends to infinity. Only the relationship of *Baas* [1999] allows the specification of initial ripple parameters.

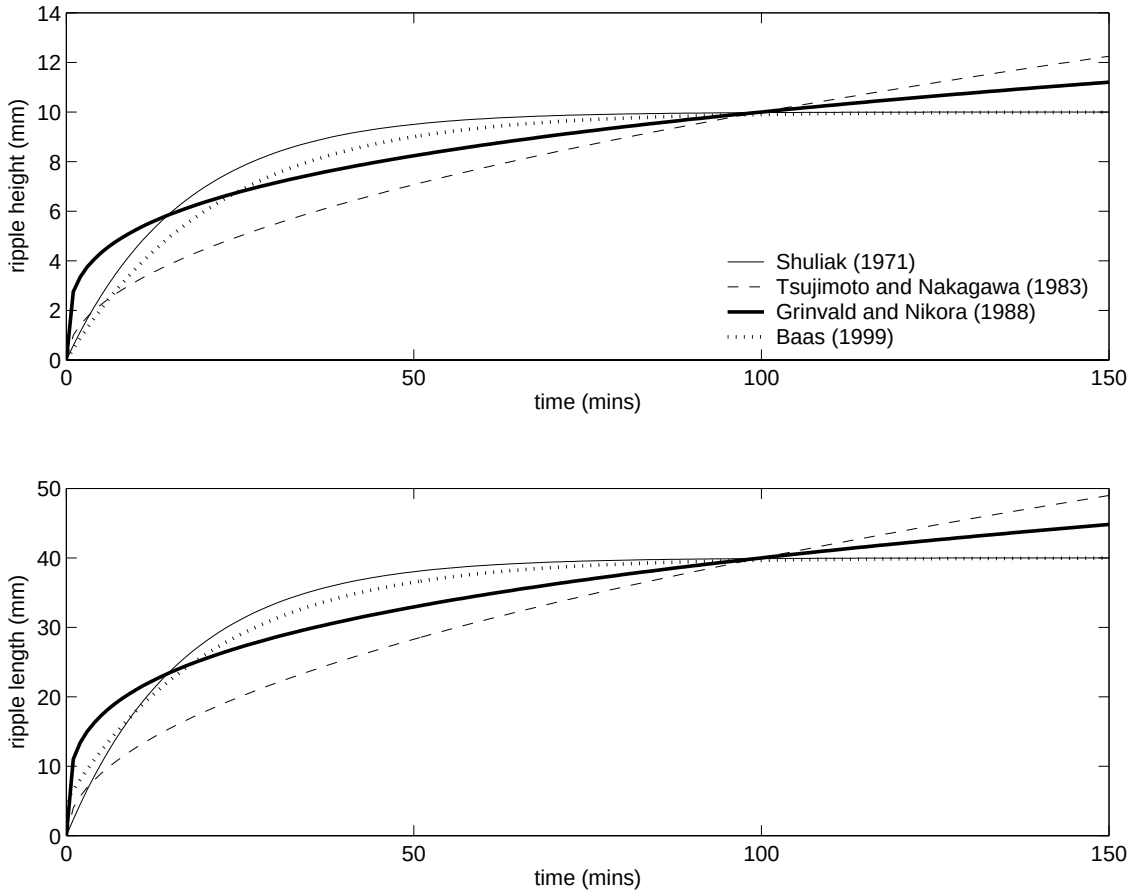

Figure 2.3 A comparison between various ripple development methods.

A major issue is that the expressions presented above suggest the same growth relationship for the ripple height and length which comes from the constant steepness assumption of current-formed ripples. This assumes that different scales of ripples are self-similar with small ripples the same shape and dimension as larger ripples. However, as shown in Figure 2.1, based on present ripple prediction methods, wave-formed ripples will show substantial variation as they increase with increasing flow conditions. *Bagnold* [1946] suggested that wave-formed ripples go through two stages as they develop: a rolling grain and a vortex stage with different forms apparent in each stage. The experiments undertaken by *Faraci and Foti* [2002] indicate that wave-formed ripple steepness is not constant as ripples grow from a flat bed condition, but will increase with time up to some equilibrium value.

Another problem with using the above relationships to model wave-formed ripple development and evolution under changing hydraulic conditions is that they do not easily allow the specification of a decreasing rippled bed (either height and length). When flow conditions are lower than the flow conditions that formed the bed, but still high enough to initiate sediment motion, ripple parameters will decrease in size [*Ardhuin et al.*, 2002].

2.3 SPECTRAL ANALYSIS TECHNIQUES

Thus far, rippled beds have been parameterised in terms of their characteristic length and height. Issues such as the spatial and temporal variability of ripple beds have been largely ignored. As highlighted by the study of *Faraci and Foti* [2002] ripple beds develop by the merging of discrete patches of ripples. Hence, the modelling of rippled beds requires that the bed be thought of as developing as a whole and ideally should be parameterised as a whole. A more efficient method to describe an approximately stationary series, such as a ripple field, is to decompose the rippled bed into its major spatial frequency components via the use of a Fourier transform algorithm.

Spectral analysis techniques have been applied to the problem of describing the sediment-water interface for approximately 40 years. However, there has been little interest in the method by researchers developing prediction methods for wave-formed rippled beds. Conversely researchers undertaking spectral analysis based studies of the seafloor have not tried to place their work in context with the more traditional analysis methods of wave-formed rippled beds (refer to Section 2.1.1).

This lack of interest is largely due to the type of research which has been undertaken using spectral methods. Previous spectral research has generally concentrated on: the spectral analysis of the bathymetery of the seafloor as part of acoustic studies [e.g., *Fox and Hayes*, 1985; *Briggs*, 1989; *Pouliquen et al.*, 2000; *Briggs et al.*, 2002; *Lyons et al.*, 2002; *Moore and Jaffe*, 2002]; developing descriptions of rippled beds formed under uni-directional flow regimes [e.g., *Nordin and Algert*, 1966; *Hino*, 1968; *Jain and Kennedy*, 1974; *Engelund and Fredsoe*, 1982]; or developing growth models for current-formed ripples [e.g., *Coleman and Melville*, 1996; *Nikora and Hicks*, 1997]. As will be shown in

this section there has been limited attention given to the isolation and description of wave-formed rippled beds in terms of their spectral density function and relating this function to oscillatory flow and sediment properties.

2.3.1 Historical Development

The idea of calculating the spectral density function of sediment rippled beds was first reported by *Nordin and Algert* [1966] who indicated that the variability of current-formed ripples could be described more concisely by decomposing the ripple surface into its major frequency components. They suggested that the ripple surface could be described using a Markov second-order linear model, and from this assumption they derived a theoretical spectral density function in terms of the statistical properties of the rippled surface. *Nordin and Algert* [1966] also related the overall bed roughness to values in the covariance function. *Hino* [1968] extended the work and proposed a *"-3"* power law to describe an equilibrium spectral density function for current-formed ripples based on other spectral applications such as the Phillips *"-5"* [*Phillips*, 1958] power law for the decay of high frequency components in the water wave spectrum. The current-formed ripple power law model was derived on dimensional grounds with *Hino* [1968] indicating that the model was better suited to higher spatial frequencies. The *"-3"* power law relationship for the equilibrium spectra compared favourably with the experimental results of *Nordin and Algert* [1966], *Ashida and Tanaka* [1967], and *Fukuoka* [1968] over a wide range of conditions. *Jain and Kennedy* [1974] also derived a *"-3"* power law relationship for equilibrium current-formed ripple spectra using a continuity relationship.

Akal and Hovem [1978] published the earliest study found to use a two-dimensional power spectrum and related autocorrelation function to describe the seafloor. Their objective was to develop a method to analyse acoustic bottom roughness and involved the analysis of small scale stereo photographs (1.64 m^2) and larger scale contour maps (40 km^2). While they discussed their two-dimensional method in detail they did not to develop a useful model to analyse acoustic bottom roughness. It was difficult to place this study in context, as *Akal and Hovem* [1978] did not relate their method to previous studies

undertaken in this area.

Fox and Hayes [1985], in a comprehensive study, developed a statistical measure of the bottom acoustic roughness from the slope of the bottom amplitude spectrum. The paper provides a good review of the autocorrelation, autocovariance and power spectrum functions. Issues such as how stable data sets were over different scales of dependence were discussed in detail and used to delineate the measured data into different geological provinces. *Fox and Hayes* [1985] calculated the phase spectrum of the seafloor and concluded that it was randomly distributed. To remove the high level of noise in the spectral estimates *Fox and Hayes* [1985] used a power law model of the spectrum as originally derived by *Hino* [1968]. Issues with the anisotropic nature of the seafloor were discussed and a method was derived to overcome these issues by studying the variation of the power law coefficients as a function of direction.

Briggs [1989] examined the seafloor roughness of scales smaller than 1 metre using high resolution ($> 5\ mm$) data obtained from stereo photographs and mylar traces of the seafloor to develop a series of power spectral estimates. The study used a power law to derive a measure of the bottom acoustic roughness similar to the method employed by *Fox and Hayes* [1985]. At each of their study sites a number of power spectral estimates with different orientations were taken to which a power law was fitted. The power law exponents and offsets were then averaged to given an average description of each site. No definitive trend between the orientation and the exponent of the power law was found which is surprising on an anisotropic surface. Interestingly *Briggs* [1989] discusses a flattening off of spectral energy at low frequencies. *Bell* [1975] also discusses this flattening off for spectral estimates lower than some critical frequency. *Briggs et al.* [2002], following on from *Briggs* [1989], undertook further field measurements. *Briggs et al.* [2002] split the bottom spectrum into multiple frequency bands to which they fitted a separate power law relationship. This was undertaken so that the effect of different roughness frequencies on acoustic scattering could be determined (i.e. a high frequency scattering compared to a low frequency scattering).

Lyons et al. [2002] used a Gaussian based two-dimensional method, originally derived by *Pouliquen et al.* [2000], to describe an anisotropic seafloor in terms of its spectral function. The spectrum of the seafloor should have a strong time and directional dependence, especially in areas where there is a high level of biological activity [*Lyons et al.*, 2002]. *Lyons et al.* [2002] used stereo photographs to develop digital elevation models of the seafloor. To estimate the two-dimensional spectrum they used a method similar to *Akal and Hovem* [1978], but indicated that spectral leakage (aliasing) could be a problem in some situations. *Lyons et al.* [2002] compared a number of data tapering windows to overcome the problem of spectral leakage. A modified Gaussian model was developed by combining the model proposed by *Pouliquen et al.* [2000] and the power law model originally derived by *Hino* [1968].

A major criticism of previous work in this field is that the studies have either focused on current-formed ripples, thus ignoring wave-formed ripples, or have concentrated on the seafloor as a whole. Current-formed ripples will generally be asymmetric in their cross section without a well defined flow length scale in the near bed boundary layer which tends to make relating the spectrum to flow parameters problematic. Acoustic backscattering studies are interested in the overall acoustic roughness of the seafloor [*Pouliquen et al.*, 2000; *Lyons et al.*, 2002; *Briggs et al.*, 2002] and hence have limited interest in the isolation and description of wave-formed sediment ripples.

To the author's knowledge there have been no studies that have used the bottom surface spectrum to analyse wave-formed ripples and relate this spectrum back to flow and sediment conditions. This is somewhat surprising since wave-formed ripples generally have symmetrical shapes and a well defined flow length scale, the orbital excursion diameter, within the near bottom flow regime. This suggests that developing a spectral analysis method to classify and predict wave-formed ripples would be easier and more intuitive than undertaking the same analysis on current-formed ripples.

2.3.2 Theoretical Spectral Forms of Rippled Beds

There has been a large amount of work undertaken on water surface wave spectra to derive theoretical spectral forms and relate these forms back to the growth parameters of waves being the wind velocity, duration and fetch [*Young*, 1999]. Examples of common forms of the water wave spectra are the JONSWAP form [*Hasselmann et al.*, 1973], the Pierson-Moskowitz form [*Pierson and Moskowitz*, 1964] and the Toba form [*Toba*, 1973].

Conversely, there has been limited work undertaken on deriving the same types of theoretical spectral forms for rippled beds and relating the ripple spectra back to flow conditions and sediment properties. As outlined in Section 2.3.1, most of the theoretical forms for the bottom sediment spectrum are largely based on a power law model, as derived by *Hino* [1968]. However, a number of authors have suggested different mathematical models to represent the spectra of the sediment-water interface [e.g., *Bell*, 1975; *Briggs et al.*, 2002; *Pouliquen et al.*, 2000]. This section will briefly discuss each of these methods.

Most of the work undertaken in this area has concentrated on fitting the high spatial frequency decay of the spectrum to determine some value of acoustic bottom roughness. The fitting process is undertaken in log-log space using a power-law model which takes the general form of:

$$S(f_s) = \frac{\alpha}{f_s^{\gamma}} \tag{2.31}$$

where α is a constant depending on the angle of repose of the sediment [*Hino*, 1968]; γ is the power-law exponent; S is the spectral function and f_s is the spatial frequency or wavenumber (k). Equation 2.31 plots as a straight line in log-log space. *Hino* [1968] was the first to suggest such a functional form of the sediment-water interface spectrum. *Lyons et al.* [2002] suggested that the value of the exponent in equation 2.31 would have a value ranging between 3 and 4. Importantly *Fox and Hayes* [1985] highlighted that the value of the exponent in equation 2.31 will depend largely on the type of spectrum generated (i.e. power, amplitude or variance spectra). *Fox and Hayes* [1985] determined the value of the amplitude spectrum exponent to be *"-1"*, while for a power spectrum the exponent was *"-2"*. There has been little deviation from the above expression in the literature.

Briggs et al. [2002] fitted multiple power laws to their measured spectra. They did this by splitting each individual spectrum into multiple bands and fitting equation 2.31 to each band. This gave multiple values of α and γ for each component spectrum. Splitting the spectrum up in this way was useful in determining parameters for acoustic reflection models that require an accurate estimation of the spectrum across bands that correspond to the particular acoustic frequency [*Briggs et al.*, 2002].

Bell [1975] undertook spatial modelling of large scale ocean topography using a spectral method. He suggested that at high wavenumbers ($cycles/km$) the bottom spectrum displays an approximate *"-2"* falloff while at low wavenumbers there was a flattening of the spectrum. *Briggs* [1989] also noted this trend in his measurements. *Bell* [1975] derived the following equation to model the seafloor.

$$F(k) = \frac{F_o}{k^2 + k_c^2} \frac{k_c^2}{k^2 + k_c^2} \tag{2.32}$$

Bell [1975] suggested values of $F_o = 250\ m^2\ cycles\ km^{-1}$ and $k_c = 2.5\ cycles\ km^{-1}$ to fit equation 2.32 to measured data. Due to the very large scale of the measurements equation 2.32 was of little use to the current study.

As outlined above, a two-dimensional filtered Gaussian approach was undertaken by *Pouliquen et al.* [2000] to determine the penetration of acoustic waves into the seafloor at specific grazing angles. Their model did not take into account the higher frequency end of the spectrum, but was able to account for both isotropic and anisotropic surfaces. The model has the form of:

$$W(\mathbf{k}) = Q(\mathbf{k}, \mathbf{k_c}) + Q(\mathbf{k}, -\mathbf{k_c}) \tag{2.33}$$

where $\mathbf{k} = (k_x, k_y)$ is the wavenumber vector; $\mathbf{k_c} = (k_{xc}, k_{yc})$ defines the average wavenumber and Q has the form of a joint probability distribution function, and is given as:

$$Q(\mathbf{k}, \mathbf{k_c}) = \frac{l_x l_y \delta^2}{4\pi} \exp\left[-\frac{l_x^2 (k_x - k_{xc})^2 + l_y^2 (k_y - k_{yc})^2}{2} \right] \tag{2.34}$$

where k_x, k_y are the components of the wavenumber; l_x, l_y are the components of the correlation length; δ is a factor that allows the root mean squared roughness variance to

be specified independent of $\mathbf{k}_c$. *Lyons et al.* [2002] modified equation 2.33 to include a high frequency tail to the spectral form, which was given as:

$$W_g(\mathbf{k}) = \frac{\alpha}{k^\gamma} + W(\mathbf{k}) \tag{2.35}$$

where α and γ are the power law offset and exponent similar to equation 2.31.

The methods found to parameterise the sediment surface in terms of its spectral function are all based on developing a spectral form for the whole of the sediment (seafloor) surface with little attention given to wave-formed rippled beds. As such the spectral methods presented are of little use to the current study which sets out to isolate the ripple frequencies from the adjacent noise. By isolating the wave-formed ripple frequencies the aim is to approximate part of a non-stationary spatial series (the seafloor) by an approximately stationary spatial series (the ripple forms).

2.4 Summary and Discussion

The main aim of this research was to develop a spectral method to account for the substantial spatial and temporal variation observed on rippled beds. It is expected that this will allow rippled beds to be predicted and modelled under transient surface wave conditions more efficiently than currently is the case. This chapter reviewed the literature pertaining to the parameterisation and prediction of wave-formed rippled beds using traditional methods and critiqued the spectral methods that have been employed to describe the seafloor.

The chapter started with a review of the current methods to predict rippled beds from sediment properties and flow conditions. The major problems with the current methods is that they do not take into account the substantial variation that is apparent on rippled beds formed under real sea states. Using the characteristic ripple length and height to parameterise a rippled bed is akin to using the significant wave height and peak wavelength to describe a irregular surface wave field. These values do provide a measure of the sea state, but a lot of important information is lost, such as the distribution of wave heights and lengths as well as the directional spread of the wave field. Sediment beds have the

added problem in that the medium that the ripples grow on, the sediment, is also highly variable both in grain size distribution and slope. This is not generally an issue with water waves.

Section 2.2 reviewed the methods that have previously been developed to model the transient nature of rippled beds as part of hydrodynamic or sediment transport modelling studies via the bottom roughness height. The main limitation of these methods is the assumption that rippled beds are in constant equilibrium with the flow conditions. There is a general lack of information regarding the time it takes wave-formed rippled beds to attain equilibrium with the flow conditions. From a number of laboratory studies this time, under low flow conditions, can be substantial. Under field conditions there is the added problem of benthic organisms which are constantly acting to flatten or disrupt rippled beds. The suggestion is that, in shallow shelf seas, rippled beds might never attain equilibrium with the surface wave conditions [*Vincent and Osborne*, 1993; *Traykovski et al.*, 1999; *Ardhuin et al.*, 2002]. A number of ripple development models were presented which have developed a functional dependency between growing current-formed rippled parameters and time. Of these models only two seem to provide a reasonable functional dependence, in that they predicted equilibrium values at times greater than the equilibrium time. However, once again these models focused on crude measures to parameterise a rippled bed: the ripple length and height.

The final section in this chapter (section 2.3), reviewed the current literature on spectral methods to parameterise the seafloor. This author considers that this is the way forward in both parameterising and modelling the spatial and temporal variability of rippled beds formed under real sea states. However, there have not been any examples found in the literature that have used spectral techniques to specifically parameterise wave-formed rippled beds. Most of the recent work undertaken in this area has been in determining the acoustic roughness of the seafloor from the seafloor spectrum. To the author's knowledge there has been no research on whether or how the hydraulic roughness can be calculated from the rippled bed spectrum.

2.5 THE RESEARCH GAP

To the author's knowledge there has been no studies that have:

- Attempted to build variability into a rippled bed parameterisation;
- Developed a spectral analysis technique that allows wave-formed rippled beds to be described in terms of its spectral density function;
- Developed a method to predict the spectral density function of rippled beds given a set of flow conditions and sediment properties;
- Modelled the evolution of wave-formed rippled beds due to a change in surface wave conditions taking into account the time a rippled bed takes to develop;
- Modelled rippled beds evolving between any two given equilibrium states.

This study attempts to develop a spectral analysis technique to parameterise and predict wave-formed rippled beds that allows the spatial variability of a rippled bed to be incorporated into the analysis. The new spectral parameterisation is then used to model how a rippled bed develops with time in terms of a change in the total spectral energy of the bed.

Chapter 3

Experimental Procedure

A series of experiments observing the interaction between surface waves and rippled bed morphology was undertaken in the wave flume located in the Robin Hydraulic Laboratory at The University of Adelaide, Australia. Experiments were designed to investigate both equilibrium and transient rippled beds under a variety of surface wave conditions and sediment properties. Plate 3.1 shows the X-Y positional table of the ripple scanner used to measure the sediment-water interface.

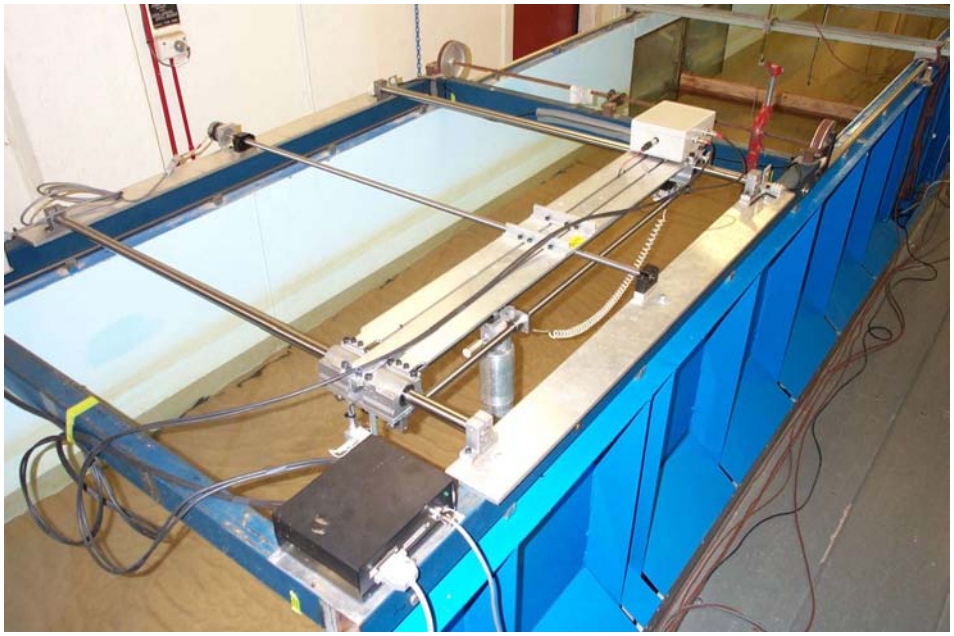

Plate 3.1 The X-Y positional table of the ripple measurement system designed and developed by this study.

This chapter will discuss the two main aspects of the overall experimental procedure, being the laboratory equipment and the experimental methods employed. The laboratory equipment section provides specific details of: the wave generation, dissipation and measurement systems; the physical properties of sediment beds; and the ripple measurement system designed by this study to scan the ripple surface. The methods section details the experimental procedure for the growth, equilibrium and transition ripple tests. The procedure is discussed in terms of the rippled bed measurements and the calculation of the surface wave spectrum from the measured time series of the water surface. The details of the growth, equilibrium and transition ripple tests undertaken will also be presented within the methods section, with examples of the types of data that were measured for each particular test illustrated. The third section in this chapter contains a discussion of two important aspects of this study: the spectral definitions that were adopted; and the stability of the surface wave spectra. The spectral definitions presented in this section will be used throughout the thesis. The stability of the water surface spectrum over an extended period is important because any change in the water surface spectrum will directly impact the formation of the rippled bed. The chapter concludes with a discussion of the laboratory equipment and experimental methods, with conclusions drawn about the effectiveness of the overall experimental procedure.

3.1 LABORATORY EQUIPMENT

This section outlines the details of the laboratory equipment required to conduct the wave flume experiments investigating wave-formed rippled sediment beds. The wave flume had not been used for a number of years prior to the laboratory experiments being undertaken. This study re-established the flume including: designing the wave dissipation beach; installing the sand beds; testing the wave probes and designing and writing the data acquisition software. A specialised piece of equipment using a laser displacement sensor was designed and developed by the author to scan the sediment surface to provide high resolution ripple measurements (refer to Plate 3.1). This section will look at the three main components of the equipment used: the wave generation and measurement systems;

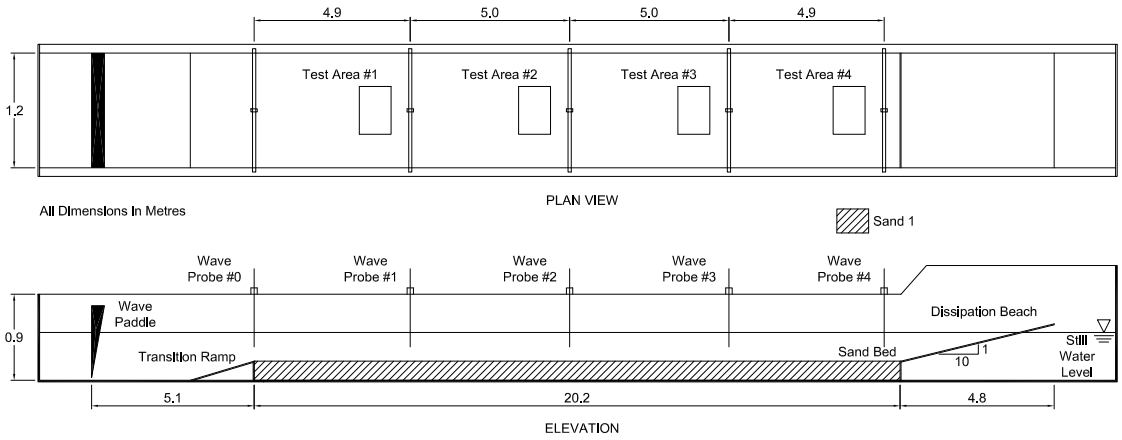

Figure 3.1 Plan and elevation views of the original wave flume setup.

the sand bed parameters and the ripple measurement system.

3.1.1 Wave Generation and Measurement Systems

The wave flume has a total length of 30 m and a width of 1.2 m with an overall depth of 900 mm (refer to Figure 3.1). Waves are generated via an hydraulic piston-type wave paddle with a triangular cross section. The depth of the flume and the shape of the wave paddle limited the height and frequency of the waves that could be generated. The range of irregular waves that could comfortably be generated by the system in its current configuration was frequencies between 1.2 and 0.8 Hz with significant wave heights up to 95 mm.

Irregular waves were generated using a specialised wave synthesiser program known as the *HR WaveMaker Wave generation control program* which was developed by HR Wallingford Ltd, UK. The wave generation software controls the movement of the wave paddle. The HR WaveMaker program can be used to generate regular waves or irregular waves conforming to a user defined spectral shape [*Beresford*, 1998]. The software generates irregular waves using a continuous random signal conforming to a predefined distribution, which is repeated over a time period depending on the frequency of waves

generated. Three surface wave frequency conditions were used in this study having peak frequencies of: 0.8; 1.0 and 1.2 Hz. The repeating period for each of these frequencies were: 10.67 minutes for the 0.8 Hz waves; 8.53 minutes for the 1.0 Hz waves; and, 7.12 minutes for the 1.2 Hz waves. This meant that the surface wave spectrum was repeated at least 14 times during the shortest test undertaken for this study. The repetition of the random wave signal was one of the benefits of using this software as it allowed the assumption that the surface wave spectrum was stable for the total test period (a point to be expanded upon further in Section 3.3.2).

A wave dissipation beach was installed across the end of the flume to reduce wave reflections. The dissipation beach was constructed using a smooth 5 m wooden ramp at a slope of 1-in-10 to which a series of vertical mesh sections and a coarse rock bed were added to aid in wave dissipation through turbulent loss. An analysis of wave reflection, using the Maximum Likelihood Method [*Young*, 1994], showed that the reflection coefficient of the dissipation beach was kept below 10% for the frequency range used in the experiments. Appendix C provides details of the wave reflection tests undertaken.

To measure the time series of the surface waves a set of five surface penetrating resistance wave probes were used (refer to Plate C.4, page 192). The probes had a measurement range of 300 mm and output voltages in the range of ± 5 V. The probes were linked to a data logging computer through an analog to digital board. Data acquisition software was written using the *Visual Designer*^{TM} suite (copyright 1993-1997 Intelligent Instrumentation) which allowed the time series to be written to the computer screen and to file. Prior to each test the probes were calibrated using 5 data points over a range of 250 mm, checked for stability and zeroed. Appendix D provides extra details of the wave probe calibration. Due to some high frequency electrical noise being evident within the output signal of the wave probes, a high frequency single pole resistance-capacitance filter was applied to the output of each probe. This filter removed signal noise above a frequency of 60 Hz. The wave probes were sampled at a frequency of 8 Hz to minimise aliasing effects.

3.1.2 Sand Bed Parameters

A 20 m long sand bed was installed in the flume, starting at a distance of 5.1 m from the wave paddle (refer to Figure 3.1). The thickness of the sand bed was chosen so that a higher degree of interaction between the water surfaces and sand bed could be achieved while still generating the largest waves possible. To aid in the smooth transition of waves as they moved from the deeper generation area to the shallower test section a 2 m long wooden ramp (1-in-10 slope) was placed at the start of the sand bed test section. A 100 mm diameter pipe was installed under the sand bed to connect the two ends of the wave flume. This was done to aid in filling the flume and to reduce the effect of wave setup in the flume.

Initially it was proposed to run the experiments with only one type of sand with a 50 percentile grain size diameter (D_{50}) of 242 μm. The flume experiments were established with the whole of the 20 m sand bed composed of this sediment type (refer to Figure 3.1). After a substantial number of initial results were analysed it was decided to replace part of the sand bed with two coarser sand types. Figure 3.2 shows the alternate setup of the wave flume. Two sands were chosen with diameters (D_{50}) of 372 μm and 544 μm. Each of the newer sand beds was 3 metres long and isolated from the original sand by wooden boxing and plastic sheeting. The centres of the two 3 m beds were located at distances of 9 and 12 m from the wave paddle. To aid in the formation of ripples in the coarser sediments, the beds were 50 mm thicker than the original bed. To provide a smooth transition between the deeper and shallower test sections the original bed was used to provide a ramp up to and away from the thicker beds.

A sieve analysis was undertaken for each of the sediment types (refer to Figure 3.3). From Figure 3.3 three characteristic diameters for each sediment were determined, being the 30, 50 and 60 percentile sediment diameters. From these characteristic diameters two sediment parameters were calculated. The phi sediment size defined as:

$$\phi_{50} = -log_2(D_{50}) \tag{3.1}$$

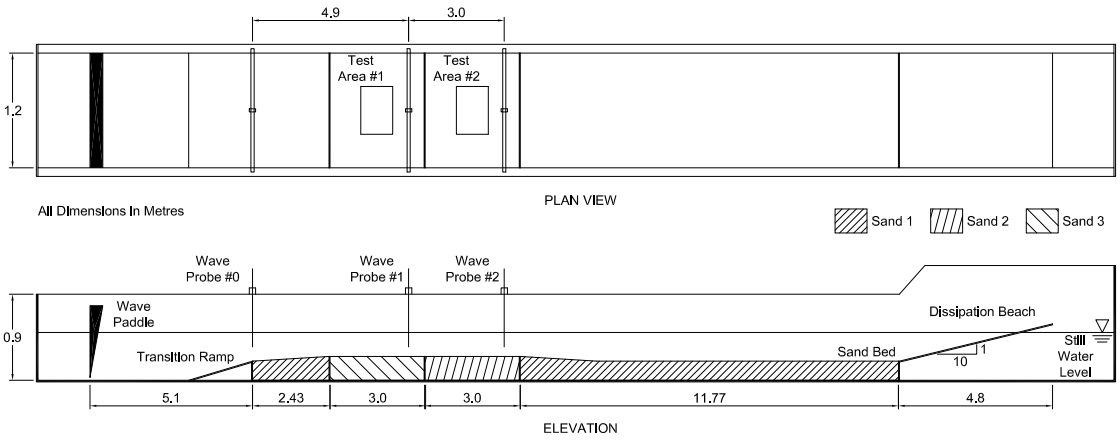

Figure 3.2 Plan and elevation views of the alternate wave flume setup.

where D_{50} is in mm; and a coefficient of uniformity calculated as:

$$C_u = D_{60}/D_{30} \tag{3.2}$$

Table 3.1 lists the sediment parameters for each of the three sediment types.

Table 3.1 Sediment parameters of the three sands used in experiments.

Sand ID	Thickness mm	D_{30} μm	D_{50} μm	D_{60} μm	ϕ_{50} –	C_u –
type 1	200	173	242	282	2.0	1.63
type 2	250	292	372	421	1.4	1.44
type 3	250	491	544	571	0.8	1.16

Of the two newer sand beds used, only one sand type (type 2) formed ripples under the conditions that could be generated in the flume. The bed composed of type 3 (refer to Table 3.1) sand was too coarse. Hence the experiments were only undertaken on two sand beds, the types 1 and 2 beds listed in Table 3.1. The type 3 sediment is included here as it shows that ripples form due to the movement of sand grains, if there is not enough energy within a flow regime to mobilise the sand, stable ripples will not form.

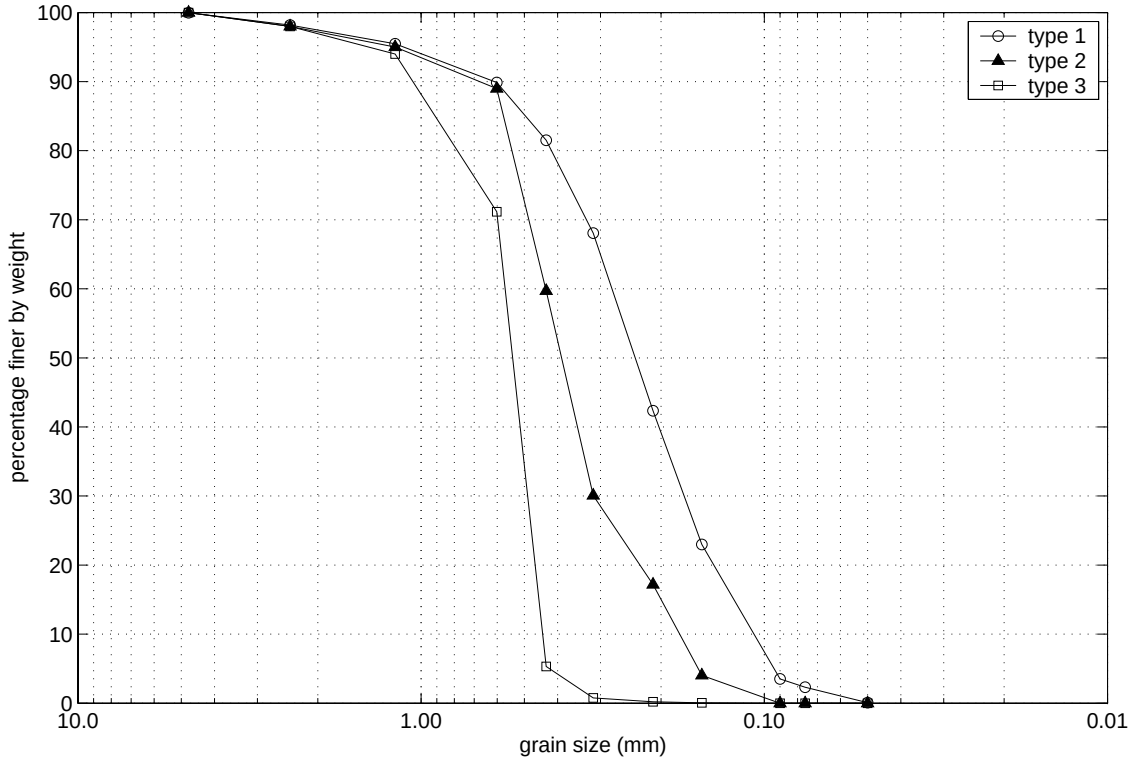

Figure 3.3 Sieve analysis of the three sands used in the experiments.

3.1.3 Ripple Measurement System

To measure the rippled surface underwater, a specialised sediment scanning system was designed and developed as part of this study. As outlined in Section 1.2 this was one of the minor objectives of this research. The ripple measurement system consisted of a laser displacement sensor suspended approximately 95 mm above the sand bed from a computer controlled X-Y positional table. A number of researchers have used various laser based ripple measurements systems successfully in both laboratory and field studies [*Crawford and Hay*, 1998, 2001; *O'Donoghue and Clubb*, 2001; *Moore and Jaffe*, 2002]. The laser measurement system developed by this study allowed the scanning of rippled surfaces underwater and while waves were being run along the flume with minimal disturbance of the rippled surface or the wave boundary layer. The axis along the flume in the direction of wave travel was defined as the primary axis while the secondary axis was defined as the axis across the flume normal to the direction of wave travel. The X-Y positional table

of the ripple measurement system is shown in Plate 3.1.

The laser sensor used was a type "LAS-8010V" visible laser analog sensor made by Nippon Automation Company Ltd. This laser displacement sensor was chosen on the advice of Dr. Tom O'Donoghue of the University of Aberdeen, UK who also used this type of laser displacement sensor to measure rippled beds [*O'Donoghue and Clubb*, 2001]. From the information supplied by the manufacturer the laser sensor has a measurement range of 100 $\pm$ 40 mm and a maximum resolution of 50 μm in the vertical direction. The laser measurement system was chosen over other methods such as acoustic or photographic methods because of the higher accuracy and reliability of the laser measurements compared to the other methods. *Betteridge et al.* [2003] suggest that the acoustic ripple profilers have a vertical measurement error in the order of 5 mm. However, the resolution of acoustic measurement systems may be improved by increasing the acoustic frequency (A.E. Hay, *pers. comm*). Photographic measurements of rippled beds may suffer from poor visibility due to the suspension of sediment particles into the water column [*Amos et al.*, 1988; *Wheatcroft*, 1994]. Based on visual observations of the wave boundary layer and the measurements obtained by the laser sensor it was concluded that the suspension of particles did not dramatically effect the ripple measurements. However, due to the relatively low scale of waves that could be generated the volume of sediment particles being suspended each wave period was small. The vertical resolution of the laser system was determined to be in the order of 0.2 mm. The derivation of this accuracy value will be discussed with relation to the ripple spectrum in Section 4.2.1.

As outlined above, an important requirement of the system was the ability to scan the sediment surface underwater while waves were being run along the flume. To achieve this goal the laser sensor was encased in a clear 80 mm diameter Perspex tube which passed through the air-water interface. Plate 3.2 shows the ripple measurement system measuring ripples underwater while waves were being run along the flume.

Passing the laser beam through the Perspex and the water column above the sediment bed changed the calibration curve of the laser sensor. Figure 3.4 shows the change in the laser head's calibration curve due to the laser beam passing through the Perspex and

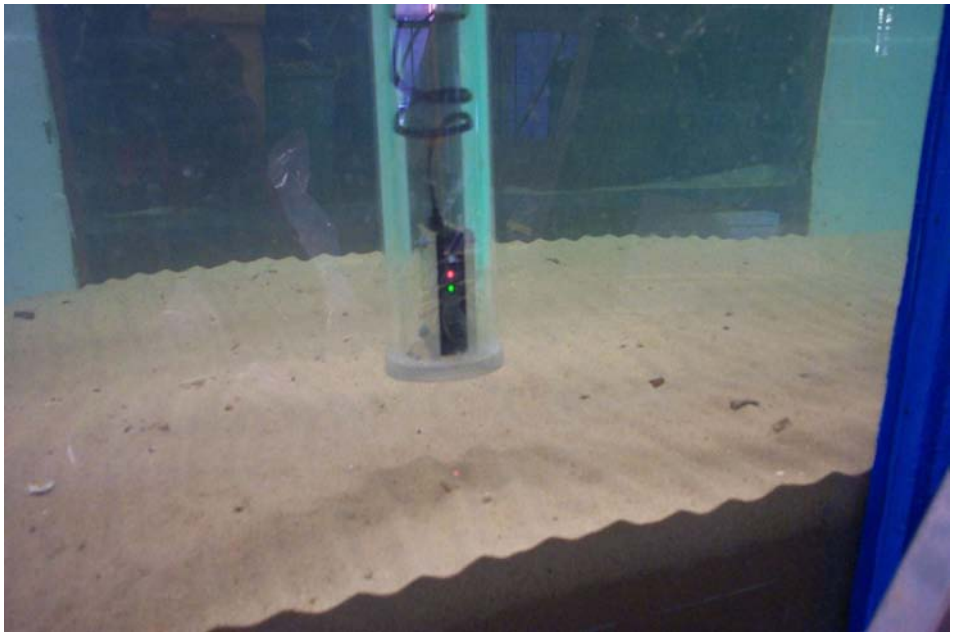

Plate 3.2 The laser head of the ripple measurement system shown underwater. The ripples shown are in the order of 40 mm long.

the water column. The lighter vertical and horizontal dotted lines represent the range of measurements that the manufactures suggest. The bold dotted line represents the standard calibration curve while the bold plain line represents the underwater calibration curve determined during this study. As can be seen in Figure 3.4, the correlation of the underwater calibration curve is very good with a R^2 value of 0.9998. The standard calibration relationship for the laser head as given by the manufacture was:

$$h = 20.0V + 40.0 \tag{3.3}$$

while the underwater calibration relationship for the laser head as determined by this study is:

$$h = 26.738V + 40.537 \tag{3.4}$$

where h is the distance away from the bed (mm) and V is the voltage output from the laser (volts).

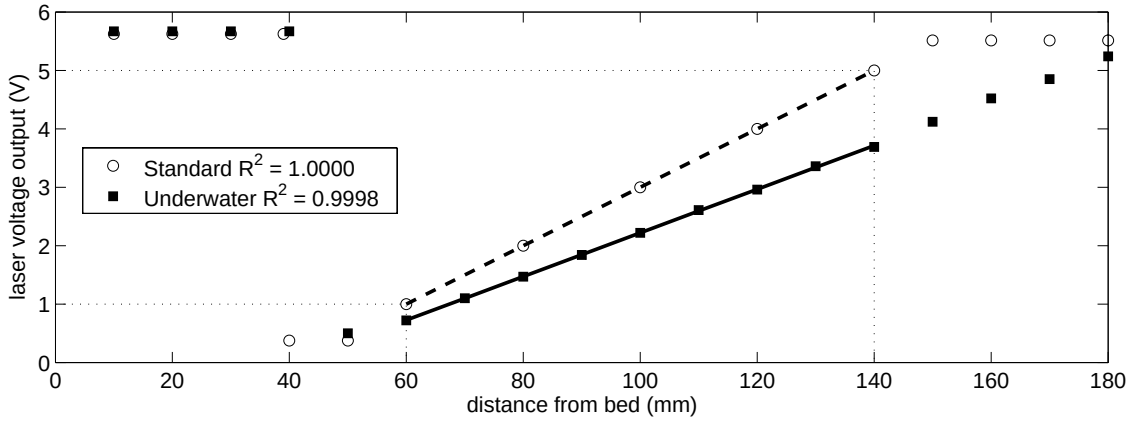

Figure 3.4 Calibration curves for the laser measurement head. The standard laser calibration data is shown as open circles, while the results of the underwater calibration tests are shown as filled squares.

An interesting point of note regarding the underwater calibration data shown in Figure 3.4 is that placing the laser sensor in its Perspex jacket underwater increased the overall measurement range of the instrument. The manufacture suggests that the laser will measure between 60 and 140 mm away from the surface to be measured. However, as shown by the calibration data, the underwater sensor will follow the same linear correlation between 60 and 180 mm away from the bed. This ability was not utilised during this study as the highest ripples measured were approximately 30 mm. It was also felt that it would be safer to keep within the manufacturer's suggested measurement range. Hence the underwater calibration (equation 3.4) was only fitted to the data between values of 60 and 140 mm from the measurement surface.

The computer controlled X-Y positioning table consisted of two carriages each driven via a 5 mm lead screw attached to a 1.8 degree step motor (refer to Plate 3.1). A 5 mm lead screw moves a nut 5 mm along the screw shaft each revolution. The carriages were mounted on shafts and linear bearings made by Linear Bearings Pty Ltd. The X-Y positional accuracy of the unit was constrained by the laser spot diameter, which is in the order of 1 mm. In the process of designing the system a trade off between the speed of the carriages and the accuracy of the positioning had to be made. It was decided to keep a high level of accuracy, but this meant that the speed of the system as it scanned the surface

was quite slow. To scan an 1 m length of the bed took approximately 80 seconds. For a full two-dimensional scan of a 1 m^2 area at a secondary spacing of 10 mm took approximately 2 hours. This did not constrain the accuracy of measurements because once formed the ripples were found to be very stable in this type of sediment. Appendix E provides extra details and specifications of the ripple measurement system.

The horizontal resolution of the ripple measurement system was determined to be less than 4 mm. As with the vertical resolution the derivation of this accuracy value will be discussed with relation to the ripple spectrum in Section 4.2.1.

3.2 EXPERIMENTAL METHOD AND TESTS

The experiments undertaken for this research project set out to examine the three phases of ripple development in terms of their spectral characteristics and relate these characteristics to flow conditions and sediment properties. The three phases were the growth of ripples from a no-ripple bed condition, the equilibrium form of rippled beds, and the evolution of ripples moving between two equilibrium states. This section will outline the experimental methods employed to achieve each of the these goals.

The three types of experiments (growth, equilibrium and transition) were run one after the other as a series of tests. This was done to maximise the collection of data over a set time period. Before one can measure an equilibrium rippled bed, the bed has to develop and come to equilibrium with the surface wave conditions. This takes time and while it is developing the sediment surface can be scanned to produce a time series of ripple evolution. The term for a sediment bed that has no ripples will be referred to within this thesis as a no-ripple condition. This is in preference to calling the bed *flat* as sediment beds are never flat, but will always have some level of background roughness.

3.2.1 Growth Tests

The growth tests were started with the sediment bed in a no-ripple condition by raking the bed to remove any ripples present from previous experiments. Ripples were formed

on the sediment surface by running irregular waves conforming to a standard JONSWAP ($\gamma = 3.3$) spectrum along the flume for a period of 2.5 hours. After this time the waves and rippled bed were considered to be at equilibrium (an assumption to be tested and discussed further in Chapter 6). As the rippled bed was developing a long section of the rippled bed along the centreline of the flume was scanned every 5 minutes using the ripple measurement system. Scans were taken at the test area #1 (TA1) shown in Figure 3.1 and at the test area #2 (TA2) shown in Figure 3.2. Each long sectional scan was 1000 mm long with a primary spacing of 1.56 mm which gave a total of 640 data points taken from the sediment surface as a one-dimensional scan. This provided 31 long sections in total, which showed the growth of the rippled bed from a no-ripple condition over time. Figure 3.5 shows an example of the data that were obtained from the ripple growth tests. This bed was formed using irregular waves with a peak frequency (f_p) of 0.8 Hz, a significant wave height (H_s) of 82 mm with a sediment diameter (D_{50}) of 372 μm.

Wave conditions for the growth tests were monitored from the probe located directly behind the test area where the bed was scanned (refer to Figures 3.1 and 3.2). This probe was placed at a distance of 1 m behind the centre of the test section. The whole of the 2.5 hour period was recorded and used to produce a frequency spectrum of the surface waves from which flow conditions could be calculated. The probes were sampled with a frequency of 8 Hz which gave surface wave spectral estimates (using a data window of 256 data points) with over 500 degrees of freedom for the 2.5 hour tests.

Table 3.2 lists the experimental growth tests undertaken. The first column in Table 3.2 lists the experiment identification code. The peak bottom orbital velocity (U_p) and peak orbital excursion diameter (d_{op}) which will be used in subsequent chapters were calculated from the root mean squared (rms) velocity (U_{rms}), shown in Table 3.2. The rms velocity was determined from the surface wave spectrum using a method outlined by *Soulsby* [1987]. *Soulsby* [1987] calculated the velocity variance spectrum from the water surface spectrum through the use of a dimensional transfer function given as:

$$S_u(\omega) = \frac{\omega^2}{sinh^2(kh)} S_w(\omega) \tag{3.5}$$

where S_u is the velocity variance spectrum (m^2/s), ω is the angular frequency (rad/s), k

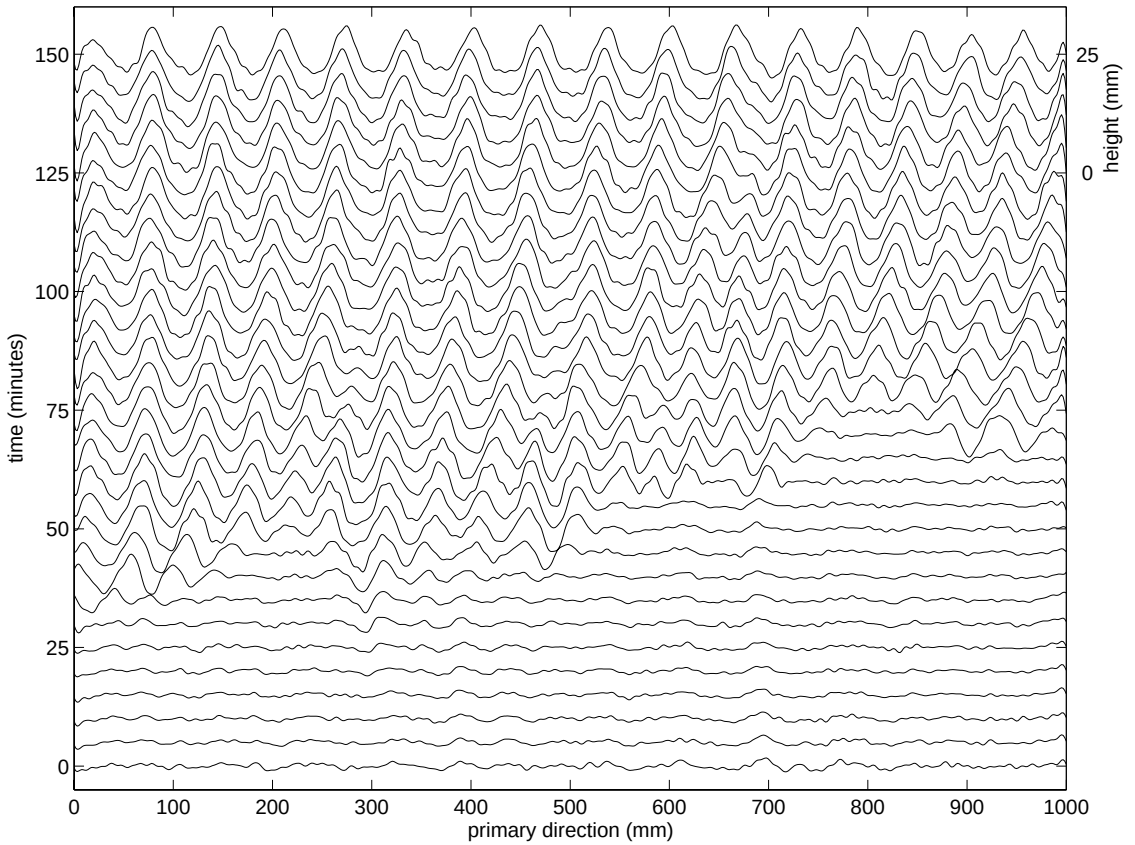

Figure 3.5 Example plot showing typical ripple growth with time ($\Delta t = 5\,mins$). Surface waves are moving from left to right across the bed. Left hand axis indicates the test time while the upper right hand axis provides a scale of ripple height.

is the wavenumber (rad/m), h is the water depth (m) and S_w is the variance spectrum of the surface waves (m^2/Hz). From equation 3.5 *Soulsby* [1987] calculated the rms velocity by integrating S_u over the angular frequency and taking the square root.

$$U_{rms} = \sqrt{\int_0^\infty S_u(\omega)\, d\omega} \tag{3.6}$$

where U_{rms} is the root mean squared velocity (m/s). Equation 3.6 is the method used by spectral wave models such as SWAN [*Booij et al.*, 1999; *Ris et al.*, 1999] to calculate the rms velocity. From equation 3.6 the peak bottom orbital velocity is scaled as:

$$U_p = 1.42\sqrt{2}U_{rms} \tag{3.7}$$

which is equivalent to a using the significant wave height to calculate the bottom orbital velocity [*Traykovski et al.*, 1999]. The peak orbital excursion diameter was calculated from the peak bottom orbital velocity as:

$$d_{op} = U_p/(\pi f_p) \tag{3.8}$$

where f_p is the peak surface wave frequency (Hz).

The dimensionless variables listed in Table 3.2 were calculated from standard linear theory and are included to provide a scale of the flow parameters compared with sediment parameters. The sediment Reynolds number ($\Re_d$) was calculated, using the D_{50} of the sediment as a length scale, as:

$$\Re_d = \frac{U_o D_{50}}{\nu} \tag{3.9}$$

where U_o is the orbital velocity calculated from linear theory (m/s) and ν is the kinematic viscosity (m^2/s). The flow Reynolds number ($\Re$) used the orbital excursion amplitude ($d_o/2$) as a length scale and was calculated as:

$$\Re = \frac{U_o d_o}{2\nu} \tag{3.10}$$

where d_o is the orbital excursion diameter calculated from linear theory (m). The Shields number (ϑ) was calculated using the skin friction roughness and as such does not take into account ripple forms which were changing during this test (refer to equation 2.6, page 14). The grain roughness friction factor (f_w) was calculated using the relationship of *Swart* [1974] with a roughness height of $2.5D_{50}$. The grain roughness friction factor was calculated as:

$$f_w = \exp\left(5.213\left[\frac{2.5D_{50}}{d_o/2}\right]^{0.194} - 5.977\right) \tag{3.11}$$

The period parameter (χ refer to equation 2.17, page 16) and the mobility number (ψ refer to equation 2.1, page 13) was calculated using the D_{50} of the sediment. The data set shown in Figure 3.5 is listed as test GO5 in Table 3.2.

Table 3.2 Summary of the ripple growth tests undertaken.

Growth	Water	Sand	Wave Parameters			Dimensionless Variables					
Test ID	Depth	D_{50}	f_p	H_s	U_{rms}	$\Re_d$	$\Re$	ϑ	ψ	d_o/D_{50}	χ
	m	μm	Hz	m	m/s	–	–	–	–	–	10^5
G01	0.286	242	0.80	0.079	0.076	41.7	5882	0.105	7.6	250.2	0.968
G02	0.184	242	0.80	0.067	0.091	49.7	8368	0.137	10.8	299.1	0.964
G03	0.187	242	0.80	0.070	0.094	51.3	8906	0.144	11.5	309.9	0.962
G04	0.205	372	0.80	0.083	0.106	87.5	11035	0.133	9.2	229.4	1.463
G05	0.208	372	0.80	0.082	0.104	85.8	10618	0.129	8.8	224.4	1.464
G06	0.287	242	0.84	0.082	0.077	41.9	5676	0.107	7.6	240.9	1.053
G07	0.287	242	0.84	0.082	0.077	42.0	5713	0.108	7.7	241.7	1.054
G08	0.282	242	0.99	0.095	0.084	42.3	4927	0.118	7.8	223.4	1.463
G09	0.288	242	0.99	0.092	0.078	40.0	4373	0.108	7.0	208.7	1.474
G10	0.205	372	0.99	0.093	0.111	86.8	8778	0.146	9.0	193.0	2.237
G11	0.184	372	0.99	0.080	0.103	81.9	7823	0.133	8.0	180.5	2.232
G12	0.284	242	0.99	0.089	0.078	39.2	4199	0.105	6.7	206.5	1.479
G13	0.289	242	1.00	0.091	0.078	39.4	4249	0.106	6.8	208.1	1.481
G14	0.288	242	1.00	0.091	0.078	39.2	4193	0.105	6.7	206.4	1.489
G15	0.288	242	1.04	0.089	0.073	36.8	3550	0.097	5.9	187.0	1.604
G16	0.186	242	1.18	0.065	0.074	37.2	3169	0.106	6.0	165.9	2.100
G17	0.183	242	1.18	0.065	0.076	37.9	3298	0.109	6.3	169.0	2.092
G18	0.154	372	1.14	0.075	0.104	80.5	6523	0.140	7.8	155.6	3.008
G19	0.184	372	1.14	0.080	0.095	73.2	5404	0.122	6.4	142.9	2.987
G20	0.288	242	1.22	0.076	0.049	23.5	1231	0.055	2.4	106.1	2.216

3.2.2 Equilibrium Tests

Once the rippled bed had come to an equilibrium with the surface wave conditions, the waves were stopped and a number of two-dimensional equilibrium grids were scanned at the test areas shown in Figures 3.1 and 3.2. Each two-dimensional scan consisted of 51 one-dimensional long sections with a spacing of 10 mm in the secondary direction taken in the direction of wave travel along the sand bed. Each long section consisted of 512 data points with a spacing of 2 mm and a total length of 1022 mm. This provided 26,112 three-dimensional data points taken from the rippled surface. Figure 3.6 presents an example of the data obtained from the equilibrium scans using the ripple measurement system. The rippled sediment bed presented in Figure 3.6 was formed under irregular waves conforming to a standard JONSWAP spectrum with a f_p of 1.0 Hz, a H_s of 98 mm and using a D_{50} of 242 μm.

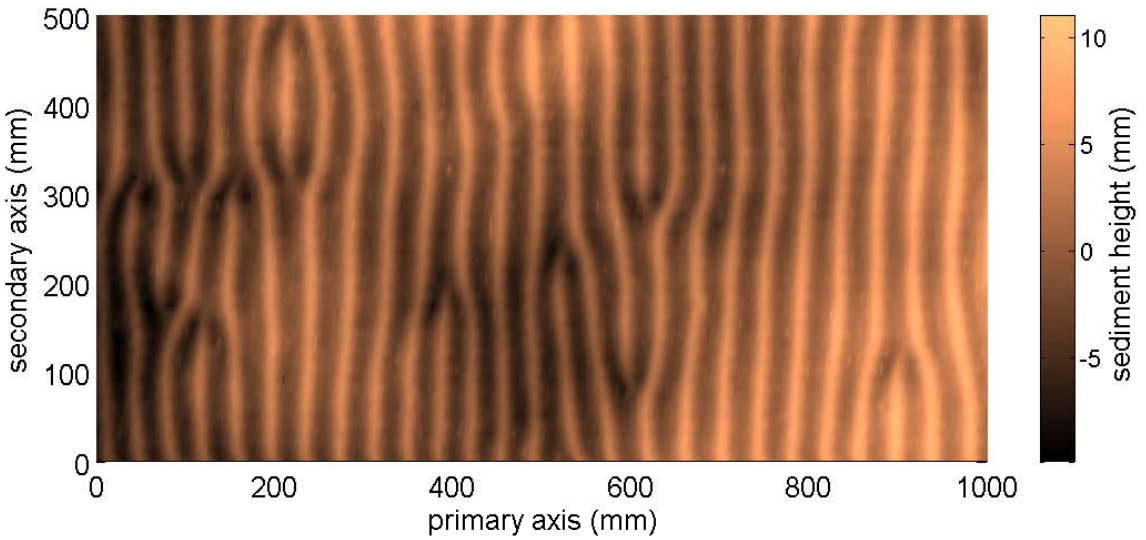

Figure 3.6 Example plot showing an equilibrium rippled bed measured by the ripple measurement system. Primary axis is along the flume in the direction of wave travel.

Equilibrium scans were undertaken after either a 2.5 hour growth test or a 2.0 hour transition test. So that the measured wave conditions where representative of the conditions to which the rippled bed had attained equilibrium, the last 30 minutes of the water surface record was utilised. As with the growth tests the wave conditions for a given bed were monitored from the probe located directly behind the test area where the bed was scanned (refer to Figures 3.1 and 3.2). The probes were sampled with a frequency of 8 Hz which gave a surface wave spectral estimate (using a data window of 256 data points) with over 120 degrees of freedom for the equilibrium tests.

Table 3.3 lists the equilibrium tests undertaken. The first column in Table 3.3 lists the experiment identification code. TA relates to test area 1 to 4 used to measure equilibrium ripple parameters (refer to Figures 3.1 and 3.2). All other variables listed in Table 3.3 were calculated in the same way as outlined for Table 3.2. Note that Figure 3.6 was developed from data gained in an initial test undertaken to established the ripple measurement system, as such the details of this test do not appear in Table 3.3.

Table 3.3 Summary of the equilibrium tests undertaken.

Equilibrum	Water	Sand	Wave Parameters			Dimensionless Variables					
Test ID	Depth	D_{50}	f_p	H_s	U_{rms}	$\Re_d$	$\Re$	ϑ	ψ	d_o/D_{50}	χ
	m	μm	Hz	m	m/s	–	–	–	–	–	$\times 10^{-5}$
E01_TA1	0.185	242	1.18	0.065	0.136	37.4	3225	0.107	6.1	166.7	2.154
E02_TA1	0.286	242	0.80	0.079	0.155	42.0	5954	0.105	7.7	285.9	0.957
E02_TA4	0.313	242	0.81	0.071	0.126	34.7	4033	0.079	5.2	237.6	0.957
E03_TA1	0.185	242	1.18	0.066	0.133	37.4	3220	0.107	6.1	167.0	2.154
E03_TA4	0.213	242	1.16	0.057	0.116	28.7	1930	0.071	3.6	124.1	2.154
E04_TA1	0.285	242	0.81	0.078	0.159	41.4	5788	0.104	7.5	283.1	0.957
E04_TA4	0.313	242	0.80	0.071	0.130	34.9	4119	0.079	5.3	237.2	0.957
E05_TA1	0.183	242	1.18	0.066	0.139	37.9	3304	0.109	6.3	169.4	2.154
E06_TA1	0.283	242	0.81	0.079	0.162	42.2	5992	0.106	7.7	287.8	0.957
E07_TA1	0.183	242	1.18	0.065	0.139	37.8	3282	0.108	6.2	168.2	2.154
E07_TA4	0.195	242	1.17	0.061	0.123	33.5	2605	0.090	4.9	147.1	2.154
E08_TA1	0.282	242	0.81	0.092	0.183	49.2	8172	0.135	10.6	335.7	0.957
E08_TA2	0.296	242	0.80	0.088	0.167	45.2	6904	0.118	8.9	308.1	0.957
E08_TA3	0.301	242	0.80	0.082	0.155	41.8	5913	0.105	7.6	284.5	0.957
E09_TA1	0.283	242	0.99	0.095	0.163	42.0	4833	0.116	7.7	226.1	1.496
E09_TA2	0.292	242	0.98	0.091	0.159	39.6	4334	0.106	6.8	210.1	1.496
E09_TA3	0.297	242	0.97	0.086	0.154	37.1	3846	0.096	6.0	195.0	1.496
E09_TA4	0.308	242	0.97	0.084	0.140	34.9	3424	0.087	5.3	182.3	1.496
E10_TA1	0.184	242	0.80	0.067	0.177	49.6	8356	0.136	10.7	337.1	0.957
E10_TA2	0.195	242	0.80	0.060	0.141	43.0	6273	0.109	8.1	292.5	0.957
E10_TA3	0.201	242	0.82	0.057	0.121	39.2	5122	0.096	6.7	268.6	0.957
E10_TA4	0.209	242	0.82	0.053	0.106	35.5	4187	0.082	5.5	243.2	0.957
E11_TA1	0.187	242	0.80	0.070	0.200	51.1	8829	0.143	11.4	347.8	0.957
E11_TA2	0.195	242	0.80	0.063	0.161	45.0	6866	0.117	8.8	305.7	0.957
E11_TA3	0.200	242	0.81	0.059	0.133	41.2	5668	0.103	7.4	281.7	0.957
E11_TA4	0.209	242	0.83	0.055	0.110	36.4	4332	0.086	5.8	252.2	0.957
E12_TA1	0.287	242	0.99	0.092	0.155	40.0	4360	0.108	7.0	215.8	1.496
E12_TA2	0.298	242	0.99	0.088	0.147	36.7	3693	0.095	5.9	197.3	1.496
E12_TA3	0.302	242	0.98	0.084	0.144	35.1	3409	0.088	5.4	186.4	1.496
E12_TA4	0.311	242	0.98	0.081	0.135	33.2	3065	0.081	4.8	174.7	1.496
E13_TA2	0.205	372	0.78	0.081	0.211	86.3	10956	0.129	8.9	245.8	1.471
E14_TA2	0.204	372	0.98	0.083	0.191	78.7	7311	0.125	7.4	177.8	2.299
E15_TA2	0.150	372	1.17	0.066	0.170	71.7	5059	0.120	6.2	134.6	3.311
E16_TA2	0.207	372	0.79	0.078	0.202	81.9	9743	0.120	8.0	234.3	1.471
E17_TA2	0.193	372	1.14	0.074	0.145	64.7	4237	0.101	5.0	139.5	2.782
E18_TA2	0.203	372	0.79	0.075	0.191	80.7	9532	0.117	7.8	230.4	1.471
E19_TA2	0.184	372	1.14	0.073	0.150	67.1	4541	0.107	5.4	144.6	2.782
E20_TA2	0.208	372	0.79	0.076	0.192	80.5	9476	0.116	7.8	229.7	1.471
E21_TA2	0.183	372	1.14	0.072	0.144	66.8	4515	0.106	5.4	144.1	2.782
E22_TA2	0.183	372	0.99	0.074	0.175	76.0	6711	0.120	6.9	173.8	2.299

3.2.3 Transition Tests

The transition tests were started with remnant equilibrium ripples already present on the surface from a previous experiment, either from a growth test or from a previous transition test, which had been generated using different surface wave conditions. The wave conditions were changed and irregular waves were run over this bed for a period of 2.0 hours until the ripples had once more come to an equilibrium with the surface wave conditions. As with the growth tests a one-dimensional sediment scan was taken every 5 minutes along the centreline of the flume. Transition tests provided 25 long sections of the rippled surface as the rippled bed transitioned to a new equilibrium configuration.

Figure 3.7 presents two examples of the data obtained from the ripple transition tests. Please note that both of these beds had a scanning length of 1000 mm, but have been reduced to 400 mm so that they could be presented here side by side. Both tests shown in Figure 3.7 were formed using irregular waves with a sediment size (D_{50}) of 345 μm. Figure 3.7a shows a rippled bed evolving from a higher energy state back to a lower energy state. The wave conditions that formed the original bed had a f_p of 0.8 Hz and a H_s of 82 mm, while the wave conditions that caused to bed to change had a f_p of 1.2 Hz and a H_s of 80 mm. Figure 3.7b shows the opposite condition with the bed evolving from a lower energy state up to one with a higher energy state. The wave conditions that originally formed the bed had a f_p of 1.2 Hz and a H_s of 80 mm, while the wave conditions that changed the bed had a f_p of 0.8 Hz and a H_s of 80 mm.

Wave conditions for the transition tests were monitored exactly the same way as the ripple growth tests. The 2.0 hour time series was recorded and used to produce a surface wave frequency spectrum. The probes were sampled with a frequency of 8 Hz which gave a surface wave spectral estimate (using a data window of 256 data points) with approximately 450 degrees of freedom for the transition tests.

Table 3.4 lists the experimental tests undertaken to observe ripple transition. The first column in Table 3.4 lists the experiment identification code. The second column gives the test ID of the experimental test that formed the original rippled bed. The test ID shown starting with a "G" (Growth) are listed in Table 3.2 while those starting with a

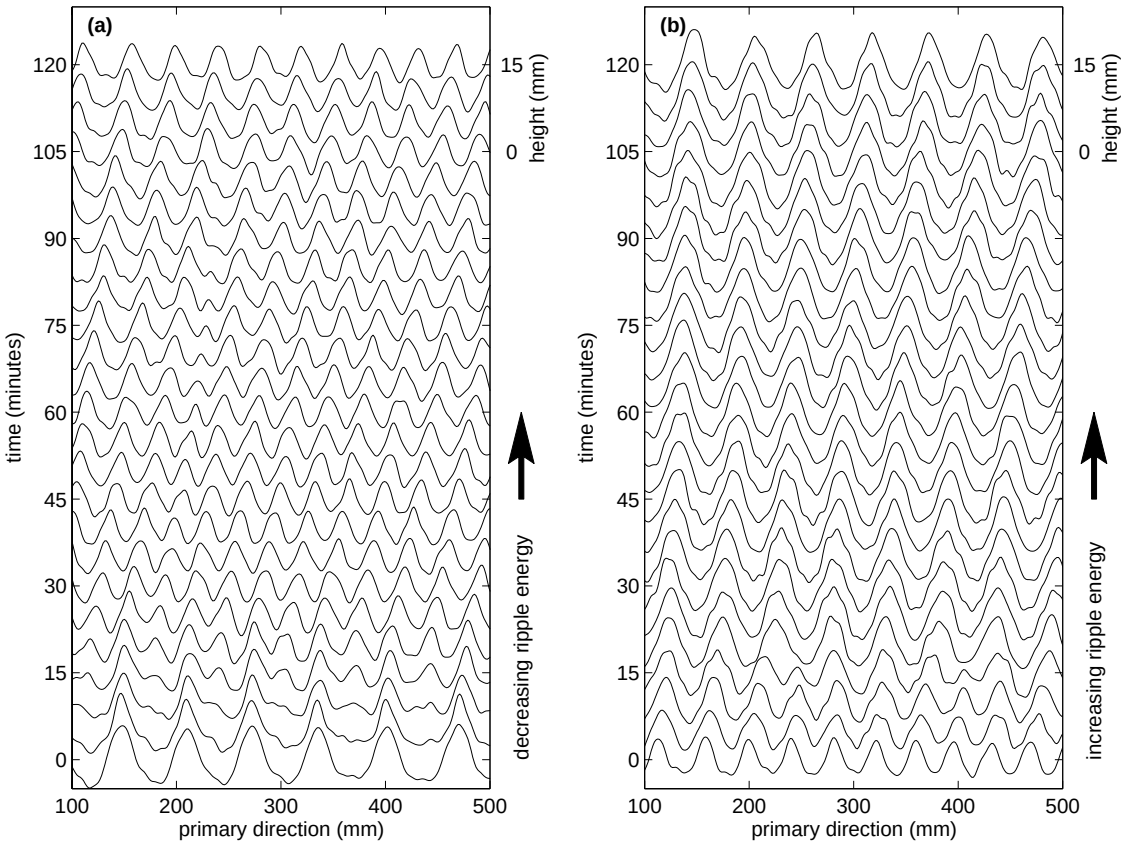

Figure 3.7 Example plot showing typical ripple transition under the action of surface waves that are out of equilibrium with the rippled bed ($\Delta t = 5\,mins$). Subplot (a) shows the change in the rippled bed as the ripple energy is decreasing, while (b) shows the change in the rippled bed as the ripples energy is increasing.

"T" (Transition) are listed in Table 3.4. All other parameters shown in Table 3.4 were calculated in the same way as outlined for Tables 3.2 and 3.3.

3.3 SPECTRAL DEFINITIONS AND SPECTRAL STABILITY

This section will outline two very important discussions of this study that do not fit into the previous two sections: the spectral definitions that have been adopted and the stability of the surface wave spectra over the extended ripple growth and transition test periods.

Table 3.4 Summary of the ripple transition tests undertaken.

Transition	Original	Water	Sand	Wave Parameters			Dimensionless Variables					
Test ID	Test ID	Depth	D_{50}	f_p	H_s	U_{rms}	$\Re_d$	$\Re$	ϑ	ψ	d_o/D_{50}	χ
		m	μm	Hz	m	m/s	–	–	–	–	–	10^5
T01	G01	0.187	242	1.18	0.065	0.074	37.0	3152	0.105	6.0	165.6	2.074
T02	G07	0.287	242	1.22	0.075	0.049	23.5	1231	0.055	2.4	105.6	2.211
T03	G05	0.193	372	1.15	0.080	0.091	69.7	4882	0.114	5.8	136.1	3.016
T04	T08	0.184	372	1.15	0.081	0.096	73.6	5437	0.123	6.5	143.3	3.020
T05	T01	0.287	242	0.81	0.078	0.075	41.3	5753	0.103	7.4	247.4	0.971
T06	G17	0.284	242	0.81	0.079	0.077	42.1	5967	0.106	7.7	251.8	0.970
T07	T03	0.204	372	0.80	0.080	0.104	85.3	10506	0.128	8.7	223.8	1.458
T08	G19	0.208	372	0.80	0.081	0.103	85.2	10482	0.128	8.7	222.8	1.458
T09	G20	0.288	242	0.84	0.083	0.078	42.6	5886	0.110	7.9	245.6	1.053

3.3.1 Spectral Definitions

After a review of the spectral analysis literature had been completed it became evident that there are some slight inconsistencies between definitions of different types of spectra. This study measured two types of series: a time series (the water waves) and a spatial series (the rippled bed). From these series there are three types of spectra that can be calculated: a power; an amplitude or a variance spectrum.

The base type is a power spectrum which in this study, has the units of m^2 for the spectra calculated from both types of series. The power spectral estimate was calculated using the power-spectral-density PSD routine within MATLAB's Signal Processing Toolbox (Mathworks, Signal Processing Toolbox, available at www.mathworks.com, 2002). The PSD routine utilises Welch's averaged, modified periodogram method and allows the user to select the length and type of the data window. This study used a Hamming window of variable lengths to calculate the spectra of both types of series. The second type of spectrum is an amplitude spectrum with units of m and is scaled from the power spectrum by taking the square root of the power spectrum. The third type, and the one most utilised by this study, is the variance spectrum with units of (m^2/Hz) if calculated from a time series or ($m^2/m^{-1} \Rightarrow m^3$) if from a spatial series. A variance spectrum is scaled from a power spectrum by:

$$S = \frac{P}{F_s/2} \tag{3.12}$$

where S and P are the variance and power spectrum respectively and F_s is the sample frequency either in Hz if the spectrum is calculated from a time series or in $1/m$ if is calculated from a spatial series. The variance spectrum has the advantage that the area under the spectral curve is equal to the variance of the series [*Young*, 1999].

3.3.2 Stability of the Water Surface Spectrum

An important issue in calculating the water surface spectrum from a long time series, as done with the ripple growth and transition tests, is determining how stable the resulting spectrum is likely to be over the extended test period. Any change in the surface wave

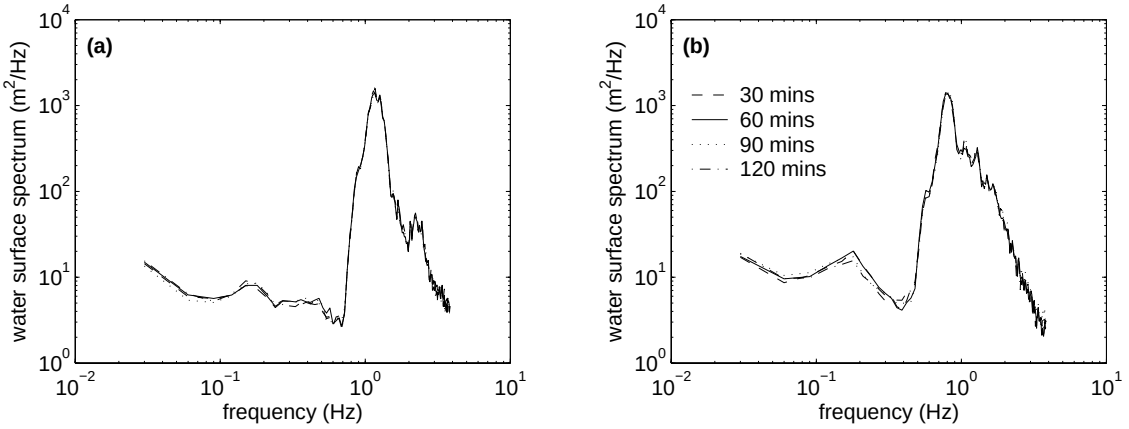

Figure 3.8 Stability of the surface wave spectra. The spectra shown were calculated at various times during a 2.0 hour ripple transition test using a 30 minute data window.

spectrum as the ripples are in the process of developing will cause unrealistic results, through the use of an unrepresentative surface wave spectrum used to calculate flow parameters.

As part of a preliminary check of the experimental data the surface wave spectrum was calculated for different times during the test period and compared. Figure 3.8 shows the results of two such checks for two different surface wave conditions. To form this figure a surface wave spectrum was calculated for every 30 minute period of a 2 hour ripple transition test using the time series data from the 30 minute interval. For example, the 30 min series shows the water spectrum calculated for the first 30 minutes of the test, the 60 min series shows the spectrum calculated for the next 30 minute period and so on.

The spectra shown in Figure 3.8 are the water surface spectrum used to form the rippled beds of the two transition tests shown in Figure 3.7. Figure 3.8a relates to the ripples shown in Figure 3.7a and it shows a surface wave condition with a peak frequency of 1.2 Hz and significant wave height of 80 mm. Figure 3.8b relates to the ripples shown in Figure 3.7b and it shows a surface wave condition with a peak frequency of 0.8 Hz and significant wave height of 80 mm.

The water surface spectra were very stable over the two hour test period (refer to Figure 3.8). The peak frequency, peak spectral density and the area for all the spectra remained at the same levels during the test with no appreciable difference between the

four water surface spectra shown in either of the two subplots. This result was typical of the stability checks that were undertaken at the end of each test.

3.4 SUMMARY AND DISCUSSION

The laboratory equipment was introduced and discussed in Section 3.1 of this chapter. Overall the equipment worked extremely well. The use of the *HR WaveMaker Wave generation control program* enabled a range of irregular waves to be generated with extremely stable spectral properties. The dissipation beach, designed for this study, effectively dampened wave reflections which allowed the ripple tests to be run over extended periods without reflected noise contaminating the water surface spectrum. After initial equilibrium test results were analysed two coarser sand beds were installed in the flume to incorporate sand bed properties into the data analysis. However, the bed composed of type 3 (refer to Table 3.1) sand was too coarse to form ripples under the conditions that could be generated in the wave flume. Hence the experiments were only undertaken on two sand beds being the type 1 and type 2 beds listed in Table 3.1. A ripple measurement system was designed and developed to scan the rippled surface underwater while waves were being run along the flume. This system worked exceptionally well and gave the ability to undertake highly accurate and reliable measurements of the rippled bed as a whole with minimal disturbance to the wave boundary layer or the ripple forms. However, the time it took the ripple measurement system to scan a given two-dimensional equilibrium grid was an issue. The time required to undertake a two-dimensional scan did not affect the ability of the system to measure rippled beds that were characteristic of the flow conditions, but it did mean that each test was substantially longer than would otherwise have been the case. Hence, a useful modification would be to increase the speed of the system by redesigning the electronic components.

The experimental method that was undertaken is presented in Section 3.2. The method was introduced as three separate types of experimental tests: ripple growth, equilibrium and transition tests. These test are separate parts of a series of tests that were undertaken on any given day. The bed was raked flat, ripples grown for a period of 2.5 hours

and a number of two-dimensional equilibrium scans were measured once the waves were stopped. After the scan had been completed the wave conditions were started with new properties and the rippled bed allowed to transition to a new equilibrium state over a period of 2.0 hours. The waves were once again stopped and up to 4 two-dimensional equilibrium scans were measured again. Each series of tests could take up to 8 to 10 hours by the time the two-dimensional scans were completed. One-dimensional scans were taken every 5 minutes throughout the ripple growth and transition test periods. Sampling the bed every 5 minutes provided suitable resolution to determine ripple dynamics, and was a comfortable time period for the ripple measurement system to undertake a one-dimensional scan and return to its starting position.

As outlined at the start of this chapter the wave flume at The University of Adelaide had not been used for a number of years prior to the current work being undertaken. This required a substantial number of preliminary tests to determine the characteristics of the wave flume. This has added to the study as nothing has been assumed prior to the test being undertaken.

The experimental procedure worked very well and enabled this study to undertake highly accurate measurements of rippled beds changing from one equilibrium state to another as a time series. These measurements were undertaken while waves were being run continuously along the flume. To the author's knowledge these types of detailed measurements on ripple transients have not be undertaken previously.

Chapter 4

Rippled Bed Parameterisation

As discussed in Chapter 2, the main inadequacy with present ripple prediction methods is that they fail to take into account the substantial spatial variation that is evident on rippled beds formed under real sea conditions. This is largely due to the way these methods parameterise rippled beds in terms of their characteristic ripple height and length.

As measurement methods have improved there has been a general increase in the amount of data that can be gained from a given rippled bed. A number of recent studies regarding wave-formed ripples have presented not only single ripple parameters such as heights and lengths, but also ripple parameter histograms and statistics [*Hanes et al.*, 2001; *Williams et al.*, 2004]. These studies have shown the substantial variability of rippled beds formed under irregular waves both in laboratory and field settings. However, this added measurement capability has not flowed on to the development of a rippled bed parameterisation that takes into account the inherent variability of wave-formed ripples. This study sets out to address this by presenting a new approach to describe rippled sediment beds formed under the action of shallow water irregular waves in terms of their spectral density function. The use of spectral analysis allows rippled beds to be described concisely in terms of their major spatial frequency components. This allows a parameterisation of the bed to be developed which takes into account the inherent variability of ripple parameters across an area of the rippled surface. The spectral parameterisation developed in this chapter will be used to predict and model the transition of rippled beds in subsequent chapters.

This chapter is broken up into two main sections. The first section highlights the inherent variability of rippled beds formed under the action of irregular waves. This is done by examining the variability of the ripple parameters measured by this study and those presented by *Williams et al.* [2004]. *Williams et al.* [2004] is one of the few studies found that have presented the standard deviation as well as the characteristic ripple parameters in their results. The second section introduces the spectral method used to develop a new rippled bed parameterisation. The spectral method developed takes into account ripple variations across an area of the bed, which facilitates the inclusion of this variability into the analysis of rippled beds. Issues such as the calculation and filtering of the bottom surface spectrum will be discussed in this section. Two spectral shape parameters will be defined at the end of the second section, being a spectral width factor and a spectral peakedness parameter. These parameters will be tested to see if they provide any insight into the dependence of the shape of the ripple spectrum against the flow and sediment conditions used in the experimental tests. The chapter will conclude with a review of the effectiveness of the spectral parameterisation method.

Throughout this chapter the example rippled bed, Figure 3.6 (page 56), will be used as a specific example to highlight the calculation method. The 40 equilibrium tests presented in Table 3.3 (page 57) will be used to develop relationships.

4.1 TRADITIONAL PARAMETERISATION

Traditional methods to parameterise ripple beds involve the determination of a characteristic ripple height and length from the rippled surface. As outlined in Section 2.1.2, a substantial number of previous studies have indicated that ripple fields formed in shallow water under real sea conditions will have considerable spatial and temporal variation in their parameters. Any given rippled bed will have a distribution of ripple heights and lengths at any given time. *Wheatcroft* [1994] investigated the distribution of sea floor elevations for a number of bed configurations at a site in 90 m of water. He determined that the roughness elements on the seafloor follow a Gaussian or normal distribution and as such, higher moments such as skewness and kurtosis were not required to describe the

elevation distribution. Apart from *Wheatcroft* [1994] there has been little work undertaken to quantify the spatial variation of rippled beds in terms of their characteristic ripple height and length.

This section will start by presenting a method used to calculate histograms of the ripple heights and lengths from the rippled surface using the zero up-crossing method as outlined by *Goda* [2000]. The inherent variability of ripple parameters will then be discussed. This discussion will focus on two sets of experimental results: a set measured by this study and a set presented in *Williams et al.* [2004]. These data sets show the spatial variation of rippled beds formed under constant irregular surface waves in laboratory conditions. The experiments represent a best case scenario in terms of creating a uniform bed. Other complicating factors that are present in shallow seas, such as remnant ripples, benthic organisms, currents, and the directional spread of the surface wave field are not present in the flume based experiments. However, as will be shown there is still substantial variation evident in the ripple parameters.

4.1.1 The Ripple Histogram

The example ripple bed shown in Figure 3.6 displays ripples that are generally long crested and uniform, however, at a number of locations the straight ripples separate with new ripples forming in-between the spacings. This separation of the ripples cause the surrounding ripples to change their directions and spacings to account for the reduction of space on the bed. Under the current theory of wave formed ripples there is no process to account for such deviations, however they are likely to be due to random fluctuations in the flow field and/or sediment properties. The natural fluctuations in the ripple length due to the random nature of the flow field and sediment properties gives the rippled bed its inherent characteristic variation.

From the data contained in the measured array shown in Figure 3.6 a histogram of the rippled surface can be developed. As outlined above the ripple histogram was formed using the zero up-crossing method as outlined by *Goda* [2000]. A schematic of this method is presented in Figure 4.1.

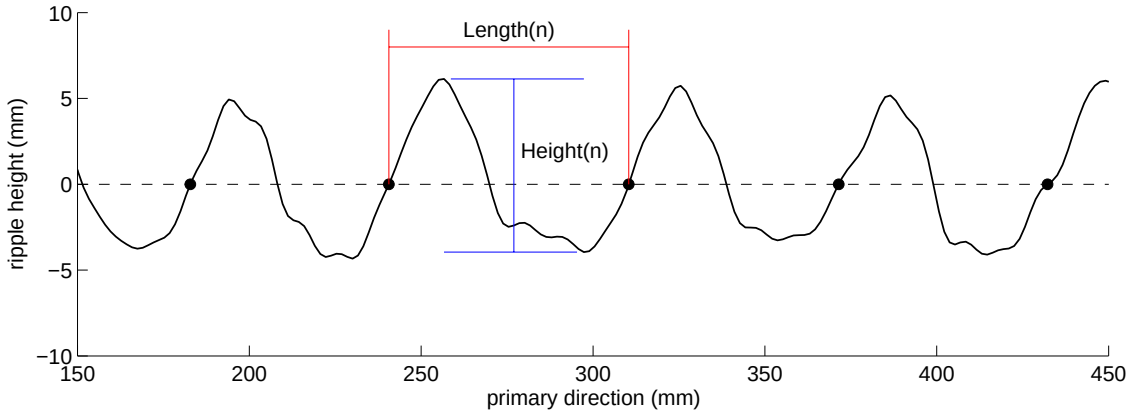

Figure 4.1 A schematic of the zero up-crossing method used to calculate rippled bed parameters. The ripple profile shown is a real rippled bed profile measured by the ripple measurement system.

To form the ripple surface histogram the two-dimensional data array is first broken up into a series of one-dimensional vectors which show the change of height along the surface of the sediment in the direction of wave travel, similar to the profile shown in Figure 4.1. A ripple histogram of each of these vectors is then calculated using the zero up-crossing method. The zero up-crossing method first determines the location where the sediment surface crosses the zero level with a positive slope. These locations are shown as the black dots in Figure 4.1. From this set of points the ripple surface is broken up into a series of sub-intervals. The maximum and minimum values of the data contained within the sub-intervals are used to determine the height of the ripple while the horizontal distance of the sub-interval is used to determine the individual ripple length. This provides arrays of ripple lengths and heights which can be displayed as histograms. The final histograms of the surface were formed by summing the individual histograms of each one-dimensional vector across the surface. Figure 4.2 shows the ripple histograms calculated from the measured array shown in Figure 3.6. The bold lines shown in Figure 4.2 represent the normal distribution fitted to the histograms. The normal distribution was fitted to the histograms shown in Figure 4.2 using a Levenberg-Marquardt nonlinear multiple regression technique.

Two interesting points can be seen in Figure 4.2. The first is that the ripple heights

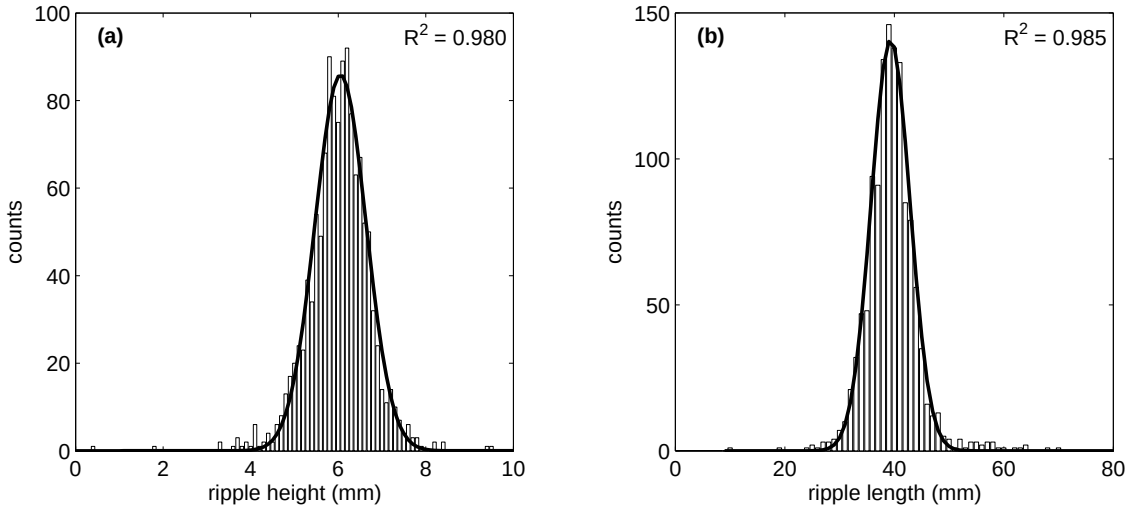

Figure 4.2 Example histograms of ripple parameters where (a) is the ripple height and (b) is the ripple length. The histograms were calculated from the rippled bed shown in Figure 3.6 ($n = 1253$). The Bold lines indicate the normal distribution fitted to the histograms while the R^2 values indicate the goodness of these fits.

and lengths follow an approximately normal distribution ($R^2 \geqslant 0.98$). As outlined above, *Wheatcroft* [1994] also found rippled beds followed a normal distribution. The main advantage of the histograms being normally distributed is that it allows the calculation of the mean (μ) and the standard deviation (σ) of the traditional ripple parameters without considering the higher moments of the distribution [*Wheatcroft*, 1994]. A second point is that the histograms show the substantial variation of ripple parameters on this ideally formed rippled bed. The mean ripple height of the bed shown in Figure 3.6 is 6.0 mm with a standard deviation of 0.7 mm which indicates that ripple heights vary over two standard deviations between 4.6 and 7.4 mm. The mean ripple length is 39.6 mm with a standard deviation of 5.3 mm which indicates that ripple lengths vary between 29.0 and 50.2 mm within two standard deviations from the mean. This level of variation in ripple parameters is considered significant for a rippled bed formed under near perfect conditions. This observed variation will be discussed and quantified for all the equilibrium rippled beds measured during this study in the next section by defining a coefficient of variation.

4.1.2 Variability of Ripple Parameters

Figure 4.2 shows that ripple parameters on the rippled bed shown in Figure 3.6 display a distribution of values. To quantify the width of this distribution a coefficient of variation has been defined. The coefficient of variation is an accepted measure of the relative dispersion and is given by:

$$C_v = \frac{100\sigma}{\mu} \tag{4.1}$$

where C_v is the coefficient of variation expressed as a percentage, μ is the mean of the record and σ is the standard deviation of the record. The ripple height coefficient of variation of the bed shown in Figure 3.6 is approximately 12%, while the coefficient of variation in the ripple length is approximately 13%. As outlined in the previous section it is considered that this level of variation in ripple parameters was significant for a rippled bed formed under near constant laboratory conditions.

Table 4.1 provides the ripple bed statistics for all 40 equilibrium tests undertaken for this aspect of the study. The test IDs shown in Table 4.1 are those presented in Table 3.3 (page 57). The values η_c and λ_c, shown in Table 4.1, are the characteristic ripple height and length. These are to be used further in Chapter 5 and are defined simply as the height and length that achieved the highest count within the histogram. For example, the characteristic ripple height and length for the rippled bed, shown in Figure 3.6 are 6.3 mm and 38 mm respectively. The mean and standard deviation of the ripple steepness, shown in Table 4.1, was calculated from the array of steepness formed by taking the ratio of the ripple heights over the lengths for each sub-interval determined from the zero up-crossing analysis (refer to Figure 4.1).

As can be seen in Table 4.1, the coefficient of variation ranges between approximately 8 and 25% for the ripple height, while for the ripple length ranges between 8 and 52% with most of the values lying between 10 and 20% for the ripple length. As outlined above, it was felt that this level of variation of ripple parameters generated under ideal laboratory conditions was significant. As an example, test E04_TA4 has a height range, within two standard deviations of the mean, between 4.3 and 7.9 mm and a length range of 29.3 and

Table 4.1 Variation of traditional ripple parameters relating to the tests shown in Table 3.3.

Equilibrium	Height (η)				Length (λ)				Steepness (η/λ)		
Test ID	μ	σ	C_v	η_c	μ	σ	C_v	λ_c	μ	σ	C_v
	mm	mm	%	mm	mm	mm	%	mm	–	–	%
E01_TA1	5.1	0.9	16.7	5.4	35.7	9.2	25.6	37.1	0.15	0.022	15.3
E02_TA1	7.4	1.0	13.7	7.8	46.2	5.9	12.9	44.1	0.16	0.014	8.7
E02_TA4	5.6	1.0	18.2	5.3	38.3	6.9	18.1	39.1	0.15	0.017	11.3
E03_TA1	5.2	0.8	16.3	5.1	36.2	6.2	17.0	36.6	0.14	0.019	12.9
E03_TA4	4.1	1.0	24.8	4.6	31.9	8.3	26.0	36.8	0.13	0.026	20.2
E04_TA1	7.2	0.8	10.7	7.6	45.6	3.8	8.3	45.7	0.16	0.010	6.5
E04_TA4	6.1	0.9	14.2	6.4	40.1	5.4	13.5	41.9	0.15	0.014	9.3
E05_TA1	5.2	0.6	11.8	5.1	34.4	4.0	11.6	33.4	0.15	0.014	9.5
E06_TA1	7.3	1.0	14.0	6.8	46.4	5.7	12.3	46.0	0.16	0.013	8.4
E07_TA1	5.4	0.8	15.4	5.5	37.6	5.6	15.0	36.5	0.14	0.018	12.3
E07_TA4	4.6	0.9	18.8	4.5	32.0	6.2	19.4	28.8	0.15	0.023	15.6
E08_TA1	7.9	0.9	10.9	7.7	50.1	5.4	10.9	48.0	0.16	0.010	6.4
E08_TA2	7.6	1.0	13.0	7.2	48.4	6.0	12.3	49.0	0.16	0.012	7.9
E08_TA3	7.0	0.8	12.1	6.7	45.3	4.7	10.5	45.1	0.15	0.012	7.7
E09_TA1	6.4	0.8	12.9	6.3	43.2	5.2	12.0	41.1	0.15	0.013	8.7
E09_TA2	5.5	0.8	13.6	5.8	40.2	5.5	13.7	38.6	0.14	0.014	10.2
E09_TA3	5.4	1.0	19.4	5.2	39.6	8.1	20.4	34.8	0.14	0.018	13.0
E09_TA4	5.0	1.2	25.0	5.0	39.8	20.8	52.2	35.6	0.13	0.025	19.1
E10_TA1	6.8	0.8	12.3	6.5	47.8	5.0	10.5	45.8	0.14	0.012	8.7
E10_TA2	6.6	0.9	13.5	7.0	46.5	6.6	14.2	46.9	0.14	0.015	10.6
E10_TA3	5.8	1.2	20.9	6.0	44.2	11.8	26.7	40.2	0.13	0.020	15.5
E10_TA4	5.3	1.2	22.4	4.8	42.4	14.1	33.3	40.9	0.13	0.024	18.5
E11_TA1	7.4	0.8	11.4	7.8	51.7	5.6	10.9	51.8	0.14	0.012	8.7
E11_TA2	6.6	0.7	10.6	6.6	48.4	5.2	10.8	46.4	0.14	0.012	8.5
E11_TA3	5.8	1.0	16.7	6.5	43.7	6.3	14.4	42.0	0.13	0.014	10.4
E11_TA4	5.2	1.0	18.8	5.5	40.9	5.7	14.0	40.3	0.13	0.016	12.3
E12_TA1	6.1	0.8	13.5	6.3	41.5	7.1	17.1	40.6	0.15	0.015	10.2
E12_TA2	5.3	0.9	17.6	5.6	37.2	6.5	17.4	38.3	0.14	0.018	12.8
E12_TA3	5.4	0.9	17.6	5.3	37.0	6.9	18.7	33.7	0.15	0.019	12.7
E12_TA4	5.3	0.9	16.0	5.5	36.4	6.0	16.6	35.2	0.15	0.016	11.2
E13_TA2	9.3	0.8	8.5	9.3	60.5	5.1	8.4	64.4	0.15	0.010	6.3
E14_TA2	7.0	0.8	11.4	7.4	50.1	5.0	9.9	51.3	0.14	0.013	9.6
E15_TA2	5.9	0.9	15.1	6.0	41.8	6.3	15.0	39.8	0.14	0.018	12.4
E16_TA2	9.5	0.8	8.8	9.6	64.1	6.3	9.8	67.7	0.15	0.012	8.1
E17_TA2	5.7	0.6	11.1	5.8	37.9	4.7	12.4	38.0	0.15	0.013	8.7
E18_TA2	8.8	0.8	8.9	8.9	56.3	4.6	8.1	56.3	0.16	0.008	5.2
E19_TA2	5.7	1.0	18.0	5.3	41.5	9.6	23.2	42.3	0.14	0.020	14.0
E20_TA2	9.3	0.8	8.1	9.4	60.3	5.8	9.6	55.2	0.15	0.010	6.4
E21_TA2	5.7	0.7	11.8	5.6	38.6	5.2	13.4	36.7	0.15	0.014	9.2
E22_TA2	6.9	0.9	12.7	6.9	48.8	7.6	15.5	47.1	0.14	0.016	10.8

Table 4.2 Irregular flow parameters used by *Williams et al.* [2004], Tables 1 and 2.

Test ID	Water	Sand	Wave Parameters		Dimensionless Variables					
	Depth	D_{50}	f_p	H_s	$\Re_d$	$\Re$	ϑ	ψ	d_o/D_{50}	χ
	m	μm	Hz	m	–	–	–	–	–	$\times 10^{-7}$
D-1M01	4.5	329	0.20	0.53	97.2	69430	0.118	16.4	1428.9	8.134
D-1M02	4.5	329	0.20	0.83	152.2	170270	0.251	40.2	2237.7	8.134
D-1M03	4.5	329	0.20	1.07	198.7	295960	0.393	68.5	2979.5	7.818
D-1M04	4.5	329	0.20	1.26	233.9	410410	0.520	95.0	3508.6	7.818
D-1M05	4.5	329	0.20	1.13	205.8	308340	0.421	73.5	2996.2	8.299
D-1F01	4.5	162	0.20	0.55	49.4	73390	0.204	35.5	2971.6	4.070
D-1F02	4.5	162	0.21	0.82	71.3	146250	0.387	74.0	4100.8	4.456
D-1F03	4.5	162	0.19	1.11	103.4	340760	0.718	155.3	6593.9	3.619
D-1F04	4.5	162	0.22	1.47	122.2	405620	1.002	217.0	6639.3	4.989
D-1F05	4.5	162	0.19	1.14	105.8	355040	0.749	162.7	6711.4	3.661

50.9 mm which is approximately a 50% difference in the parameters determined from this bed. Another interesting point, which can be observed in Table 4.1 is that rippled beds formed under higher mobility conditions generally have smaller coefficients of variation.

As outlined above, there has been very little research undertaken to quantify the variation of rippled beds. Due to the difficulty of measuring ripple parameters, previous studies have mainly concentrated on reporting single values for the characteristic ripple parameters (height and length). However, a recent study by *Williams et al.* [2004] presented characteristic ripple parameters as well as the standard deviation of the ripple parameters formed under both regular and irregular waves. Table 4.2 presents the irregular flow conditions used by *Williams et al.* [2004] to generate rippled beds. The dimensionless variables presented in Table 4.2 were calculated from data originally presented in *Williams et al.* [2004] and are included so that comparisons can be made with the experimental data presented in Table 3.3. The method used to calculate the dimensionless variables was outlined in Section 3.2. Note that *Williams et al.* [2004] also measured rippled beds formed under the action of large scale regular waves, however, these results will not be presented or used in the current study as the focus is on rippled beds formed under irregular waves.

As shown in Table 4.2, the scale of wave conditions *Williams et al.* [2004] was able to generate are much larger than could be achieved in the current study. This enables this

Table 4.3 Ripple parameters measured by *Williams et al.* [2004], Tables 1 and 2.

Test ID	Height (η)			Length (λ)		
	μ mm	σ mm	C_v %	μ mm	σ mm	C_v %
D-1M01	30.	1.	3.3	290.	1.	0.3
D-1M02	40.	1.	2.5	330.	2.	0.6
D-1M03	40.	2.	5.0	420.	17.	4.0
D-1M04	50.	3.	6.0	530.	25.	4.7
D-1M05	40.	8.	20.0	510.	91.	17.8
D-1F01	10.	1.	10.0	290.	34.	11.7
D-1F02	10.	2.	20.0	470.	52.	11.1
D-1F03	20.	5.	25.0	1040.	198.	19.0
D-1F04	20.	4.	20.0	620.	130.	21.0
D-1F05	20.	3.	15.0	570.	61.	10.7

area of the research to be extended into these larger scale conditions. Table 4.3 presents the ripple parameters measured by *Williams et al.* [2004]. The test ID shown in Table 4.3 are those presented in Table 4.2. The ripple data presented in Table 4.3 were measured by acoustic means, hence, the error of the measurements is likely to be larger than those measured during the current study. This is especially the case for the ripple heights which, in general, are poorly resolved by acoustic systems [*Betteridge et al.*, 2003].

The coefficient of variation ranges between approximately 3 and 25% for the ripple heights presented in Table 4.3, while for the ripple length the coefficient ranges between 0.3 and 21%. Interestingly, as the bottom mobility conditions are increased there is a general increase in the coefficient of variation in Table 4.3. This trend was opposite to that in the data set measured during the current research (refer to Table 4.1), which showed that as the mobility conditions were increased there was a decrease in the coefficient of variation.

There has been little work undertaken to try and relate the observed variation in ripple parameters to flow or sediment conditions. If this could be achieved it would enable the variability of rippled beds formed under different mobility conditions to be determined and allow an estimate of the error associated with ripple predictions to be quantified. Figure 4.3 shows the coefficient of variation (C_v) for the ripple heights listed in Tables 4.1

and 4.3 plotted against the six non-dimensional numbers shown in Tables 3.3 and 4.3.

The opposing trends in the two sets of data can be seen very clearly in Figure 4.3. The data set measured as part of the current study shows a downward trend as the mobility conditions are increased while the data set measured by *Williams et al.* [2004] shows an upward trend becoming more variable at higher mobility conditions. The maximum coefficient of variation for the ripple height is in the order of 30% for both data sets while the lowest variation is around 3% calculated from the *Williams et al.* data set. The overall trend is for the ripple height variation to start at a high value for low mobility conditions, drop to a minimum at medium mobility conditions, then increase back to a high value at higher mobility conditions.

Figure 4.4 shows the coefficient of variation (C_v) for the ripple lengths listed in Tables 4.1 and 4.3 plotted against the six non-dimensional numbers shown in Tables 3.3 and 4.3.

Once again opposing trends in the two data sets, shown in Figure 4.4, are evident with the value of the ripple length variation decreasing as mobility conditions are increased for the current study's data set and increasing for the set measured by *Williams et al.* [2004]. The magnitude of the variation is higher in Figure 4.4 for the ripple lengths than was the case for the ripple heights (refer to Figure 4.3). The maximum coefficient of variation for the ripple length is in the order of 40 to 50% for both data sets. However, the same overall trend is evident with the variation starting at a high value, dropping to a minimum, then increasing back to a high value as the mobility conditions are increased.

The smaller scale measurements generated during the current study are very low and are borderline in terms of ripple development, while the larger scale measurements of *Williams et al.* [2004] cross into the higher suborbital range of ripple development (refer to Section 2.1.1). Hence, an explanation for the change in ripple variability behaviour may be due to the relative magnitudes of the flow conditions. Initially the increase in the magnitude of the non-dimensional numbers represents a general increase in the movement of sediment grains within the bottom boundary layer, which enables ripples to form more uniformly across the bed. This trend continues until the ripple regime changes from

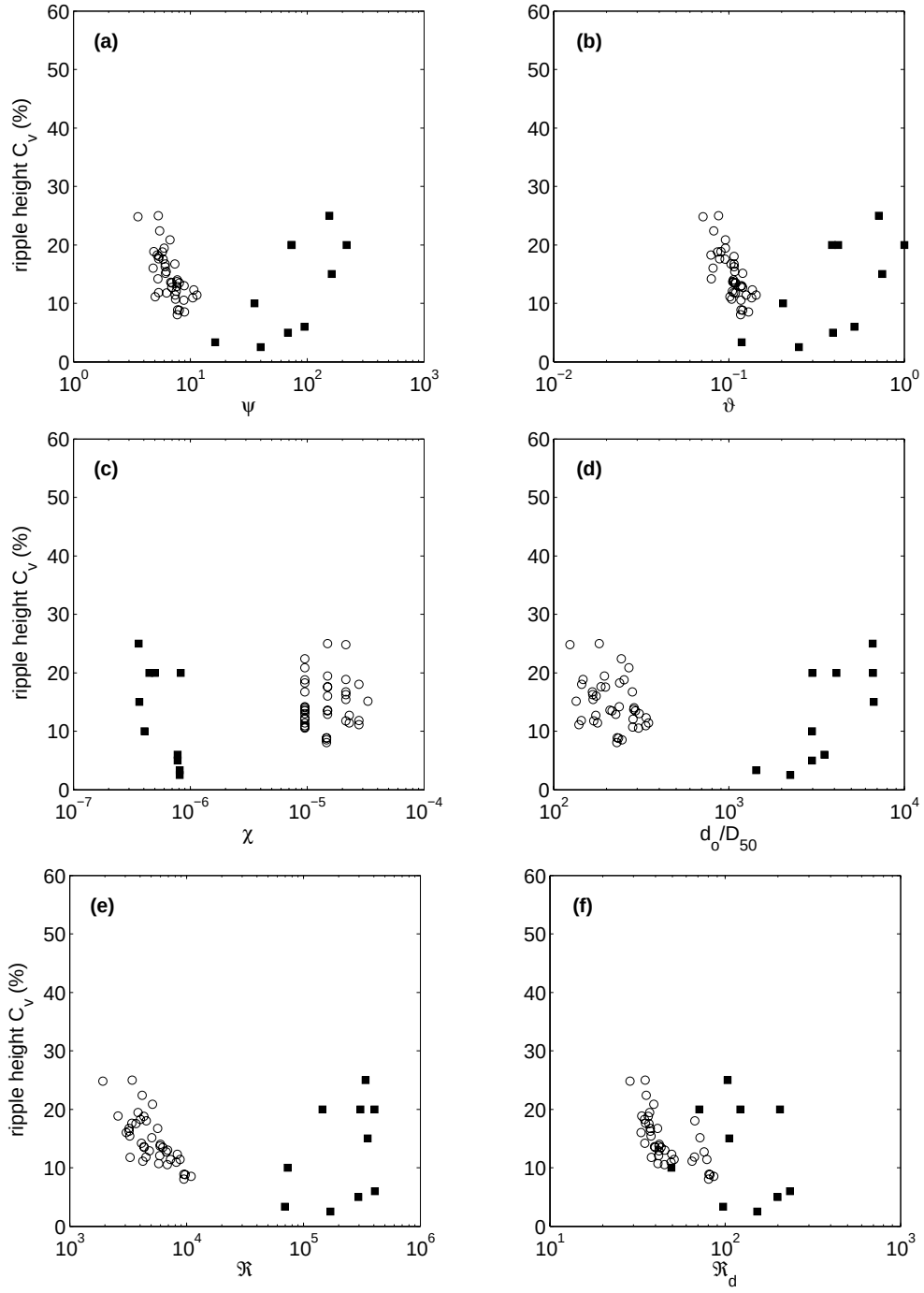

Figure 4.3 The variation of ripple height C_v plotted against: (a) the mobility number; (b) the Shields number; (c) the period parameter; (d) the normalised orbital excursion diameter; (e) the flow Reynolds number and (f) the sediment Reynolds number. The different symbols shapes denote the two data sets used: circles (○) represent data measured as part of the current study while filled squares (■) represents ripples measured by *Williams et al.* [2004].

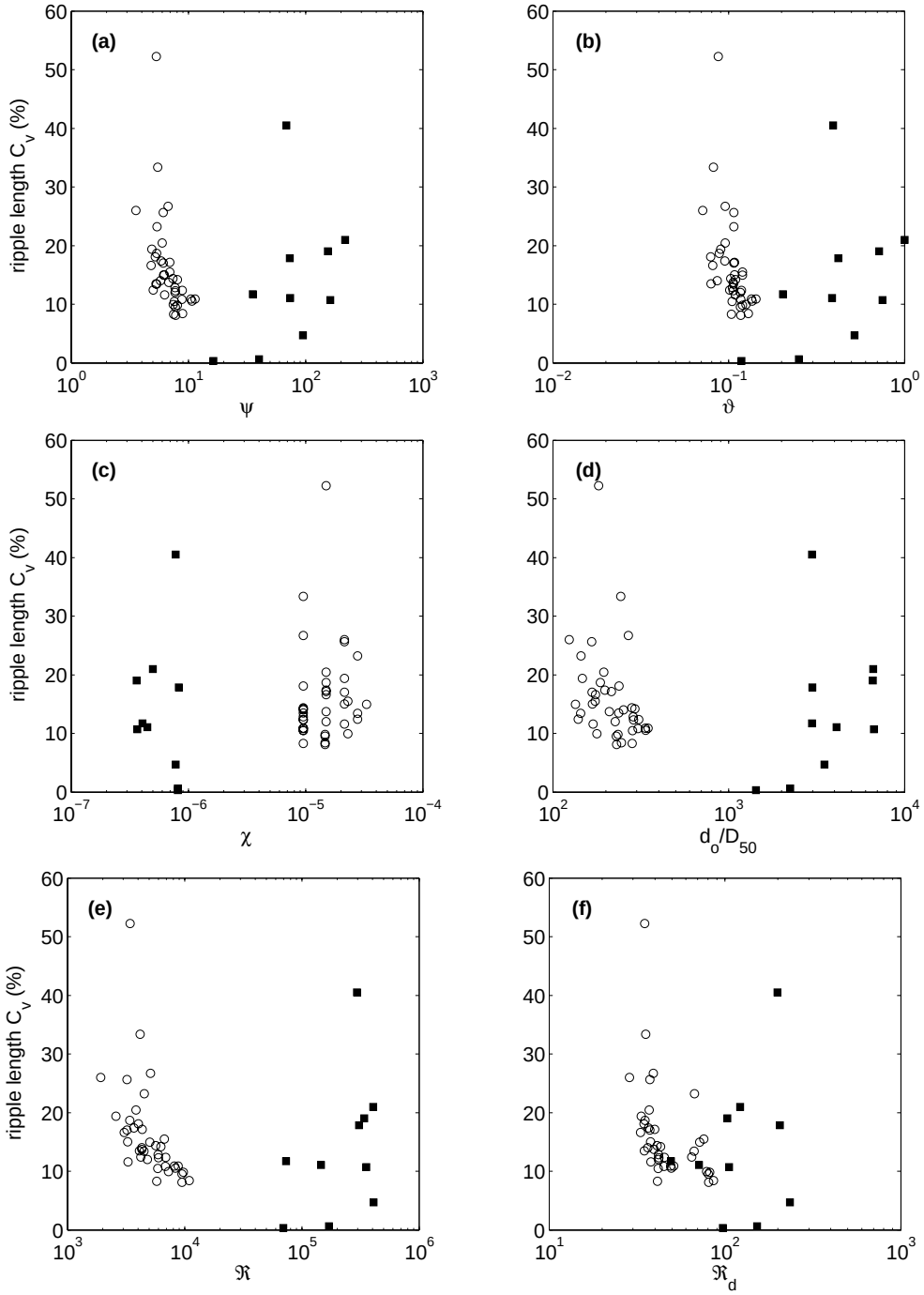

Figure 4.4 The variation of ripple length C_v plotted against: (a) the mobility number; (b) the Shields number; (c) the period parameter; (d) the normalised orbital excursion diameter; (e) the flow Reynolds number and (f) the sediment Reynolds number. The different symbols shapes denote the two data sets used: circles (○) represent data measured as part of the current study while filled squares (■) represents ripples measured by *Williams et al.* [2004].

orbital to suborbital and ripples start to be eroded by the higher flow conditions. Due to the random flow fluctuations within the bottom boundary layer under irregular waves some individual ripple forms will be eroded and others not, hence there is an increase in the overall variability of the ripple beds.

To the author's knowledge this type of analysis on the variability of ripple parameters has not been undertaken previously. It highlights a possible bias that ripple prediction methods have in predicting ripples formed under medium mobility conditions. At higher and lower mobility conditions ripples will be inherently variable with a distribution of ripple parameters existing on a given bed. The next section will present the development of a spectral method to account for this observed variability.

4.2 SPECTRAL PARAMETERISATION

An efficient method to account for the observed spatial variation of ripple parameters is to undertake a Fourier analysis of the rippled surface. The resulting spectral density function allows the surface to be described concisely in terms of the distribution of energy on the rippled surface as a function of spatial frequency. The development of a spectral density function from the sediment surface is a direct analogy to undertaking the same analysis on the time series of the water surface. However, there are a number of important differences. The first is that the sediment surface is measured as a spatial series while the water surface is measured as a time series. Mathematically this is not a difficult problem to overcome, but it makes relating the two spectra problematic. The second is that in the absence of waves the water surface is effectively flat, this is not generally the case for a sediment surface. Hence a substantial part of this section will be dedicated to the discussion of the spectral filtering that was employed to remove the low spatial frequency trends due to an uneven surface, and the high spatial frequency noise due to the high frequency measurement noise. The last major difference is that over the temporal scale of water waves the water can be assumed to be homogenous, this is not the case for sediment beds. As shown in Figure 3.3 (page 47), sediment diameters are generally distributed across a range of values. This study did not investigate the effect that the variability of sediment

parameters has on the variability of rippled beds, but highlights it as a future area of research.

Throughout this section the example rippled bed, Figure 3.6 (page 56), will be used to highlight the calculation method. The method used to calculate a one-dimensional spectrum from a two-dimensional surface will be introduced. Unfortunately only long crested, one-dimensional rippled beds were able to be generated by this study, hence, only one-dimensional spectra were calculated from the rippled beds. However, the method could easily be extended to two-dimensions to take into account variability in ripple directions and patterns. *Lyons et al.* [2002], following on from work undertaken by *Pouliquen et al.* [2000], discussed the issues in calculating a two-dimensional ripple spectra of the seafloor. Once the calculation method has been discussed, the filtering of the rippled surface will be introduced and discussed in terms of its effect on the spectrum. After which the ripple spectra for all 40 equilibrium tests outlined in Table 3.3 (page 57) will be compared with trends between experiments discussed.

4.2.1 Bottom Elevation Spectrum

Figure 4.5 presents the one dimensional spectral density function estimated from the rippled sediment surface shown in Figure 3.6. As indicated in Section 3.2.2, the data array shown in Figure 3.6 was scanned using the ripple measurement system and consisted of 51 parallel one-dimensional long sections scanned along the flume in the direction of wave travel. Each one-dimensional scan was composed of 512 data points.

The spectral estimate of the bed was determined by first calculating the individual variance spectra of each of the 51 one-dimensional vectors scanned in the primary direction. The 51 spectra were averaged to give a spectral estimate of the rippled surface as a whole. This was done to smooth the spectrum and to increase the accuracy of the spectral estimate, while keeping a high spectral resolution. The individual spectra were calculated with a Hamming window of 512 data points via the power-spectral-density PSD routine within MATLAB's Signal Processing Toolbox (Mathworks, Signal Processing Toolbox, available at www.mathworks.com, 2002). This gave 51 spectral estimates

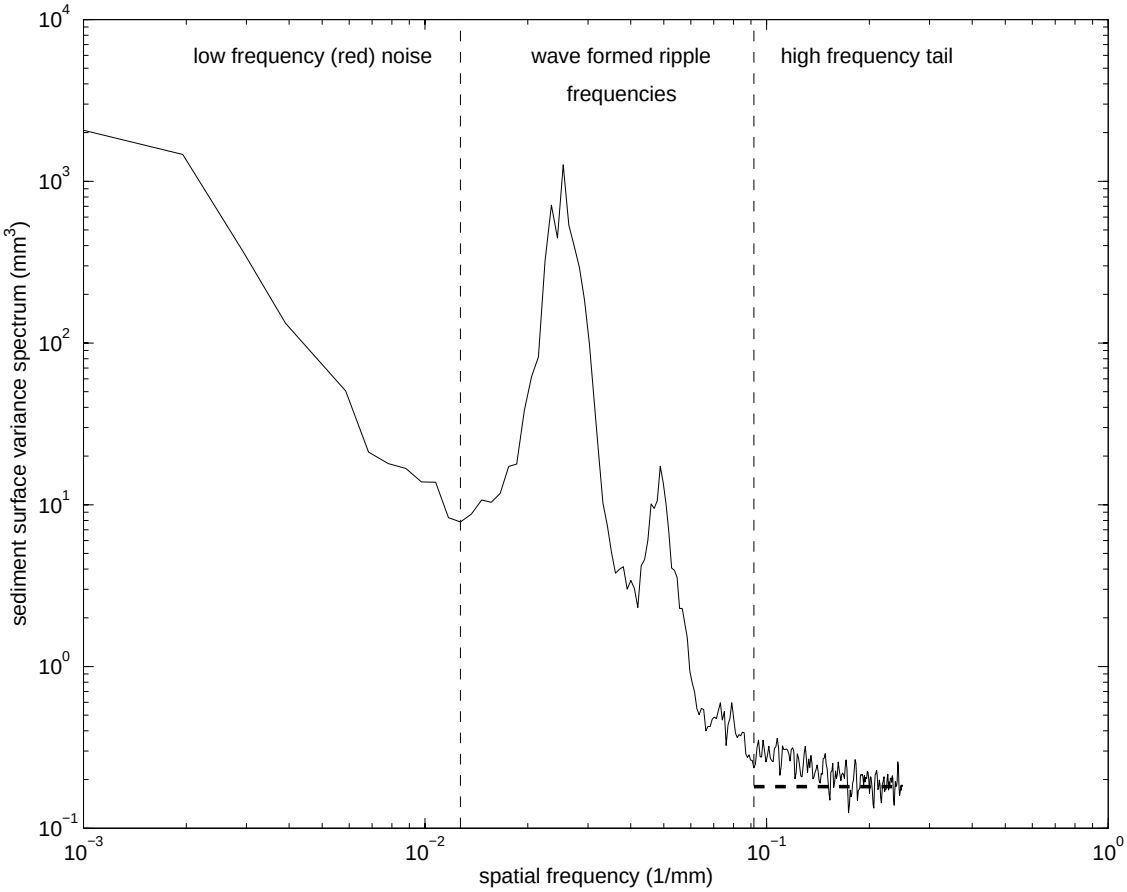

Figure 4.5 The one-dimensional spectrum calculated from the example ripple surface shown in Figure 3.6. Ripple frequencies are enclosed by the two vertical dotted lines. The bed was formed under random surface waves with a peak period of 0.1 Hz and a significant wave height of 95 mm.

of the bed each with 2 degrees of freedom. The PSD function utilises Welch's averaged, modified periodogram method and outputs a power spectrum (mm^2) which was scaled by 2 times the sample interval (mm) to give a variance spectrum (mm^3) (refer to Section 3.3.1 for more details). The resulting spectrum provided an overall spectral estimate of the 500 mm $\times$ 1022 mm (0.51 m^2) sediment surface scanned.

As shown by the vertical dotted lines in Figure 4.5, the spectrum of the sediment surface can be broken up into a number of distinct regions. The exact boundaries of these regions will be different for a spectrum calculated from rippled beds with different sized ripples, however, all three regions generally exist for a given ripple spectrum. Each of

these regions will be briefly discussed with specific reference to the sediment spectrum shown in Figure 4.5.

The first region is the low frequency region with spatial frequencies (f_s) less than approximately 0.01 mm^{-1} (100 mm) down to the sample length (1024 mm). Unlike typical water wave spectra the spectral density function of the sediment surface shown displays a large low frequency component. Almost all topographical data show the presence of a low frequency trend due to wavelengths within the data that are longer than the sample length. There is generally a finite limit to the rate of change of the process, causing the lower frequency components to also be of the greatest amplitude [*Fox and Hayes*, 1985]. This type of spectrum was termed by *Fox and Hayes* [1985] as a *"red noise"* spectrum, which is an analogy to the red low frequency end of the visible light spectrum. The presence of low frequency high energy *"red noise"* introduces a major problem in using the spectrum to analyse wave formed ripples. As shown in Figure 4.5, the spectral energy of this noise is larger than the peak energy level of the ripple bands. This will cause the spectral parameters estimated from the spectrum to be skewed unrealistically towards the lower spatial frequencies. This requires that the low frequency noise be removed from the spectrum prior to any analysis being undertaken.

The middle region ranges between spatial frequencies of approximately 0.01 mm^{-1} (100 mm) to 0.09 mm^{-1} (11 mm) and, from preliminary tests and observations undertaken, contains the spectral energy due to the wave formed sediment ripples present on the sediment surface. The peak spatial frequency of this rippled bed is approximately 0.025 mm^{-1} (40 mm). As shown in Figure 4.5, there is a large second harmonic component at approximately 0.05 mm^{-1} (20 mm) and a smaller third harmonic component at approximately 0.075 mm^{-1} (13 mm) contributing to the ripple's spectral energy on this sediment bed. On examining the raw data the ripples approach the shape of water waves in shallow water with broader troughs and peaked crests. This distinctive shape of ripple forms can be seen in Figure 4.1. To describe this type of surface requires a larger number of Fourier harmonics than would otherwise be needed if the ripples had a pure sinusoidal shape. Hence, the extra harmonics present in the spectrum represent the Fourier method

trying to fit the shape of the ripple forms.

The last region is the high frequency tail end of the spectrum which ranges from a spatial frequency of approximately 0.09 mm^{-1} (11 mm) to the Nyquist frequency of 0.25 mm^{-1} (4 mm). In Figure 4.5, the move to higher spatial frequencies brings increasing random noise into the spectrum. Once again in analogy to the light spectrum, *Fox and Hayes* [1985] termed this type of noise *"white noise"*. White noise is characterised by a random fluctuation with equal contribution to all spatial frequencies and, as such, white noise is recognised within the spectrum as a chaotic horizontal line. *Fox and Hayes* indicated that the highest frequency that is able to be resolved is the spatial frequency where the horizontal white noise line intersects with the spectrum of the signal. In the case of the spectrum shown in Figure 4.5 this occurs at a spatial frequency in the order of the Nyquist frequency. Using Rayleigh's or Parseval's theorems the noise level of the signal can be estimated from the magnitude of the white noise. This theorem states that the integral of the power spectrum equals the integral of the squared modulus of the function [*Fox and Hayes*, 1985], given as:

$$\int_{-\infty}^{\infty} |g(x)|^2 dx = \int_{-\infty}^{\infty} |G(f_s)|^2 df_s \tag{4.2}$$

where $g(x)$ is the sediment surface elevation and $G(f_s)$ is the Fourier transform of $g(x)$. Equation 4.2 indicates that the energy within the spatial domain is equal to the energy within the spatial frequency (spectral) domain. This means that the amplitude of the noise level in the amplitude spectrum can be related to the noise level in the spatial series [*Fox and Hayes*, 1985]. In the case of the spectral plot shown in Figure 4.5 the amplitude of the high frequency white noise was in the order of 0.2 mm. From these two observations it was concluded that the laser measurement system had a vertical resolution in the order of 0.2 mm and a horizontal resolution less than 4 mm (Nyquist frequency). This accuracy was considered acceptable to measure the sediment bed forms examined in this thesis, which were consistently greater than 30 mm in length and 4 mm in height. The presence of the white noise at higher frequencies does not dramatically affect the use or accuracy of the ripple spectrum because the spectral energy levels are very much smaller than the

energy of the ripples. However, the higher spatial frequencies do not contribute to the analysis of the ripples and ideally should also be removed.

4.2.2 Spectral Filtering

As indicated above, the presence of red noise in the spectrum makes using the bottom spectrum difficult as the red noise frequencies have higher energy levels than the ripple frequencies. Hence, the red noise needs to be removed prior to the ripple spectrum being analysed. The presence of the white noise at higher frequencies does not effect the use or accuracy of the ripple spectrum due to the spectral energy levels being very much smaller than the energy of the ripples. However, the higher spatial frequencies do not contribute to the analysis of the ripples and ideally should also be removed from the spectrum. The removal of both types of noise was achieved through the use of a Fourier band pass filter. A MATLAB function file containing the Fourier band pass filter was made available to this study by Prof. Mark Donelan of the University of Miami, USA.

The band pass filter was applied to the measured raw data array (refer to Figure 3.6). Each row of the raw data array was transformed to frequency space via a Fast Fourier Transform (FFT) routine. Spectral energy components with spatial frequencies less than f_{s1} = 0.01 mm^{-1} (100 mm) and greater than f_{s2} = 0.1 mm^{-1} (10 mm) were removed. The values for the banding frequencies were somewhat arbitrary and were chosen to encompass all the ripple frequencies encountered in the experimental tests. Tighter limits could have been set for individual rippled beds, however, there was little benefit from doing this as the ripple energy levels were much higher than the energy levels in the vicinity of the banding frequencies. The filtered data were then transformed back to the spatial domain via an inverse FFT routine (IFFT). Figure 4.6 shows the effect of removing the noise from the measured data array shown in Figure 3.6.

As shown in Figure 4.6, filtering the data array removes the longer trends that were present on the surface shown in Figure 3.6. Filtering has not affected the ripple's spacing, height or shape. From the filtered data array, a spectral estimate for the surface was calculated as described in Section 4.2.1. Figure 4.7 presents the variance spectrum of the

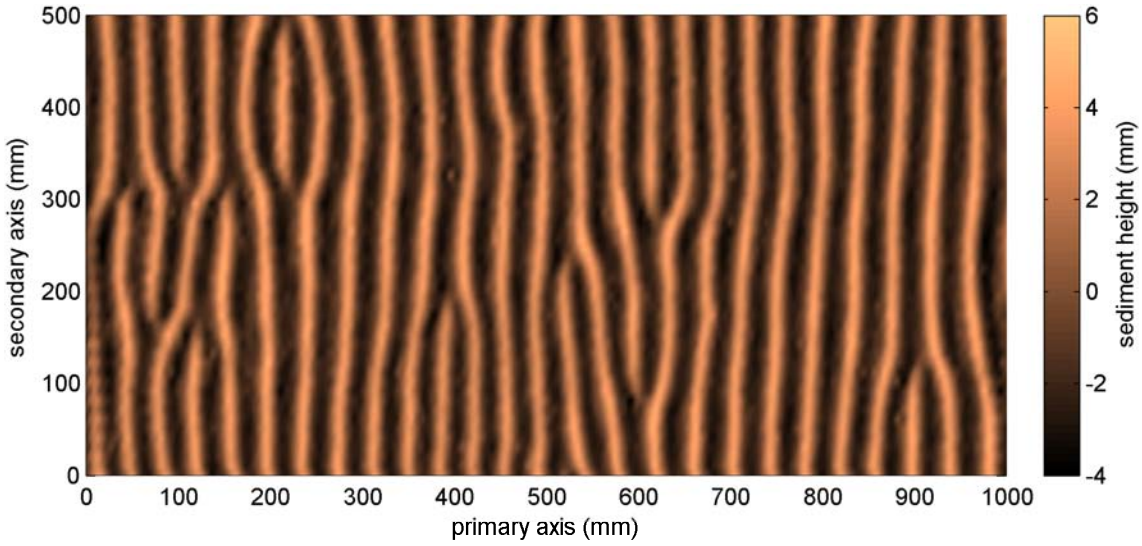

Figure 4.6 The filtered form of the rippled bed shown in Figure 3.6.

filtered sediment surface shown in Figure 4.6. Figure 4.7 shows that the spectral energy outside the ripple range ($f_{s1} < f_s < f_{s2}$) has been removed completely while the spectral energy attributed to the wave formed ripples has not been changed.

4.2.3 The Ripple Spectrum

The filtered form of the bottom elevation spectrum shown in Figure 4.7 has been termed the ripple spectrum. A one-dimensional ripple spectrum was calculated for each of the 40 experimental tests listed in Table 3.3. Figure 4.8 presents the 40 spectra grouped by the surface wave frequency that was used to form the rippled bed. The two line types shown indicate the two types of sediment (type 1 and type 2) used as part of the experimental tests (refer to Table 3.1, page 46).

It should be noted that these spectra were calculated with a window of 128 data points to further increase the accuracy of the spectral curves from the spectrum shown in Figures 4.5 and 4.7. Reducing the length of the data window has increased the accuracy of the ripple spectra at the expense of the spectral resolution.

The tests shown in Figure 4.8 were not only conducted with different frequencies and sediment diameters, but also with different wave heights and depths. The aim of the

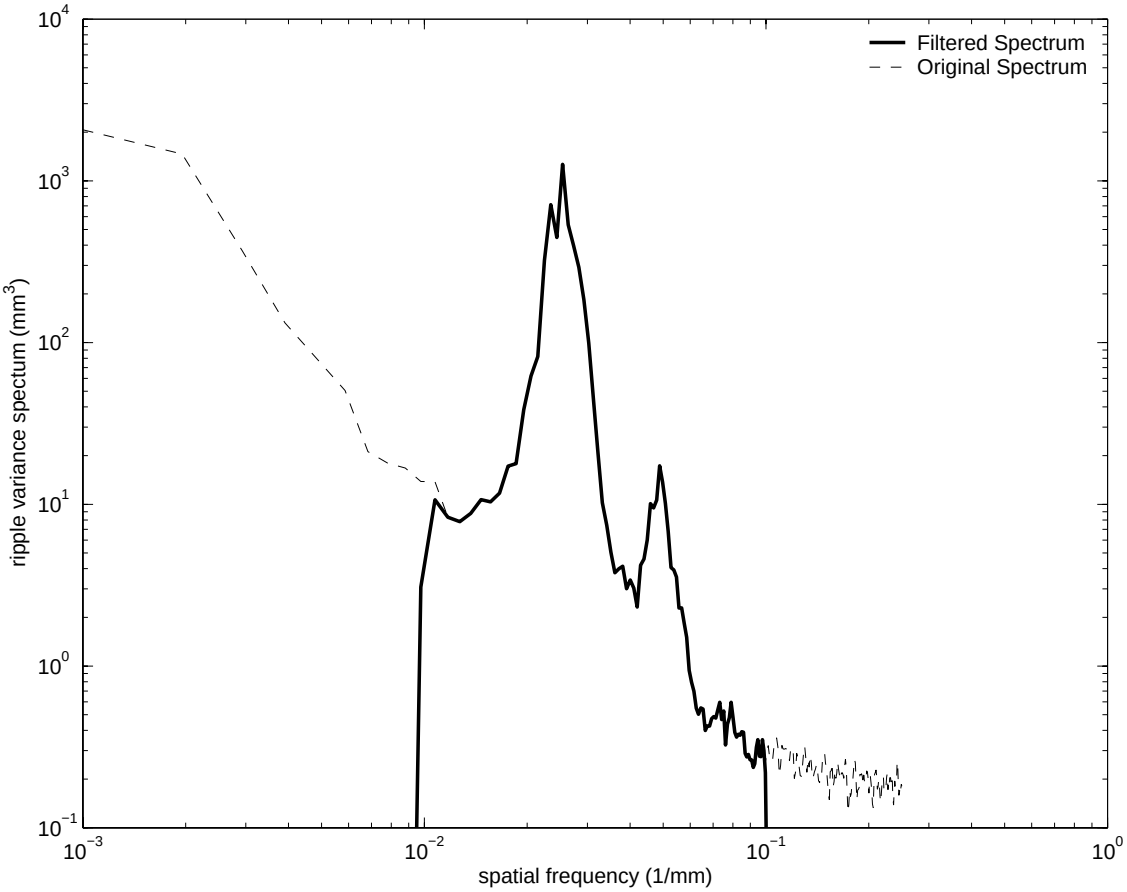

Figure 4.7 The one-dimensional spectrum calculated from the filtered ripple surface shown in Figure 4.6.

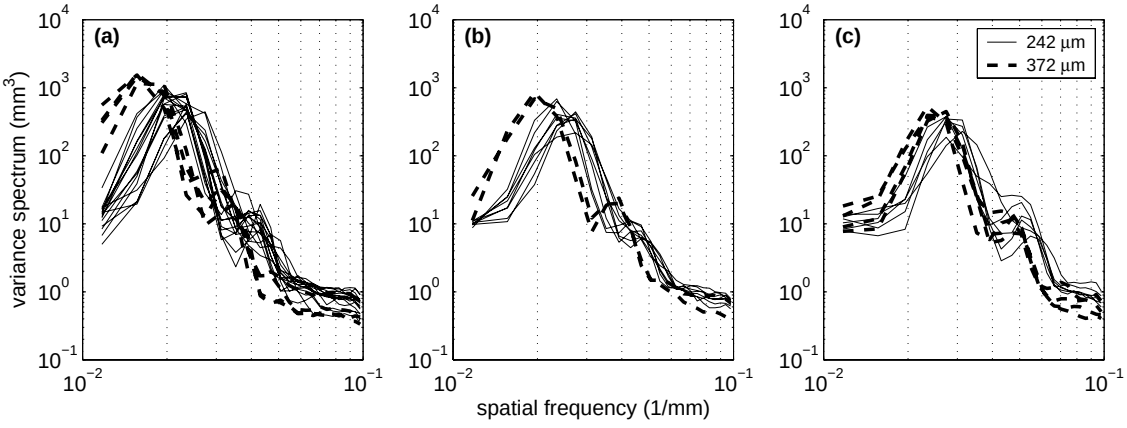

Figure 4.8 The ripple spectra grouped by surface wave frequency: (a) 0.8; (b) 1.0, and (c) 1.2 *Hz* tests. Different line types indicate the different types of sediment used in the tests.

experiments was to generate bottom mobility conditions across the largest range possible using the wave generation equipment that was available to the study. This makes direct comparison of the spectra in this form problematic, however, a number of trends can be inferred from the data shown in Figure 4.8. The first is that as the peak frequency of the surface waves is increased from 0.8 to 1.2 Hz there is a general increase in the peak spatial frequency and a decrease in the spectral energy levels of the ripple spectra for a given sediment size. This indicates that as the surface wave frequency increases the ripples on the bottom surface decrease in height and length. The second is that increasing the sediment diameter from 242 to 372 μm causes a general decrease in the peak spatial frequency and an increase in the spectral energy of the ripple spectra. This indicates that coarser sediments beds develop rippled beds with higher and longer ripple forms. These two observations are consistent with generally accepted behaviour of wave-formed ripples [*Nielsen*, 1992].

Another interesting point is the similarity in spectral shapes shown in Figure 4.8. A different spectral shape indicates differences in the variability of the rippled bed. For example a broader spectrum would indicate a higher level of variability than a narrow spectrum. The next section will introduce two spectral shape parameters, a spectral width factor and a spectral peakedness parameter. These parameters will be tested to see if they provide any insight into the dependence of the shape of the ripple spectrum against the flow and sediment conditions used in the experimental tests.

4.2.4 Spectral Parameters

One of the benefits of using a spectral parameterisation for describing rippled beds is that previous work developed to describe the surface wave spectrum can be applied to the ripple spectrum. This section will introduce and outline two of these descriptive parameters derived from the spectrum, a spectral width factor and peakedness parameter. A number of authors have used and discussed these parameters with relation to the water wave spectra [e.g., *Goda*, 1978; *Longuet-Higgins*, 1983].

The spectral width factor (v) is a measure of the spectral bandwidth [*Goda*, 1978] and

is given as:

$$v = \sqrt{\frac{m_0 m_2}{m_1^2} - 1} \tag{4.3}$$

where m_n is the nth moment of the spectral density, calculated as:

$$m_n = \int_0^\infty f^n S(f)\, df \tag{4.4}$$

where f is either the frequency (Hz) or the spatial frequency (m^{-1}) and S is the variance spectrum with units of either (m^2/Hz) for a water wave spectrum or (m^3) for the ripple spectrum. For a full derivation of the spectral width factor see *Longuet-Higgins* [1983].

The spectral width factor was calculated for each of the ripple spectra shown in Figure 4.8 and plotted against six of the more widely used non-dimensional numbers, relevant to ripple formation: the mobility number; the Shields number; the period parameter; the normalised orbital excursion diameter; the flow Reynolds number and the sediment Reynolds number. This was done so that a possible functional dependence for the spectral width factor could be investigated. Figure 4.9 shows the spectral width factor plotted against the above six non-dimensional numbers. The different symbol shapes and fills denote the different frequency conditions and sediment types used in the experiments.

In Figure 4.9, the spectral width factor ranges between 0.2 and 0.35 for the ripple spectra shown in Figure 4.8. There is not a pronounced trend between the spectral width factor and the non-dimensional parameters in Figure 4.9 with all values of the non-dimensional numbers having the same spectral width. This is also the case for the surface wave frequency and the 50 percentile grain size diameter shown as the different shaped and filled symbols. Across all experimental tests there is no defined trend in the spectral width factor. This is somewhat surprising as there was a substantial variation in the ripple height and length shown in Figures 4.3 and 4.4. Hence, it was concluded that there is a limited amount of information to be gained from using the spectral width factor to classify the ripple spectra measured in this study.

The spectral peakedness parameter [*Goda*, 1978] is calculated from the spectrum by:

$$Q = \frac{2}{m_0^2} \int_0^\infty f\ S(f)^2\, df \tag{4.5}$$

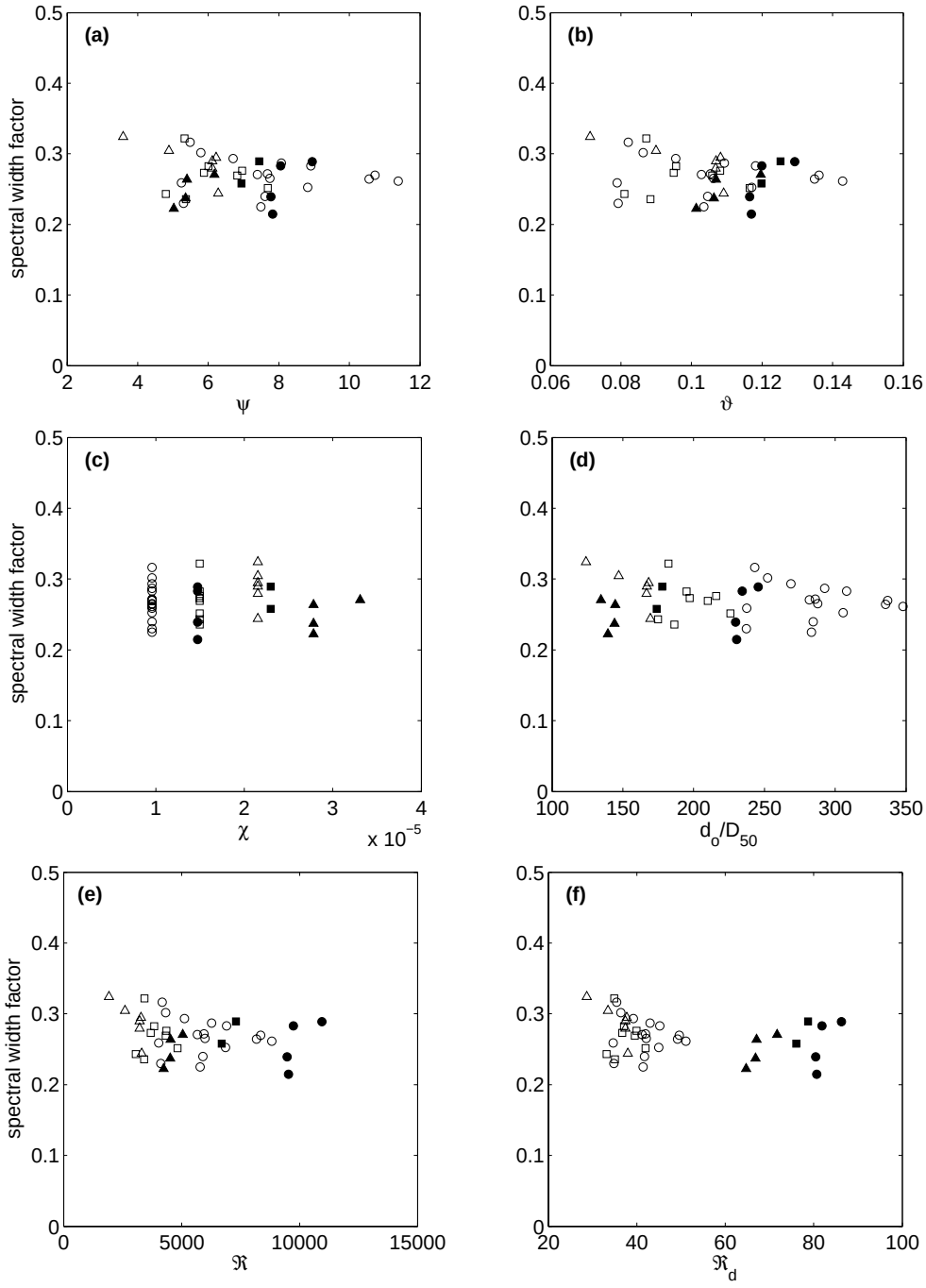

Figure 4.9 The spectral width factor plotted against: (a) the mobility number; (b) the Shields number; (c) the period parameter; (d) the normalised orbital excursion diameter; (e) the flow Reynolds number and (f) the sediment Reynolds number. The different symbols shapes denote the different frequency conditions used: ○ - 0.8 Hz; □ - 1.0 Hz; △ - 1.2 Hz, while the fill indicates the sediment type: open - 242 μm; filled - 372 μm

where Q is the spectral peakedness parameter and gives an estimate of the spectral peak. As with the spectral width factor the spectral peakedness parameter for each of the spectra, shown in Figure 4.8, was plotted against six of the more widely used non-dimensional numbers. Figure 4.10 presents the spectral peakedness parameter. Once again the different symbols shapes and fills denote the different frequency conditions and sediment types used in the experimental tests.

As with the spectral width factor (refer to Figure 4.9), the spectral peakedness factor does not show any real dependence on the surface wave frequency or sediment type used in the tests, as shown by the scatter of different symbols across the plot. However, there does seem to be a weak positive correlation between the peakedness parameter and all of the non-dimensional numbers except for the period parameter. This is consistent with the trend seen in Figures 4.3 and 4.4, which illustrated that as the mobility conditions were increased there was a general decrease in the variability of the ripple parameters on the sediment beds for the data measured during this study. As the rippled beds become less variable the spectra would become more narrow banded and hence the peakedness factor would increase in magnitude. It was concluded that the spectral peakedness factor may provide some information as to the shape of the ripple spectra given a set of experimental conditions. However, the trends were weak for the ripple spectra calculated as part of this study.

Interestingly, the ripple spectra were formed under a variety of conditions, but show no defined trend in the shapes of ripple spectra as shown in Figures 4.9 and 4.10. This is surprising, as the study was expecting to see some change in the spectral shapes due to observed variability of the rippled beds (refer to Section 4.1.2).

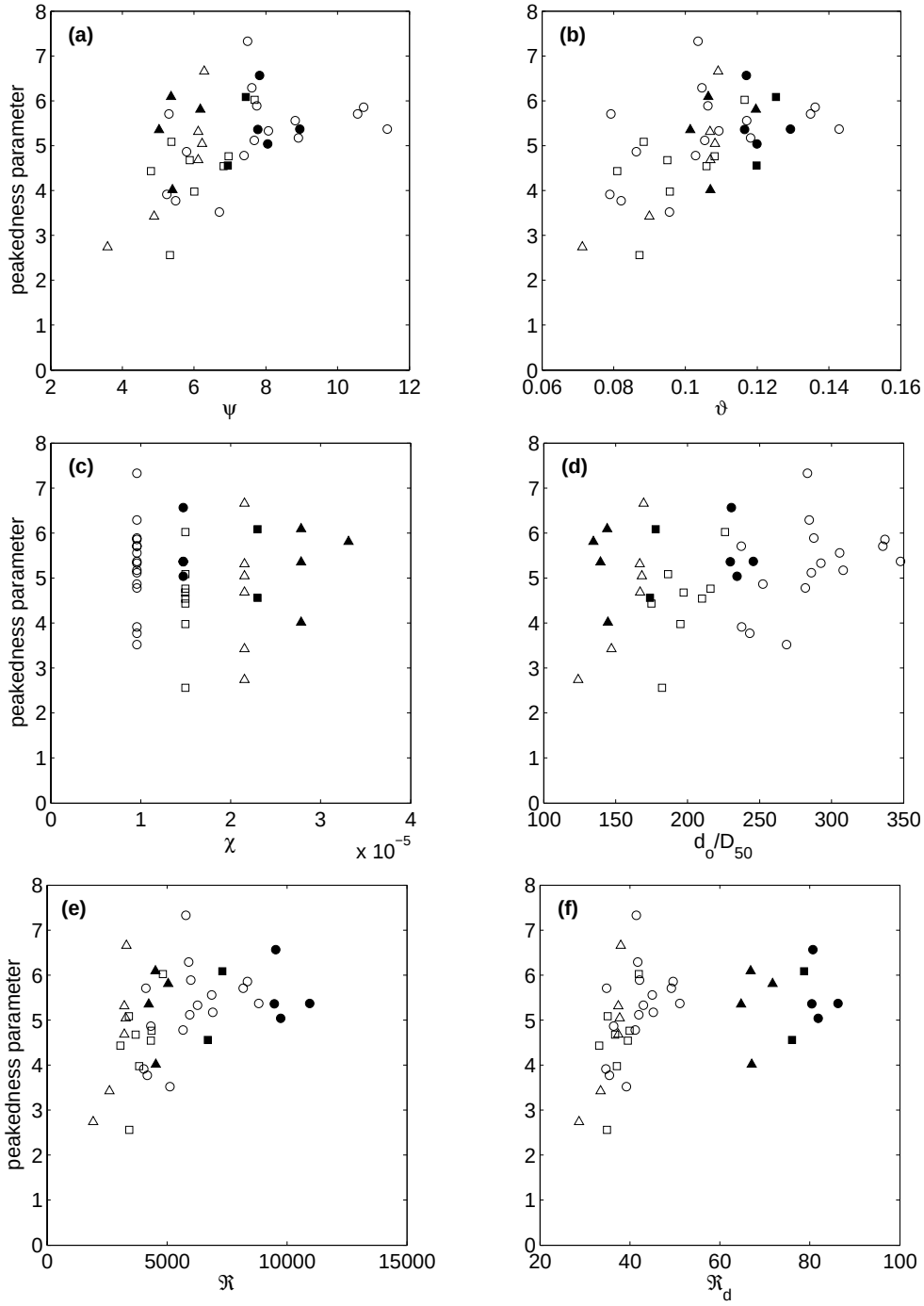

Figure 4.10 The peakedness parameter plotted against: (a) the mobility number; (b) the Shields number; (c) the period parameter; (d) the normalised orbital excursion diameter; (e) the flow Reynolds number and (f) the sediment Reynolds number. The different symbols shapes denote the different frequency conditions used: ○ - 0.8 Hz; □ - 1.0 Hz; △ - 1.2 Hz, while the fill indicates the sediment type: open - 242 μm; filled - 372 μm

4.3 SUMMARY AND DISCUSSION

This chapter introduced a new method to parameterise wave-formed rippled beds in terms of their spectral density function so that the observed spatial variation of ripple parameters could be taken into account in ripple prediction and modelling applications.

The chapter began by highlighting the need for a parameterisation that takes into account the spatial variation across the rippled bed. This was done by examining the variability of the ripple parameters measured during this study and presented by *Williams et al.* [2004]. *Williams et al.* [2004] is one of the few studies found that have presented the standard deviation as well as the characteristic ripple parameters in their results. The rippled beds used were formed under long-crested irregular waves in the absence of other factors which add to the variability of ripple beds such as remnant ripples, benthic organisms, currents and two-dimensional surface wave spectra. However, there was still substantial variation evident within the measured parameters over small spatial scales. Under real sea conditions the expectation is that there would be an even higher level of variation in ripple parameters over spatial scales similar to those investigated by this study. An interesting trend was determined by plotting the variation of ripple parameters against six of the more widely used non-dimensional numbers. The overall trend was for the ripple variation to start at a high value drop to a minimum then increase back to a high value as the mobility conditions were increased. To the author's knowledge this type of analysis on the variability of ripple parameters has not be undertaken previously. It highlights the bias ripple prediction methods have in predicting ripples formed under medium mobility conditions. At higher and lower mobility conditions ripples will be inherently variable with a distribution of ripple parameters existing on a given bed.

The spectral method developed to parameterise the rippled surface in terms of its major frequency components was presented and discussed in Section 4.2. A major issue in using the spectral density function of the sediment surface to classify rippled beds is the presence of low frequency trends within the data. These trends skew the spectra towards the low frequency end of the spectrum. This is not generally an issue in surface wave modelling as the water surface can be assumed to be flat over small temporal scales with

wave forms being thought of as perturbations from this surface. To overcome this problem a method using a spectral filter to isolate the ripple frequencies from the surrounding background noise was presented in Section 4.2.2. This method worked very well for the experimental data presented, as shown by comparing Figures 3.6 and 4.6. The selection of the banding frequencies was somewhat arbitrary and was based on a prior guess as to the value of the ripples spatial frequencies. If this method was to be applied to other data, especially field data, then some preprocessing of the data to set the banding frequencies would be necessary. Once the ripple spectra were filtered they were compared and the trends in the peak spectral parameters highlighted. The observed trends were found to agree with the generally accepted behavior of wave-formed ripples.

Section 4.2 ended with the description of a set of spectral shape parameters being a spectral width factor and a spectral peakedness parameter. No definite dependence was found between the width factor and six of the more widely used non-dimensional numbers, which was unexpected as the width of the spectrum indicates the level of variation across the rippled bed. A slight dependence was found between the peakedness parameter and the non-dimensional numbers used, however, the linear correlation was only slight. The use of the two spectral parameters represents a branch in this body of work which did not provide any useful application. It was hoped that the use of these parameters would allow the ripple spectrum to be related to the flow and sediment conditions, however, this was not the case and the results are only included here for completeness.

The parameterisation of wave-formed rippled beds in terms of their spectral density function has the potential to lead to significant improvements in the way rippled beds are parameterised and modelled. In the same way as the parameterisation of surface waves in terms of their spectral density function has increased the ability to classify and model wind generated wave fields, studies of rippled beds would benefit from the increased detail and ease a spectral method would bring.

Chapter 5

Rippled Bed Prediction

A spectral parameterisation for wave-formed rippled beds was presented in Chapter 4 to overcome the previously reported and observed spatial variation of ripple parameters. To use the ripple spectrum to its full potential to characterise and model a rippled sediment bed it is essential that the spectrum be related to the flow conditions and sediment properties under which the rippled bed formed. There has been a substantial number of studies that have derived prediction methods for rippled beds based on the characteristic ripple height and length (refer to Section 2.1.1). However, there have been no studies found that have tried to establish a predictive functional form for the spectral density function of the sediment surface under the action of waves. This chapter will outline a method that will allow the ripple spectrum to be predicted from surface wave conditions and sediment properties.

This chapter contains three main sections. The first section examines the relationship between the water surface and ripple spectra. A major issue in directly comparing the two spectra is that they have different dimensions. To overcome this issue a scaling method to convert the surface wave frequency spectrum to a spatial frequency spectrum is derived and discussed. After converting the spectrum, comparisons between the two spectra in terms of peak values, total energy and spectral shapes are presented and discussed. The second section takes a different approach and derives a non-dimensional form of the ripple spectrum based on the flow conditions which formed the bed and the sediment properties of the bed. A method is then developed that allows the non-dimensional and

hence dimensional ripple spectra to be estimated from the flow conditions and sediment properties through the use of an empirically derived spectral form. The theoretical spectral form is similar to the spectral forms that are widely used in surface wave applications (i.e. JONSWAP, Pierson-Moskowitz spectral forms). The third section will determine the performance of the spectral method by comparing the ripple predictions with other more accepted ripple prediction methods. The performance of the spectral method will be determined for both laboratory and field scale ripples. The chapter will conclude with a discussion of the prediction method for the ripple spectrum with conclusions highlighted.

5.1 THE WAVE-RIPPLE SPECTRAL RELATIONSHIP

The relationship between the water surface and the rippled bed spectra is extremely complicated. The two spectra are linked via the bottom orbital velocity spectrum which is a function of the depth of water and the surface wave properties. As the water becomes deeper the velocity spectrum becomes successively more narrow banded [*Mathisen and Madsen*, 1999] and, according to linear wave theory, finally disappears at some finite depth which is a function of the surface wave conditions. This section will look at the relationship between the water surface and ripple spectra in terms of their peak spectral densities, peak spatial frequencies, spectral shapes and total energy levels. As outlined above, a major issue in the direct comparison of the two spectra is that they have different dimensions. Hence, before the spectral relationships can be compared a conversion method for the surface wave spectra will be presented.

5.1.1 Conversion of the Water Wave Spectrum

As discussed in Section 3.3.1 the water surface is measured as a temporal series while the ripple surface is measured as a spatial series. Hence, the two spectra have different units: the water surface spectrum has spectral energy units of m^2/Hz and frequency units of Hz, while the ripple spectrum has energy units of $m^2/m^{-1} \Rightarrow m^3$ and frequency units of $1/m$. This problem can be overcome by first converting the water surface spectrum to

a wavenumber spectrum then to a spatial frequency spectrum.

The wavenumber spectrum of the water surface can be related to the frequency spectrum of the water surface by noting that the area under both variance spectra are equal to the variance of the series [*Young*, 1999]. This is mathematically equivalent to:

$$\sigma^2 = \int Q_w(k)\, dk = \int S_w(f)\, df \tag{5.1}$$

where σ^2 is the variance (m^2); k is the water surface wavenumber (rad/m); f is the water wave frequency (Hz); Q_w is the water surface wavenumber spectrum (m^3/rad) and S_w is the water surface frequency spectrum (m^2/Hz). Solving equation 5.1 for the wavenumber spectrum gives:

$$Q_w(k) = S_w(f)\, \frac{df}{dk} \tag{5.2}$$

where df/dk can be determined from the water wave dispersion relation, given as:

$$f = \frac{\sqrt{gk\tanh(kd)}}{2\pi} \tag{5.3}$$

where g is the gravity constant (m/s^2) and h is the water depth (m). Differentiating equation 5.3 with respect to the wavenumber gives:

$$\frac{df}{dk} = \frac{g\tanh(kh) + khg(1-\tanh^2(kh))}{4\pi\sqrt{gk\tanh(kh)}} \tag{5.4}$$

The water surface frequency spectrum can be scaled to a wavenumber spectrum by using equation 5.2. However, the units on the wavenumber spectrum are still not the same as those used for the ripple spectrum. The water surface wavenumber spectrum has spectral energy units of m^3/rad and frequency units of rad/m, while the ripple spectrum has energy units of m^3 and frequency units of $1/m$. This dimensional problem is overcome by multiplying the spectral energy by 2π (rad) and dividing the frequency by 2π (rad). A simple check to determine if the above conversion is correct is to use equation 5.1, which states that the energy in one domain should equal the energy in the other which equals the variance of the series. Figure 5.1 provides an example of converting a typical water surface spectrum from a frequency spectrum to a spatial frequency spectrum. The

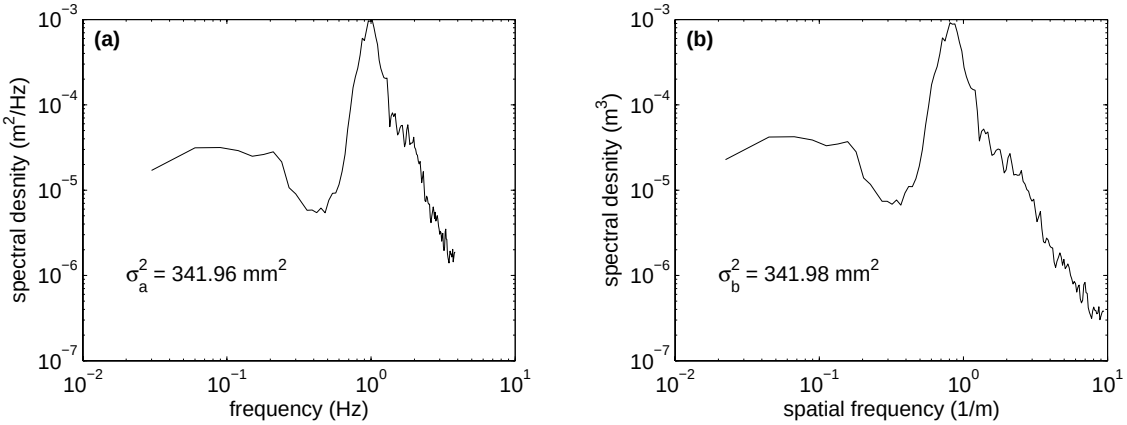

Figure 5.1 Conversion of the water surface spectrum where: (a) is the water surface frequency spectrum and (b) is the water surface spatial frequency spectrum. The area under both spectra (the variance σ^2) is shown in the figures. $\sigma_a^2/\sigma_b^2 = 0.9999$

example is shown as test E22_TA2 in Table 3.3 (page 57). The area under both spectra (the variance σ^2) is shown in the figures to enable the conversion method to be compared.

Taking the ratio of the two variances, shown in Figure 5.1, demonstrates that the conversion method employed works very well with a ratio value close to unity. The conversion of the water surface spectrum to the spatial frequency domain allows a direct comparison between the water surface spectrum and the bottom ripple spectrum to be undertaken. The next section will present the results of a comparison analysis that attempts to relate the two spectra in terms of the peak values, spectral shapes and total energy.

5.1.2 Spectral Comparisons

This section will outline a number of parameters that are calculated from the water surface and ripple spectra so that a comparison between the two spectra can be made. Figure 5.2 presents the water surface and ripple spectra plotted on the same axes for the test shown as E22_TA2 in Table 3.3. As expected the water surface spectrum contains more energy at a lower spatial frequency than does the ripple spectrum. This simply means that the surface waves were higher and longer than the ripple forms.

To compare the water surface and ripple spectra for the 40 equilibrium tests (refer to Table 3.3) five parameters were used: the peak spectral density and peak spatial frequency

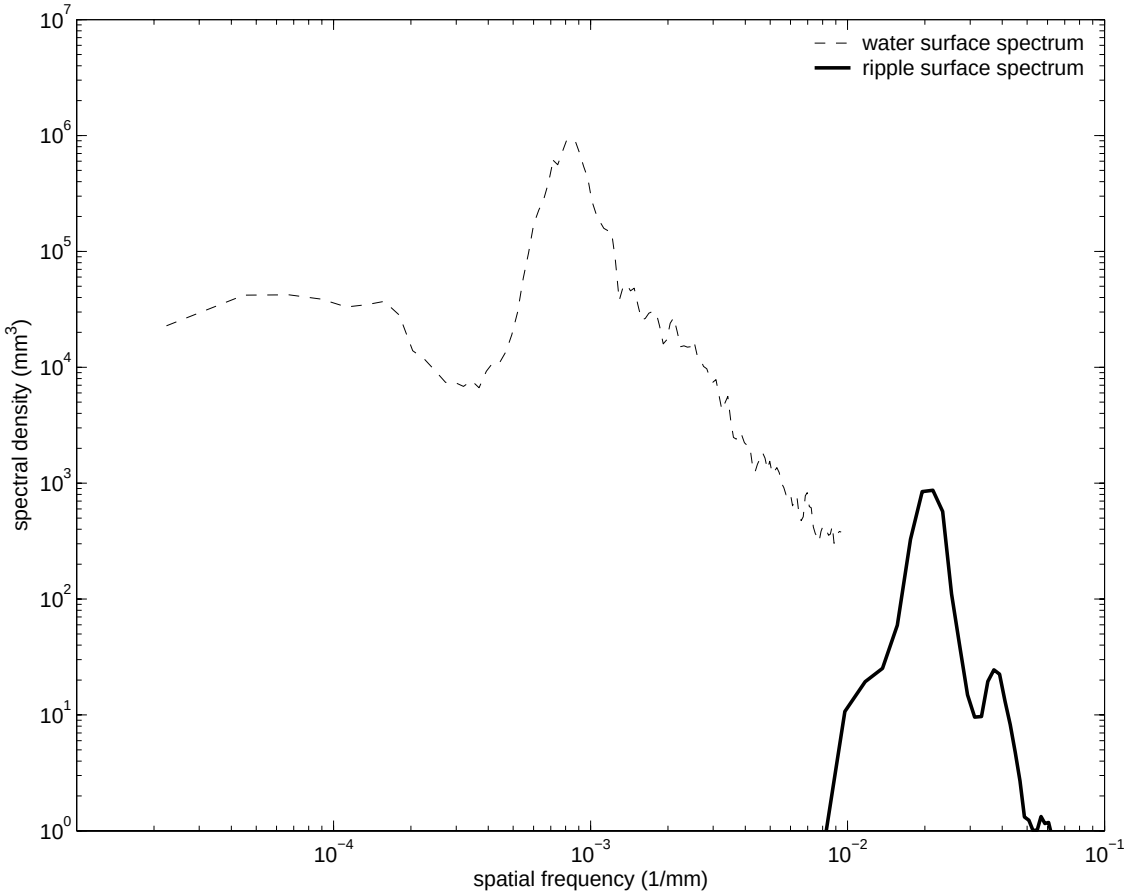

Figure 5.2 The spatial frequency water surface and ripple spectra plotted on the same axes. The water surface spatial frequency spectra is shown as the dotted line while the ripple spectra is shown as the bold line.

values in each spectra (S_{vp} and f_{sp}); the spectral width factor (v refer to equation 4.3, page 86); the spectral peakedness parameter (Q refer to equation 4.5, page 86), and the total average energy of the wave series ($\bar{E}$). *Young* [1999] defined the total average energy of the wave series as:

$$\bar{E} = \rho g \sigma^2 \tag{5.5}$$

where ρ is either the density of water or of the sediment (kg/m^3) and $\bar{E}$ is the total average energy of the wave profile ($kg/s^2 \Rightarrow J/m^2$). The density of the sediment was taken as 2650 kg/m^3, while the water was assumed to have a density of 1000 kg/m^3.

Figure 5.3 presents the comparison between the peak spectral density and peak spatial

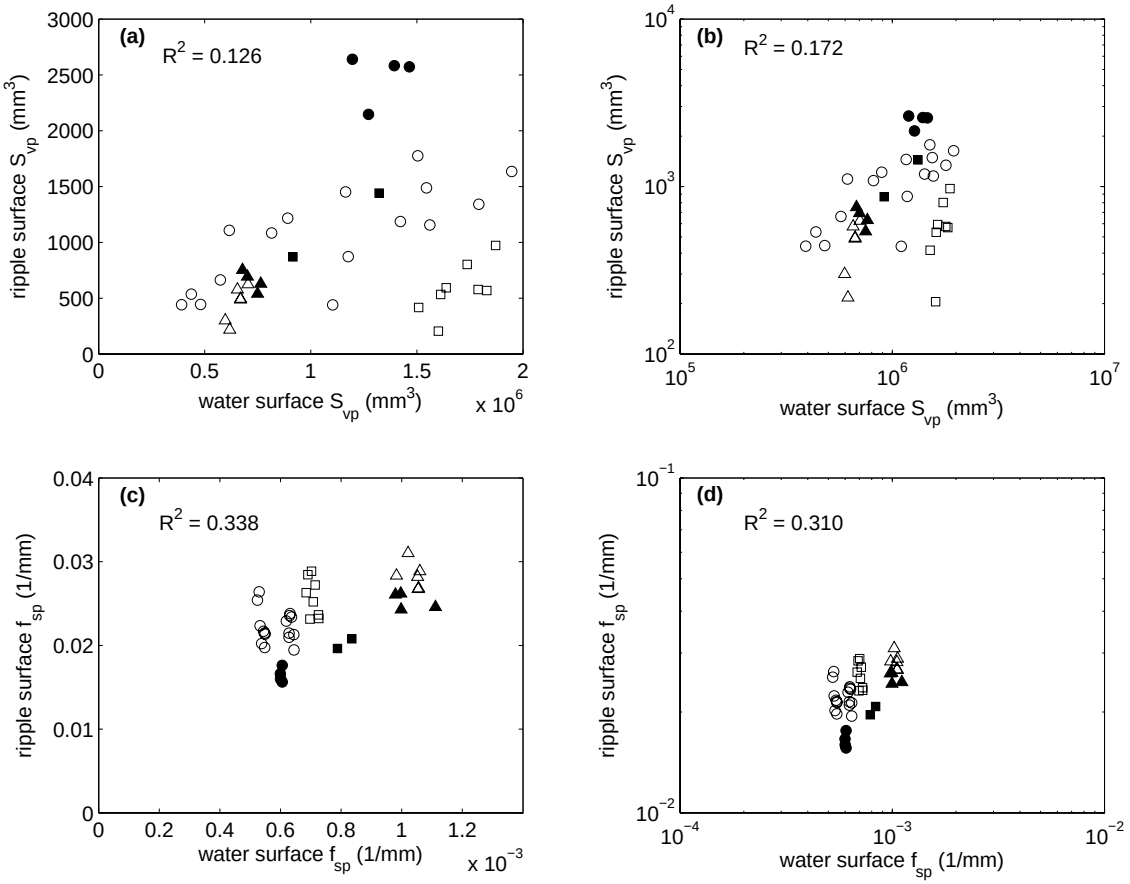

Figure 5.3 Comparison between the peak values of the water and ripple spectra. The left hand side show the linear-linear plots while the right hand side shows the log-log plots. The different symbols shapes denote the different frequency conditions used: ○ - 0.8 Hz; □ - 1.0 Hz; △ - 1.2 Hz, while the fill indicates the sediment type: open - 242 μm; filled - 372 μm

frequency of the water surface and ripple spectra. The linear-linear plots are shown on the left hand side of Figure 5.3, while the right hand side shows the log-log plots.

The top two plots, (subplots a and b) in Figure 5.3 show the relationship between the peak spectral density for the water surface and ripple spectra. There is considerable scatter in both plots with a low linear correlation ($R^2 < 0.2$) evident between the two variables. There is a slight trend in Figures 5.3a and 5.3b that suggests that as the peak spectral density of the water surface spectra increases there is an increase in the peak spectral density of the ripple spectra. The bottom plots (subplots c and d) in Figure 5.3 show the relationship between the peak spatial frequency of the water surface spectra and

the ripple spectra. Once again there is a trend which suggests that as the peak spatial frequency of the surface spectra increased there was a corresponding increase in the peak spatial frequency of the ripple spectra. However, as shown by the values of the linear correlation coefficient the trend was considered weak ($R^2 < 0.3$). From the relationships shown in Figure 5.3 it was concluded that there was a relationship between the peak values of the surface wave spectra and the peak values of the ripple spectra, but this relationship was weak.

Figure 5.4 presents a comparison between the two spectral shape parameters: the spectral width factor and peakedness parameter of the water surface and ripple spectra. The spectral width factor and peakedness parameter were presented and discussed in Section 4.2.4. As with Figure 5.3 the left hand side are the linear-linear plots while the right hand side shows the log-log plots.

The relationship between the spectral width factors for the water surface and the ripple spectra are shown in Figures 5.4a and 5.4b. As can be seen in these figures, there was no real trend in the relationship between the two width factors. The width factor of the surface waves varies between 0.5 and 0.9 which seems to be a function of the surface wave frequency as shown by the different frequency symbols. However, the width factors of the ripple spectra only varied slightly between 0.2 and 0.4 and were very similar for all the tests undertaken. This would indicate that the width of the ripple spectra is approximately constant and is not affected by the flow conditions. As shown by the correlation coefficient there is only a weak linear correlation between the two variables ($R^2 < 0.1$). Undertaking a log-log analysis of the data did not improve the correlation (refer to Figure 5.4b).

The two bottom plots in Figure 5.4 show the relationship between the spectral peakedness parameter calculated from the water surface and ripple spectra. Once again there is a very weak linear correlation between the two parameters ($R^2 < 0.1$). Interestingly, the trend that was evident in Figure 5.4a is reversed in Figure 5.4b with the peakedness parameter varying substantially for the ripple spectra and staying relatively constant for the water surface spectra. The peakedness parameter relates to the JONSWAP peakedness (γ) factor and was set in the wave generation software at a value of 3.3, corresponding

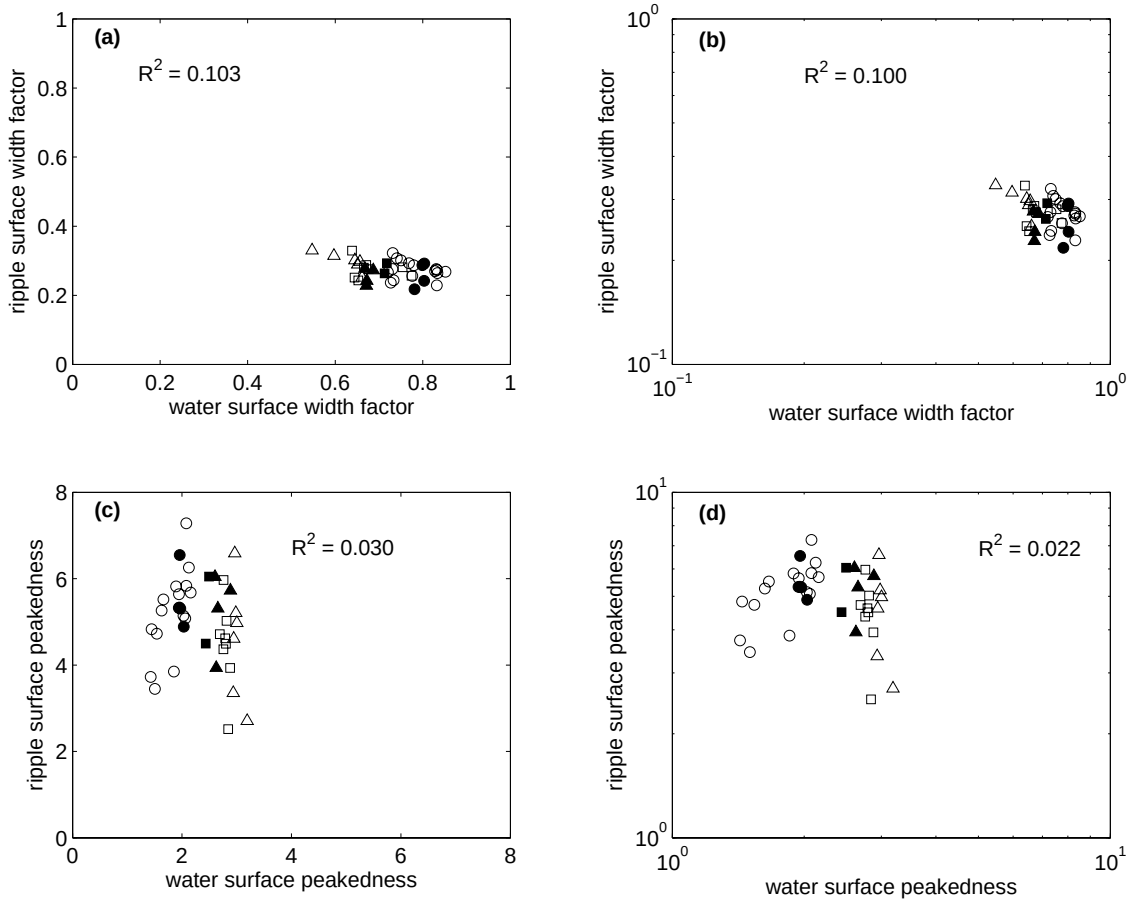

Figure 5.4 Comparison between the shape parameters of the water and ripple spectra. The left hand side show the linear-linear plots while the right hand side shows the log-log plots. The different symbols shapes denote the different frequency conditions used: ○ - 0.8 Hz; □ - 1.0 Hz; △ - 1.2 Hz, while the fill indicates the sediment type: open - 242 μm; filled - 372 μm

to a standard JONSWAP spectrum (refer to Section 3.1.1). However, there was some deviation from this value in the wave spectra measured in the wave flume as shown in Figure 5.4. As with the width factor, plotting the peakedness parameter in log-log space did not improve the correlation between the two parameters.

Overall the water surface spectral shape parameters, shown in Figure 5.4, do not provide an effective method to estimate the shape of the ripple spectra. The correlations between the shape parameters are weak with no real trend being able to be derived from Figure 5.4.

Figure 5.5 presents the relationship between the total average energy of the water

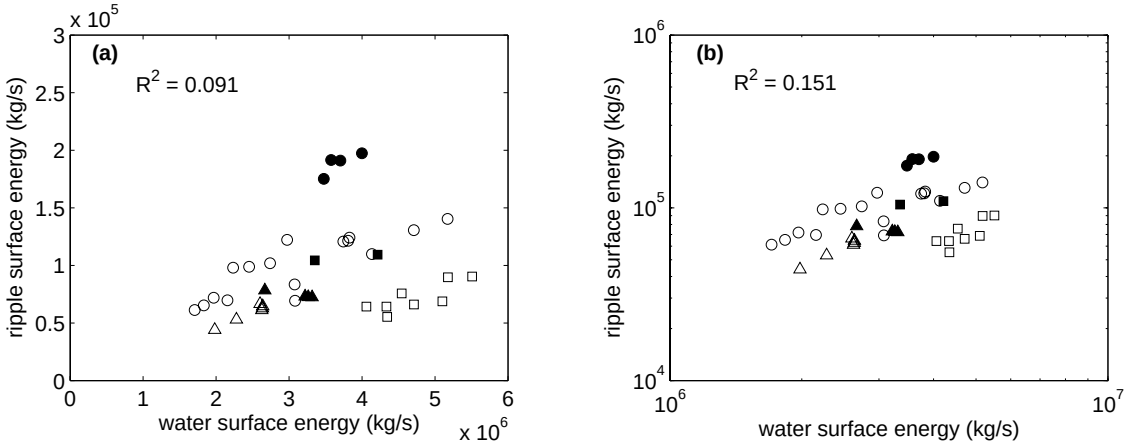

Figure 5.5 Comparison between the energy of the water and ripple spectra. The different symbols shapes denote the different frequency conditions used: ○ - 0.8 Hz; □ - 1.0 Hz; △ - 1.2 Hz, while the fill indicates the sediment type: open - 242 μm; filled - 372 μm

surface and ripple spectra (refer to equation 5.5). The left hand side plot shows the linear-linear relationship while the right hand side shows the log-log relationship.

There is a trend evident in Figure 5.5 with the total energy within the ripple spectra increasing as the total energy of the water surface spectra is increased. However, as with the other comparison figures of this section there is a large scatter in the experimental data set and hence the trend is not conclusive. There is only a very weak linear correlation ($R^2 < 0.2$) between the two variables in both linear-linear and log-log space.

As outlined at the start of this section, the interaction between the water surface and the ripple surface is very complicated. It was felt that some type of functional dependance between the two spectra should exist. This section outlined a number of methods that attempted to develop a functional dependence between the water surface and bottom ripple spectra. This would enable the calculation of the ripple spectrum from the water surface spectrum without the need to calculate the bottom orbital velocity spectrum. However, as was shown from this analysis there were only weak correlations evident between the parameters calculated from the water surface and ripple spectra. As such, no definite trends were able to be derived that would allow the bottom ripple spectra to be estimated from the surface wave spectrum. To the author's knowledge this type of spectral analysis

has not been attempted before on rippled beds and with further tests may yet yield some useful results. However, for the data presented in this section, these types of relationships were found to be inconclusive. The next section will outline a different approach that utilises a non-dimensional form of the ripple spectra to estimate the ripple spectrum from surface wave conditions and sediment bed properties.

5.2 PREDICTION OF THE RIPPLE SPECTRUM

Section 2.1.1 presented four of the more widely used ripple prediction methods [*Nielsen*, 1981; *Grant and Madsen*, 1982; *Wiberg and Harris*, 1994; *Mogridge et al.*, 1994]. The limitation of these traditional ripple prediction methods is that they fail to take into account either the spatial or temporal variability of the ripple field. This section will present the development of a new empirical ripple prediction method which uses a non-dimensional form of the ripple spectrum. The ripple spectrum is a comprehensive way to characterise an area of the ripple surface which takes into account the spatial variation of ripple parameters across the bed. Hence, developing a prediction method for the ripple spectrum will enable the inherent variability of rippled beds to be incorporated into the analysis.

5.2.1 The Non-Dimensional Ripple Spectrum

The trends evident in the spectral forms presented in Figure 4.8 (page 84) suggest that a non-dimensional model incorporating flow parameters and sediment properties could be established. This type of model would allow the ripple spectrum to be estimated from the surface flow conditions and sediment bed properties. This section presents and discusses the non-dimensional scaling that was applied to the ripple variance spectrum so that the different spectra could be directly compared.

Nordin [1971] presented a non-dimensional model for current-formed ripples generated under both laboratory and field conditions. As discussed in the previous section rippled sediment beds are sampled as a spatial series which is not dependent on time, thus, a time scale is not required to derive a non-dimensional form for the resulting spectrum.

Nordin [1971] used the ratio of the gravity constant (m/s^2) over the flow velocity squared (m^2/s^2) to develop a length scale for the unidirectional flowing water, but did not include any length scale for the sediment bed in his analysis. *Nordin* only found weak log-log relationships between non-dimensional spectra with appreciable scatter in his results. As discussed in Section 2.3.1, there have been no studies that have used the bottom spectra to analyse wave-formed ripples and relate this spectrum back to flow and sediment conditions. This is surprising since wave-formed ripples generally have symmetrical shapes and a well defined flow length scale, being the orbital excursion diameter. Hence, developing a spectral analysis method to classify and predict wave-formed ripples should be easier and more intuitive than undertaking the same analysis on current-formed ripples which do not have a well defined flow length scale.

A number of authors [*Nielsen*, 1981; *Mogridge et al.*, 1994; *Wiberg and Harris*, 1994] have suggested that the length and the height of small scale wave formed ripples will scale to the orbital excursion diameter of the wave motion and be dependent on the 50 percentile grain size diameter. These studies developed relationships for ripple parameters through the use of a number of non-dimensional numbers, being either the mobility number [*Nielsen*, 1981], the wave period parameter [*Mogridge et al.*, 1994], or the ratio of orbital excursion diameter to the sediment grain diameter [*Wiberg and Harris*, 1994]. It follows that with respect to ripple development, the most important flow length scale, within the oscillatory bottom boundary layer, will be the orbital excursion diameter, while the 50 percentile grain size diameter will be an adequate length scale for the sediment bed.

A number of different non-dimensional numbers were tested during this study, however, only two gave satisfactory results to provide a non-dimensional form of the ripple spectrum. The two non-dimensional numbers developed used the two length scales discussed above: the peak orbital excursion diameter (d_{op}) and the median grain diameter (D_{50}). The peak orbital excursion diameter was calculated using the method presented in Section 3.2 (equation 3.8, page 54). The first non-dimensional number scales the spectral energy of the rippled bed as:

$$S' = \frac{S_r}{d_{op}^2 D_{50}} \tag{5.6}$$

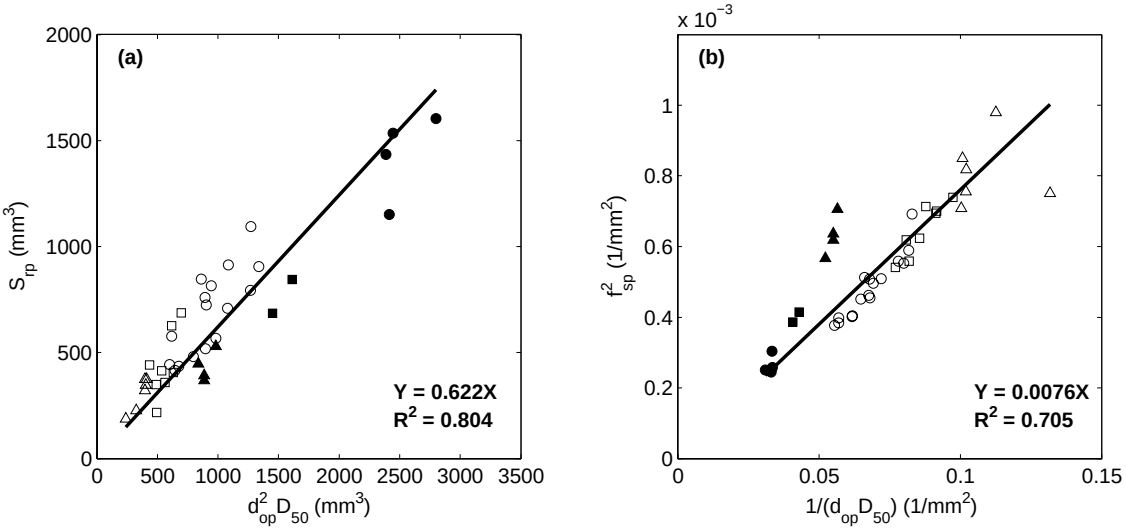

Figure 5.6 The effectiveness of the non-dimensional spectral form shown by: (a) equation 5.6, and (b) equation 5.7. The different symbols shapes denote the different frequency conditions used: ○ - 0.8 Hz; □ - 1.0 Hz; △ - 1.2 Hz, while the fill indicates the sediment type: open - 242 μm; filled - 372 μm

where S_r is the ripple variance spectrum (mm^3) and S' is the non-dimensional ripple spectrum. The second non-dimensional number scales the spatial frequencies of the rippled bed as:

$$f'_s = d_{op} D_{50} f_s^2 \tag{5.7}$$

where f_s is the spatial frequency (mm^{-1}) and f'_s is the non-dimensional spatial frequency.

To establish how well the ripple spectral parameters correlate with the flow and sediment parameters two linear plots were developed (refer to Figure 5.6). Figure 5.6a plots the peak spectral density of the spectra shown in Figure 4.8 against the orbital excursion diameter squared times the median grain diameter for the particular test. Figure 5.6b shows the relationship between the peak spatial frequency of the ripple spectra shown in Figure 4.8 against the inverse of the orbital excursion diameter times the characteristic grain diameter for the particular test. As with other results presented the details of the 40 equilibrium tests undertaken are presented in Table 3.3 (page 57).

Figure 5.6a shows the relationship represented by equation 5.6. There is a high linear correlation ($R^2 = 0.804$) between the peak spectral density and the peak orbital excur-

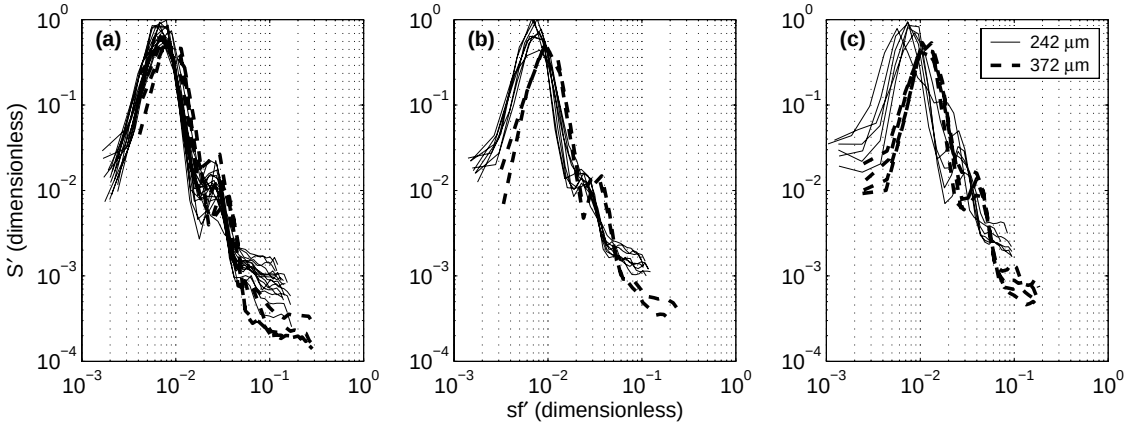

Figure 5.7 The non-dimensional ripple spectra for the experimental tests grouped by surface wave frequency: (a) 0.8; (b) 1.0 and (c) 1.2 Hz tests. Different line types indicate the different types of sediment used in the tests.

sion diameter squared multiplied by the median diameter. This correlation is across the range of rippled beds that could be generated in the wave flume used to undertake the experiments.

Figure 5.6b illustrates the relationship represented by equation 5.7. Once again there is a high linear correlation ($R^2 = 0.705$) between the two variables displayed over a range of conditions. However, this relationship is not as convincing as the relationship shown in Figure 5.6a due to the separation of sediment sizes in the plot. The coarser sediment (filled shapes) data points all lie above the line in a separate group compared to the finer sediment (open shapes). It is possible that there could be two best fit lines fitted to the data set, one for each sediment size. However, the correlation coefficient shown in Figure 5.6b was fitted to the complete data set and, as such, it was concluded that the relationship shown by equation 5.7 provided the best way to non-dimensionalise the spectral frequency axis.

Figure 5.7 shows the same 40 spectra as shown in Figure 4.8 in their non-dimensional form. Once again for clarity, the spectra are grouped in each subplot by the surface wave frequency used to form the rippled bed. The two line types indicate the sediment size.

As shown in Figure 5.7, scaling the ripple spectra by the flow conditions and sediment properties using equations 5.6 and 5.7 has resulted in all the spectra showing similar non-dimensional peak spectral energy levels and non-dimensional peak spatial frequencies.

This enables ripple spectra formed under different flow regimes and on different sediment beds to be compared. However, it has to be emphasised that the non-dimensional spectrum described by equations 5.6 and 5.7 does not represent a variance spectrum and hence the area under the spectral curve will not equal the variance of the series.

The agreement among the three plots, shown in Figure 5.7, is very high in terms of spectral energy levels obtained. In terms of spectral frequency (equation 5.7), however, the agreement is not as high, especially for the tests undertaken with the coarser sediment type. Interestingly as the surface wave frequency was increased there was a corresponding decrease in the agreement between the spectra in terms of peak spatial frequency values. A possible reason for this is that, due to the higher frequency surface waves and the coarser sediment type used to form the rippled bed, these ripples did not reach a fully developed equilibrium state and were still in the process of developing. This point will be discussed further in Chapter 6. However, this deviation in spatial frequency values was only slight and well within the scatter that is to be expected from experimental results. Hence, it was concluded that equations 5.6 and 5.7 provided an acceptable non-dimensional form for the ripple spectrum.

This section has presented an effective non-dimensional form for the ripple spectrum. The non-dimensional spectral form is based on rippled beds formed under a number of different flow conditions and sediment types. This has provided a method which allows the different ripple spectra to be compared, but still does not provide a method which will enable the spectrum to be estimated from the surface wave conditions. The next section will introduce a theoretical spectral form similar to those used in water wave theory, which will be used to estimate the ripple spectrum.

5.2.2 The Non-Dimensional Spectral Form

The non-dimensional ripple spectra presented in Figure 5.7 display similar peak values and shapes over the range of flow conditions and sediment properties used in the experimental tests. This similarity allows a function to be fitted through the data points contained in the 40 spectral curves. The aim is to provide an estimate of the non-dimensional

spectrum given a range of non-dimensional spatial frequencies, i.e., $S' = g(f_s')$ where $g(f_s')$ is some function of the spatial frequency. The main issue in undertaking such an empirical fitting process is to determine the form of the function to fit to the data set. As discussed in Section 2.3.2, previous work on deriving theoretical spectral forms for the sediment surface have mainly concentrated on the seafloor as a whole and have largely been based on a power law model (equation 2.31, page 36), as originally derived by *Hino* [1968], which is fitted to the decay of the spectrum at higher frequencies. The power law relationship plots as a straight line in log-log space and therefore cannot be used to adequately describe the ripple spectra presented in Figure 5.7. As shown in Figure 5.7, the spectral energy across the ripple bands is not linear in log-log space, but parabolic in shape.

After testing a number of functional forms, only two relationships were determined to be viable options. These two forms will be presented and discussed in this section. The first functional form was based on the exponential of a parabolic function:

$$S' = \exp(a_2 {f_s'}^2 + a_1 f_s' + a_0) \tag{5.8}$$

where a_2, a_1 and a_0 are the three fitting parameters used to fit the function to the non-dimensional spectra. The second spectral form was a modification of the power law model and is largely based on the *Pierson and Moskowitz* [1964] water wave spectral form. This functional form is given as:

$$S' = \frac{\alpha}{(f_s')^\gamma} \exp\left[-\beta \left(\frac{f_s'}{\Theta}\right)^n\right] \tag{5.9}$$

where α, γ, β, n, and Θ are the 5 parameters used to fit the spectral curve to the non-dimensional data. Both equations were fitted to the data set shown in Figure 5.7 using a Levenberg-Marquardt nonlinear multiple regression technique. Figure 5.8a shows the result of fitting equation 5.8, while Figure 5.8b presents equation 5.9 fitted to the non-dimensional spectra. In both subplots the fitted equation is shown as the bold line while the 40 non-dimensional ripple spectra are shown as the lighter grey curves.

As can be seen the spectral data shown in Figure 5.10 is quite noisy especially at lower and higher spatial frequencies. The lower frequency noise show in the spectra was due to

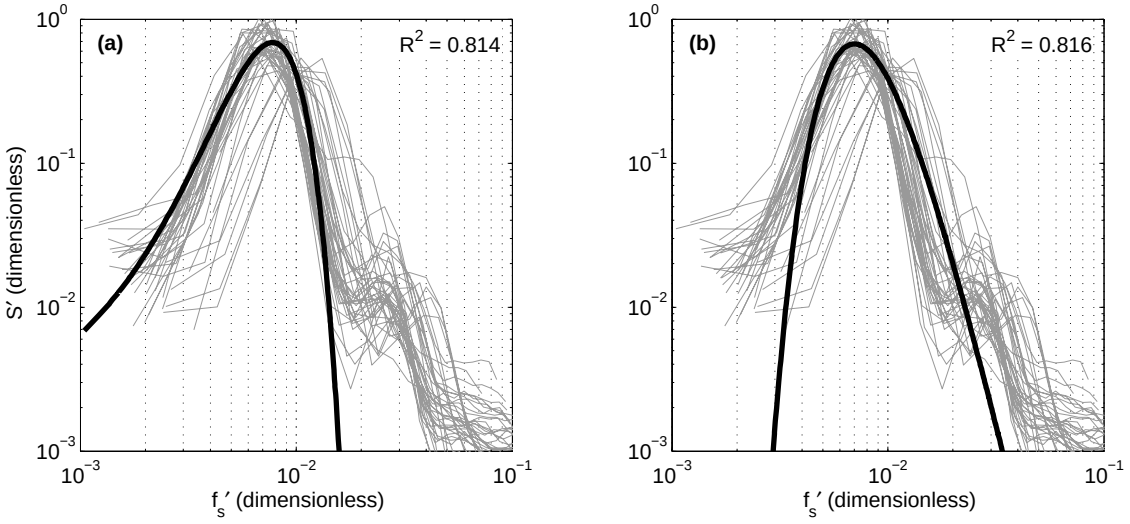

Figure 5.8 Fitted functional forms of the non-dimensional ripple spectra where (a) is the relationship shown by equation 5.8 and (b) is the relationship shown by equation 5.9. The bold lines in each subplot represents the fitted equations, while the grey lines represent the 40 non-dimensional spectral curves shown in Figure 5.7.

the filtering method employed not being set at a correct limit for the particular data set. All curves were filtered using the same banding frequencies (refer to Section 4.2.2) which has left some low frequency noise in the spectra. This noise is an order of magnitude lower than the peak non-dimensional spectral density and hence does not contribute greatly to the total spectral energy of the bed. The high frequency noise is shown as the horizontal line at the higher end of the spectral curves. The higher frequency noise is left over from the filtering process and is almost two orders of magnitude lower than the value of the peak spectral density. Another issue in regards to fitting the spectra is the kink in the non-dimensional spectral curves due to the second harmonic. As discussed in Section 4.2.1, the higher harmonics evident in the ripple spectra were due to the shape of the ripple forms. It was very hard to try and fit an equation to the data set that would take into account the second harmonic present in the spectral curves. However, as with the low and high frequency noise the level of energy contained in this region is very small, compared to the peak.

As shown in Figure 5.8, equations 5.8 and 5.9 both fit the data very well in the vicin-

Table 5.1 Fitting parameters of equation 5.9

Parameter	Fitted Value
α	3.9 $\times 10^{-13}$
γ	6.5
Θ	0.007
n	-1.59
β	4.11

ity of the spectral peak with high values of the correlation coefficient being recorded. Equation 5.8 fits the data better at low spatial frequencies, but fails to match the decay of the spectra at higher spatial frequencies. Equation 5.9 matches the decay of the spectra at higher frequencies, but does not match the spectrum as well as equation 5.8 at lower spatial frequencies.

It was decided to use equation 5.9 in preference to equation 5.8 because this equation fitted the higher spatial frequency decay of the spectra better, had a slightly higher R^2 value, and was more symmetrical about the peak spatial frequency. As seen in Figure 5.8a, equation 5.8 was quite skewed. Table 5.1 lists the values of the fitting parameters used in equation 5.9 to obtain the fit shown in Figure 5.8.

Using equations 5.6, 5.7, and 5.9, a theoretical dimensional form of the ripple spectrum can be derived which is a function of the spatial frequency, peak orbital excursion diameter and the 50 percentile sediment diameter. This theoretical dimensional form is given as:

$$S_r(f_s) = \frac{\alpha(d_{op}^2 D_{50})}{(d_{op} D_{50} f_s^2)^\gamma} \exp\left[-\beta \left(\frac{d_{op} D_{50} f_s^2}{\Theta}\right)^n\right] \tag{5.10}$$

which represents the theoretical variance spectrum of a rippled bed based on a given flow condition and grain size.

This section has presented a method which enables the ripple spectrum to be estimated from the flow conditions and the sediment properties through the use of a non-dimensional spectral form. The next section will assess the performance of the spectral method shown by equations 5.9 and 5.10 by comparing it to other ripple prediction methods for both laboratory and field scale ripples.

5.3 PERFORMANCE OF THE SPECTRAL METHOD

The ripple prediction method, presented in the previous section, is an attempt to develop a method that will take into account the substantial variability that has been observed by numerous authors [*Amos et al.*, 1988; *Drake and Cacchione*, 1992; *Hay and Wilson*, 1994; *Wheatcroft*, 1994; *Bell and Thorne*, 1997; *Traykovski et al.*, 1999; *Hanes et al.*, 2001; *Ardhuin et al.*, 2002; *Doucette*, 2002; *Moore and Jaffe*, 2002] on rippled beds formed under a variety of conditions. It has to be emphasised that this method represents a first step in regards to using spectral methods to characterise wave-formed rippled beds and has been developed on only a relatively small data set generated by a limited range of flow conditions (refer to Table 3.3). To assess the performance of the spectral method, the method is compared to both laboratory and field scale conditions in this section. To facilitate this comparison two ripple parameters were defined from the theoretical ripple spectrum to provide a measure of the characteristic ripple height and ripple length.

The characteristic ripple height (η_c) was defined as a direct analogy to the significant water wave height, in that it uses the variance of the record to calculate a characteristic height of the series. The significant water wave height is defined as the average of the highest 1/3 of the waves within the surface wave time series and is approximated from the surface wave variance spectrum as four times the square root of the area under the spectral curve [*Massel*, 1996; *Young*, 1999]. The area under the variance spectral curve is equal to the variance of the series [*Young*, 1999]. As discussed in Section 4.1.2 the characteristic ripple height was defined as the ripple height that achieves the highest count in the ripple height histogram (refer to Figure 4.2, page 69). The values of the characteristic ripple heights are listed in Table 4.1 for the 40 equilibrium tests undertaken (refer to Table 3.3). This value can be related linearly to the square root of the area under the ripple spectrum. Figure 5.9a shows this relationship for the 40 tests shown in Table 3.3. The different symbols shown in Figure 5.9 relate to the three surface wave frequencies used to generate the beds and the two sediment sizes.

From the slope of the linear relationship shown in Figure 5.9a a definition can be

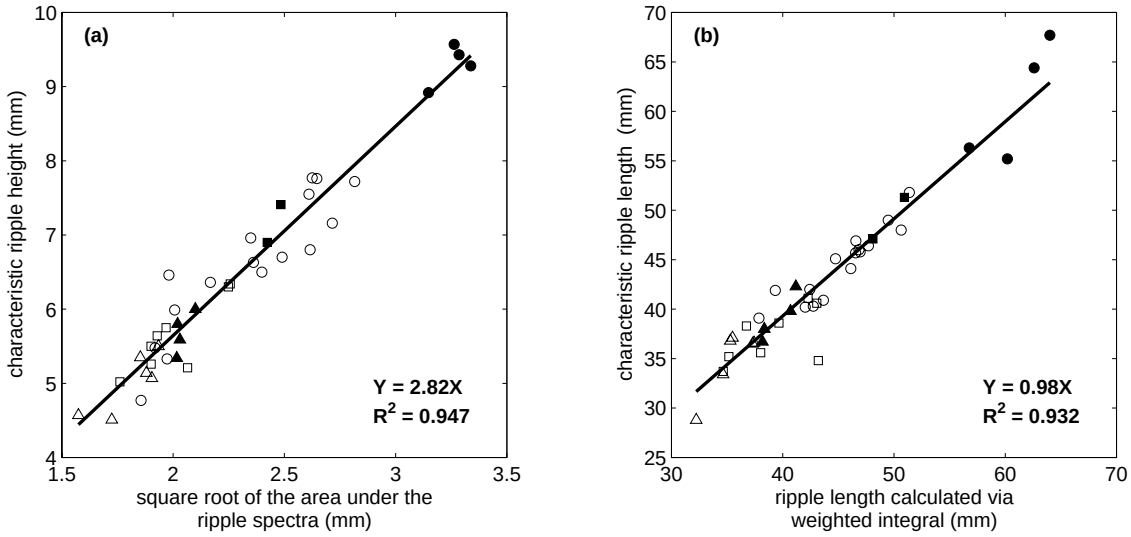

Figure 5.9 Relationship between the ripple spectrum and the characteristic ripple height and length as shown by (a) equation 5.11, and (b) equation 5.12. The different symbols shapes denote the different frequency conditions used: ○ - 0.8 Hz; □ - 1.0 Hz; △ - 1.2 Hz, while the fill indicates the sediment type: open - 242 μm; filled - 372 μm

developed for the characteristic ripple height from the ripple spectrum as:

$$\eta_c = 2.8\sqrt{\int_{f_{s1}}^{f_{s2}} S_r(f_s)\, df_s} \tag{5.11}$$

where S_r is the ripple variance spectrum (mm^3), f_s is the spatial frequency (mm^{-1}) and f_{s1} and f_{s2} are the upper and lower bounds defining the ripple spatial frequencies present in the spectrum. The multiplication factor of 2.8 used in equation 5.11 has the same value as the multiplier used to obtain the height of a sinusoidal series from the standard deviation of the record [*Hanes et al.*, 2001].

The characteristic ripple length was determined from the ripple spectrum by using the inverse of the weighted integral method that is widely used in water wave research. The accuracy of the weighted integral method was discussed in relation to the determination of the peak frequency of the water surface spectrum by *Young* [1995]. The characteristic

ripple length (λ_c) is defined as:

$$\lambda_c = \frac{\int_{f_{s1}}^{f_{s2}} S_r^4(f_s)\, df_s}{\int_{f_{s1}}^{f_{s2}} f_s S_r^4(f_s)\, df_s} \tag{5.12}$$

A comparison between the characteristic ripple lengths derived from the ripple spectra via equation 5.12 and the ripple lengths calculated from the histograms of ripple lengths, as discussed in Section 4.1.2, is provided in Figure 5.9b. As shown in Figure 5.9b, there is a good agreement between the characteristic ripple lengths derived from this histogram and the ripple lengths calculated by equation 5.12 with a near 1-to-1 relationship. It was concluded that equations 5.11 and 5.12 represent an accurate way to parameterise the theoretical ripple spectrum in terms of the traditional rippled bed parameterisations being the ripple height and length.

The performance of the spectral method for laboratory scale ripples was assessed by comparing the ripple heights and lengths predicted by the method with the ripple parameters measured as part of the experiment phase of the study. The measured ripple parameters were estimated using the zero up-crossing method as outlined by *Goda* [2000]. The same analysis was undertaken using two of the more widely used empirical ripple prediction methods of *Nielsen* [1981] (equations 2.2 and 2.3) and *Wiberg and Harris* [1994] (equations 2.12 and 2.13). This was done so that the accuracy of the spectral method could be compared to the accuracy of these previous methods. To compare the relative accuracy of each method, a goodness-of-fit coefficient (N_R) was used that was simply the norm of the normalised residual error from a 1-to-1 relationship. Mathematically this is given as:

$$N_R = \sqrt{\sum_{i=1}^{n} \left[\frac{p_{m_i} - p_{e_i}}{p_{e_i}}\right]^2} \tag{5.13}$$

where n is the number of data points, p is the ripple parameter either the ripple height or length and the subscripts m and e refer to the measured and estimated values respectively.

Figure 5.10 shows the comparison between the ripple parameters estimated using the three empirical methods and the ripple parameters estimated using the zero up-crossing

method. Interestingly for this scale of data the method of *Nielsen* [1981] slightly over predicts the ripple length while the method of *Wiberg and Harris* [1994] slightly underestimates the ripple length which highlights the large variability in ripple parameters predicted by current methods. Generally all methods shown in Figure 5.10 predict the ripple parameters adequately, with values of N_R in the same order of magnitude. However, the spectral method models the ripple parameters slightly better than the more established methods. This is to be expected as the spectral method was developed by fitting the parameters shown in Table 5.1 to the experimental data set.

There is little advantage in using the more complicated spectral method in predicting equilibrium beds such as those generated by this study. However, as will be shown in Chapter 6, the great advantage of using the spectral method is that it allows the rippled bed to be modelled with time. This allows an understanding of the temporal and spatial variability of the rippled bed to be gained through the use of the spectral method. This is not the case with previous empirical prediction methods that give little indication of the inherent variability of a given ripple parameter estimate.

A number of authors [e.g., *Clifton and Dingler*, 1984; *Wiberg and Harris*, 1994] have suggested that as the scale of flow to sediment properties increases, rippled beds display three separate scaling regimes: orbital, suborbital and anorbital. Each requires a different parameterisation to be undertaken to account for the different physical processes that become important within each regime. The experiments undertaken as part of the current study could only generate small scale orbital ripples ($d_{op}/\eta < 20$). Hence, the spectral method is only valid for ripples in this range. However, it is interesting to see how the method performs when applied to other regimes. Figure 5.11 shows the predicted ripple parameters plotted against the orbital excursion amplitude on axes normalised by the sediment diameter. The three regions shown in Figure 5.11 represent the three ripple regimes, while the open circles display the experimental data that were measured as part of the current study. The dotted line, in Figure 5.11, represents the ripple prediction method of *Wiberg and Harris* [1994] while the bold line is the spectral methods that was developed as part of this study. The method of *Wiberg and Harris* [1994] is shown because it pro-

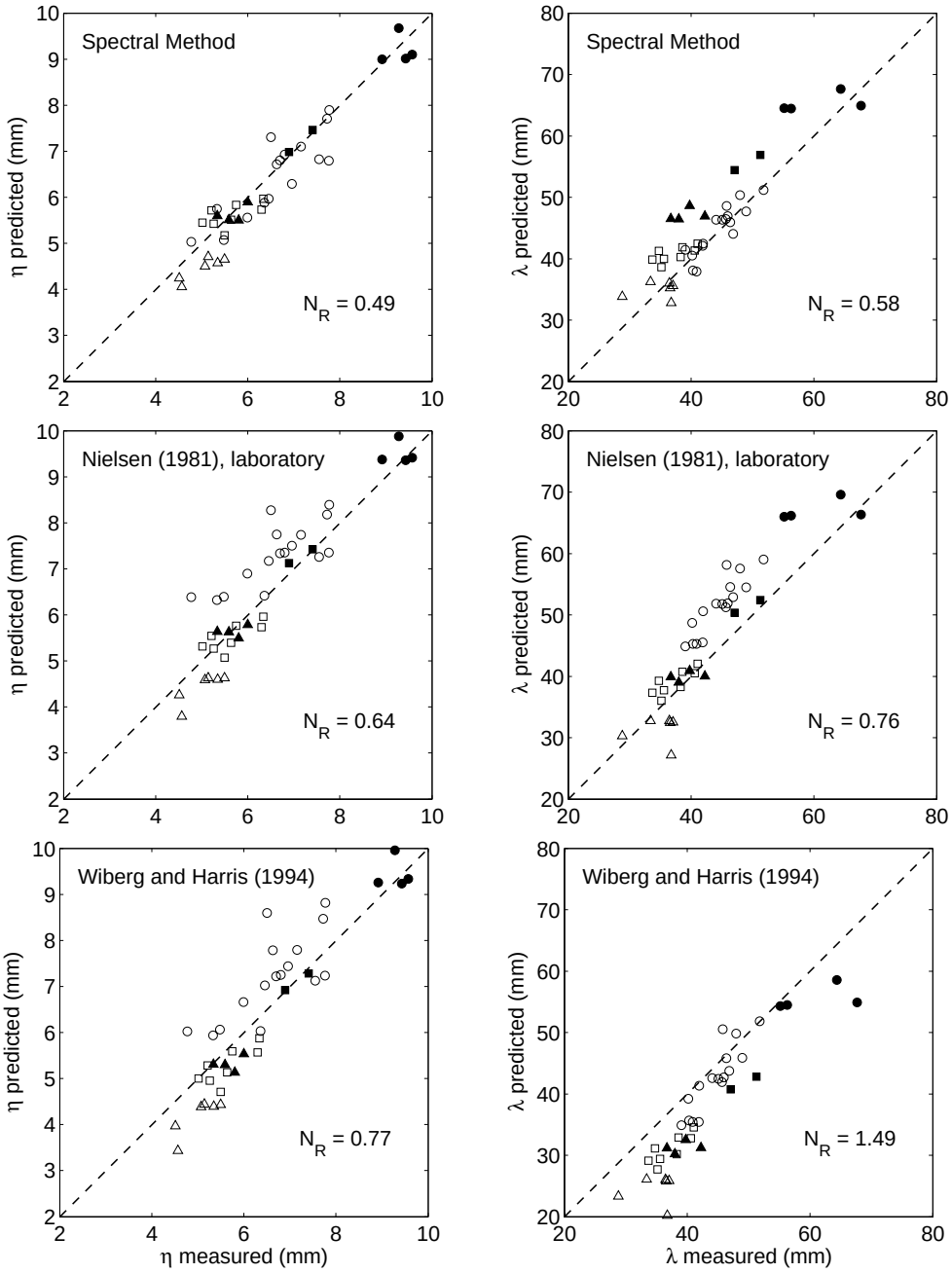

Figure 5.10 Laboratory scale comparison of the spectral method and two other ripple prediction methods with the measured values of the ripple height and the ripple length for the experimental data. The different symbols shapes denote the different frequency conditions used: ○ - 0.8 Hz; □ - 1.0 Hz; △ - 1.2 Hz, while the fill indicates the sediment type: open - 242 μm; filled - 372 μm. N_R is the norm of the normalised residual error from a 1-to-1 agrement shown as the dotted line.

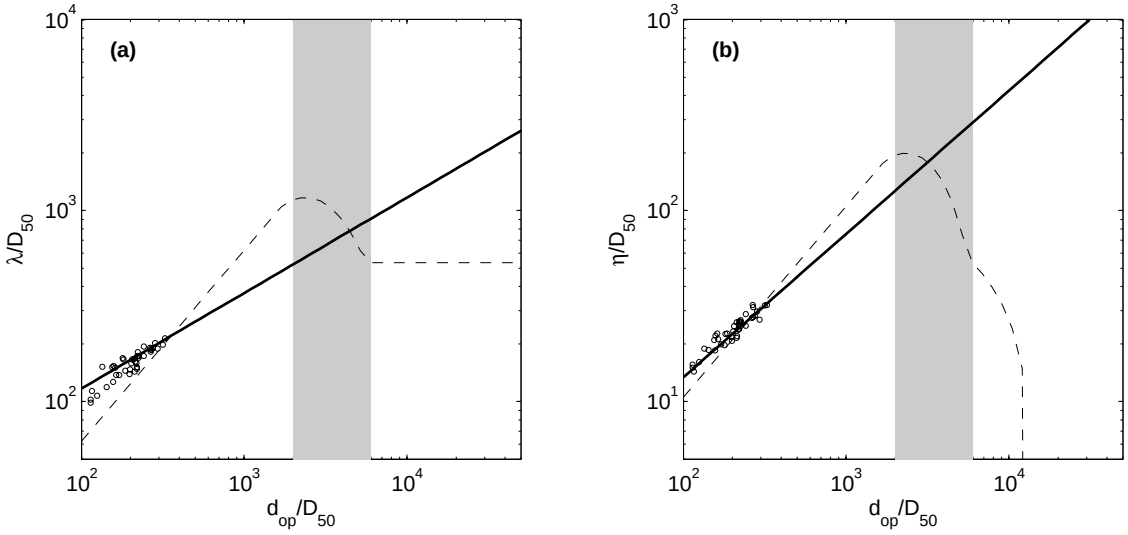

Figure 5.11 Field scale comparison of the spectral method. The estimated (a) normalised ripple length and (b) normalised ripple height plotted against the normalised orbital excursion diameter. The plain line represents the spectral method while the dotted line represents the ripple prediction method of *Wiberg and Harris* [1994]. The circles represent the experimental data set measured as part of this study. Moving left to right across the figure the regions are the orbital, suborbital (shaded) and the anorbital ripple regimes.

vides an easy way to illustrate the generally accepted trends in ripple parameters in this non-dimensional space. A review of *Clifton and Dingler* [1984] and *Wiberg and Harris* [1994] highlights the substantial scatter ripple measurements display about these trends.

In Figure 5.11a the spectral method, in its present form, deviates away from the values predicted by the method of *Wiberg and Harris* [1994] as the normalised orbital diameter is increased. The spectral method fails to simulate the change in slope as the ripple regime changes from orbital to anorbital. In Figure 5.11b the spectral method does show a high level of agreement with the method of *Wiberg and Harris* [1994] in the orbital regime, but once again it fails to simulate the falloff of ripple parameters in the suborbital and anorbital regions. This was to be expected as the method was fitted to a relatively small set of data with a low range.

Table 5.1 presents the five parameters used to fit the method to the experimental data set. These parameters, while applicable for the scale of data measured during this study,

may not be the optimum set of parameters for larger scale ripples. Just as the fitting parameters of the Pierson-Moskowitz water wave spectrum, on which the form of equation 5.9 is based, have different values under different physical conditions so it could be the case that the same is true of the theoretical ripple spectrum. As outlined in Chapter 4, the spectral method is a first step in using any other parameterisation of rippled beds other than the very simple two parameter based methods that have been previously developed. Further research using larger scale measurements needs to be undertaken to refine the fitting parameters of the spectral method.

5.4 Summary and Discussion

This chapter introduced a new method to predict wave formed rippled beds, from flow conditions and sediment properties, in terms of their spectral density function. To use the new spectral parameterisation presented in Chapter 4 to its full potential to characterise and model rippled beds, it is essential that the ripple spectrum can be related back to the flow conditions under which the rippled field formed and to the properties of the sediment bed. Two methods were attempted to develop a functional dependence between the water surface and ripple spectra.

The first method directly compared the two spectra by converting the water surface spectrum into a spatial frequency spectrum. Five spectral parameters were derived from the spectra and used to develop relationships between the two spectra. However, this method failed to produce a reliable functional dependence to predict the ripple spectrum. The failure of this method was disappointing as it was felt that some functional dependance should be evident between the linked spectra. Higher level spectral functions such as the cross spectral density or a transfer function estimate were attempted, but were not successful. Hence, it is a recommendation of this thesis that future work be undertaken on the development of higher level spectral functions to enable the prediction of a given ripple spectrum directly from the water surface spectrum that formed the rippled bed.

The second method used a non-dimensional form of the ripple spectra to develop a functional dependence between the flow and sediment properties and the ripple spectra.

This method worked well and enabled the study to estimate a ripple spectrum given a flow condition and sediment bed properties. The non-dimensional form of the ripple spectrum was developed from the median grain size and the peak orbital excursion diameter. The use of the peak orbital excursion diameter was derived from the peak value in the near bottom velocity spectrum. Historically there has been some debate on how to introduce the randomness and variability of the surface wave field into ripple prediction methods [*Mathisen and Madsen*, 1999; *Traykovski et al.*, 1999]. However, the preliminary ripple prediction method developed in this chapter did not take into consideration the variability of the wave field or sediment bed, but used characteristic values to define these random parameters.

The non-dimensional method was compared with two established ripple prediction methods [*Nielsen*, 1981; *Wiberg and Harris*, 1994] and was found to be able to model small scale ripples with the same degree of accuracy as the more traditional methods. However, based on a comparison of the method against widely accepted trends of ripple parameters at higher ripple scales it was found that the spectral method failed to predict these trends at larger ripple scales. It was concluded that the method was able to be used to predict equilibrium ripple beds at small scales, but at larger scales further research needs to be undertaken on refining the fitting parameters or on the form of the empirical function.

Overall the non-dimensional spectral method worked well over the range of experimental conditions that could be simulated by this study. However, there is little advantage in using equation 5.10 to predict ripple parameters under steady state flow conditions. The main advantage comes when the spectral method is used to model ripples developing with time under changing flow conditions. This method will be presented in the next chapter.

Chapter 6

Ripple Bed Transients

As discussed in Chapter 2, there have been two main approaches employed to account for the temporal variation of rippled beds in shallow shelf seas. These approaches are: moveable bed roughness models (refer to Section 2.2.1); and ripple development or growth models (refer to Section 2.2.2).

Moveable bed roughness models re-calculate the ripple parameters each time step as part of a hydrodynamic modelling simulation based on the flow conditions. As such, the bottom roughness height evolves during the modelling simulation based on the estimated surface wave conditions of the previous time step. A number of authors have developed moveable bed roughness models to account for the highly dynamic nature of wave-formed rippled beds and have incorporated these into flow and sediment transport models [*Grant and Madsen*, 1982; *Graber and Madsen*, 1988; *Tolman*, 1994, 1995; *Ardhuin et al.*, 2001]. *Ardhuin et al.* [2001] indicated that the use of a moveable bed routine enabled a greater degree of agreement between their measured observations and their modelling results to be achieved. However, the main limitation with the current application of moveable bed roughness models is that they do not contain ripple evolution sub-models [*Tolman*, 1995]. This assumes that ripple growth rates are much higher than the rate at which flow conditions change, which effectively means that the rippled field is in constant equilibrium with the surface wave conditions. Based on field observation of ripple dynamics by *Amos et al.* [1988]; *Wheatcroft* [1994]; *Bell and Thorne* [1997]; *Traykovski et al.* [1999]; *Doucette*

Parts of this chapter have been published in the Journal of Geophysical Research, see Appendix B

[2002] and *Moore and Jaffe* [2002], this will generally not be the case.

Ripple growth models attempt to address the failings of the bottom roughness models by developing a functional dependence on ripple parameters with time. These functions contain coefficients that are based on the flow and sediment properties which allows the time a rippled bed takes to come to an equilibrium with the flow conditions to be estimated and taken into account. There have been a number of studies undertaken on the development of growth models for current-formed ripples growing from *flat* bed conditions [e.g., *Coleman and Melville*, 1996; *Nikora and Hicks*, 1997; *Baas*, 1999]. The main focus of these studies were to determine the rate at which the ripples change in fluvial environments. Conversely there has been little work undertaken on determining the rate at which wave-formed rippled beds will evolve due to a change in the surface wave spectra. A limited set of previous laboratory studies have observed and recorded wave-formed ripples growing from *flat* bed conditions [*Marsh et al.*, 1999; *O'Donoghue and Clubb*, 2001; *Faraci and Foti*, 2002] (refer to Section 2.2 for a review of these studies). These studies did not attempt to develop a growth model for wave-formed ripple beds.

The transition of ripples from one equilibrium energy state to another, due to a change in wave direction or energy, has been widely observed in the field [*Amos et al.*, 1988; *Wheatcroft*, 1994; *Drake and Cacchione*, 1989; *Bell and Thorne*, 1997; *Traykovski et al.*, 1999; *Doucette*, 2002; *Moore and Jaffe*, 2002]. How an established ripple bed will evolve due to a change in the flow conditions is an area of ripple dynamics that is poorly understood and to the author's knowledge there have been no studies that have investigated the transition of rippled beds between two equilibrium states.

This chapter contains three main sections which will culminate in the development of a ripple evolution model that will allow ripple parameters starting from a given equilibrium position to be modelled with time. The first section discusses ripple growth in relation to the experimental results measured by this study. Table 3.2 (page 55) list the flow conditions and sediment properties used in the 20 growth tests that were undertaken. Throughout this discussion, specific reference will be made to the example plot presented in Section 3.2.1 (refer to Figure 3.5, page 53) showing ripple growth with time. The sec-

ond section discusses ripple transition mechanisms in relation to the experimental results. These types of measurements have not been previously undertaken in a controlled laboratory environment. Table 3.4 (page 60) list the flow conditions and sediment properties used in the nine transition tests that were undertaken. As with the growth tests, an example plot presented in Section 3.2.3 (refer to Figure 3.7, page 59) will be used to aid in the discussion of ripple transition mechanisms. The third section will present the derivation of the ripple evolution model that has been developed based on the growth and transition experimental tests. The chapter will conclude with a discussion of the two types of ripple transient tests and the evolution model with conclusions highlighted.

6.1 RIPPLED BED GROWTH

To develop a ripple evolution model, the growth of ripples from a no-ripple condition needs to be understood and parameterised. A no-ripple state occurs in nature when there has been an absence of suitable wave conditions to form ripples. Field studies by *Amos et al.* [1988] indicate that benthic organisms will degrade rippled beds to a *flat* bed condition within 4 to 6 hours. However, in general, numerical models start from a no flow condition and are then ramped up as the simulation proceeds. Similarly, parameterisations of rippled beds would also require ramping up from a no-ripple bed condition as the simulation starts. Hence the growth characteristics of rippled beds growing from no-ripple bed conditions are required in the ripple evolution model. This section describes a series of experiments which monitored the growth of rippled beds under the action of an irregular surface wave field as they grew from a no-ripple state. The analysis focusses on the development of the dimensional and non-dimensional ripple spectra with time under a variety of flow and sediment conditions. As noted previously the term for a sediment bed that has no ripples will be referred to in this thesis as a no-ripple condition. This is in preference to calling the bed *flat* as sediment beds are rarely flat, but will always have some level of background roughness.

Section 3.2.1 outlines the experimental method employed to observe ripple beds growing from a no-ripple state. Table 3.2 (refer page 55) lists the experimental growth tests

undertaken while Figure 3.5 (refer page 53) shows an example of a transient data set that was obtained from the ripple growth tests. Note that the Fourier band pass filter discussed in Section 4.2.2 was used to filter the transient ripple profiles prior to any analysis being undertaken.

It can be seen in Figure 3.5 that the rippled bed takes a period of time to initiate ripple formation, but once ripples start to appear on the surface the bed develops quickly. Once the ripples have developed they no longer change and can be considered to have come to a dynamic equilibrium with the flow conditions. Ripples along the bed typically do not form at the same time, but one or two individual ripples will form at a given location in isolation, then other ripples will form spreading out in both the up-wave and down-wave directions. This growth mechanism is shown very clearly in Figure 3.5 with the initial formation of a few isolated ripples which then merge and spread out across the bed. *Faraci and Foti* [2002] also noted this form of growth in their irregular wave tests. The growth mechanism follows the original suggestion of *Bagnold* [1946] that ripples need to pass through the rolling grain preliminary state. Once the sediment at a given location has built up enough by the rolling grain mechanism it starts to disrupt the bottom boundary layer and flow separation occurs with a vortex being shed in the wake of the ripple. The larger velocity associated with the vortex causes sediment to be scoured behind the ripple and hence the ripple grows rapidly. As the flow is oscillating these vortices and the associated turbulence are carried both in the up-wave and down-wave directions. Thus the ripples spread out in both directions from the original perturbation of the sediment surface.

6.1.1 Ripple Spectra Growth

There are a number of ways in which the ripple height and length can be estimated during the preliminary growth stages of the rippled bed. Individual ripples can be chosen and then followed through the time series measuring the height and length of the particular ripple at each time step. *Faraci and Foti* [2002] undertook this method using photographs to determine individual ripple heights and lengths at each time step. For the data shown in Figure 3.5 the first ripple appears at 30 minutes while the total bed does not become fully

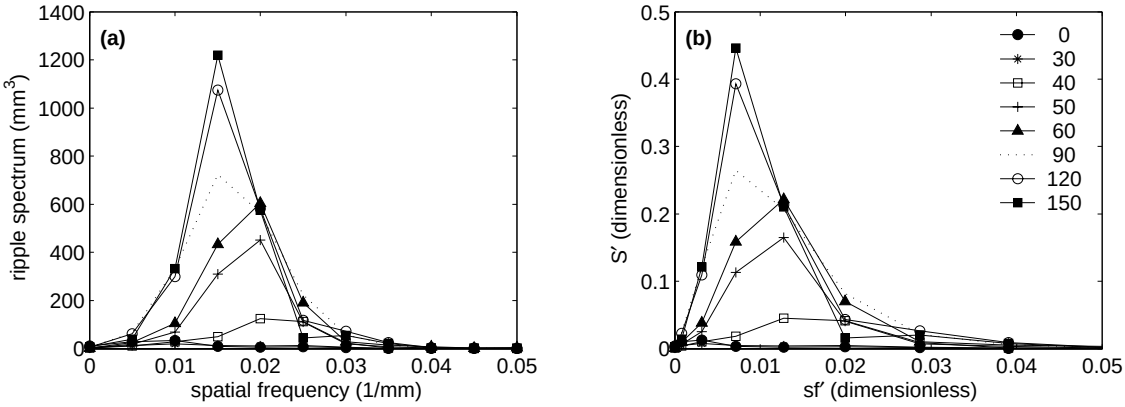

Figure 6.1 Example plot showing typical ripple spectrum growth with time. The two plots are: (a) the dimensional spectra calculated from the sediment surface time series; and (b) the non-dimensional ripple spectrum calculated from the dimensional spectra and the flow and sediment parameters.

rippled until 75 minutes. Hence focussing on a particular ripple form may give an unrealistic picture of the time rippled beds take to develop. A more concise way to describe the growth of rippled beds is to observe the way the ripple spectrum develops with time. This assumes that the rippled bed can be considered as a moving random field of bottom elevations. The developing rippled bed can then be characterised as a whole without bias being given to any particular area of the bed. Figure 6.1 shows the development of both the dimensional and the non-dimensional ripple spectra with time. The non-dimensional scaling that has been used to develop a predictive method for equilibrium wave-formed rippled beds was presented in Section 5.2.1 (refer to equation 5.6, page 103 and equation 5.7, page 104). The data used to produce Figure 6.1 is the same data set as shown in Figure 3.5.

Figure 6.1 illustrates that the growth of the ripple spectrum starts at the higher spatial frequencies and shifts to the lower frequencies as the ripples start to develop. This indicates that the ripples are lengthening as their height is increasing. *Jain and Kennedy* [1974] suggested a mechanism for the evolution of the current-formed ripple spectrum. They suggest that the velocity of sediment ripples along the bed is dependent on the length of the ripples, hence ripples will be dispersive (longer ripples will move faster along the

bed than shorter ripples). Since individual ripples are not able to move through each other, over time all ripples will become larger and more uniform. *Jain and Kennedy* [1974] called this process *"the variance cascade"* as ripples cascade into each other. There is some evidence of this process in the spatial data shown in Figure 3.5. A number of the original smaller ripples are swallowed during the evolution process by adjacent larger ripples. However, this effect is small in the current tests as the ripples only move small distances during the 2.5 hour test period.

As with the spatial ripple data (refer to Figure 3.5) the spectral energy takes approximately 30 minutes to increase above a background level. Once the ripples have started to grow their spectral energy increases steadily until the ripples have reached a dynamic equilibrium with the flow conditions. Observing the spectra will give a good indication of whether the bed has reached equilibrium during a given test. In Figure 6.1 the ripple spectrum is stable after 120 minutes of run time.

6.1.2 Ripple Parameter Growth

As presented in Section 4.1.2, a coefficient of variation (equation 4.1, page 70) can be calculated from the ripple surface using a zero up-crossing technique [*Goda*, 2000]. It is interesting to see how the coefficient of variation for both the ripple height and the ripple length changes with time as the ripple surface grows from a no ripple condition. Figure 6.2 presents the coefficient of variation calculated at each 5 minute time step for the ripple surface shown in Figure 3.5.

The coefficient of variation for the ripple height and the ripple length show two different trends. The ripple height variation starts off at a medium level increases to a very high value as the rippled bed starts to form then slowly decreases as the rippled bed moves towards an equilibrium state with the flow conditions. The variation of the ripple length starts at the same medium value as did the height variation, however, it does not increase as did the height variation, but stays at a constant value for a period then decreases steadily until equilibrium is once more achieved. This indicates that the ripple height displays a greater variation as the rippled field forms than does the ripple length. This trend can

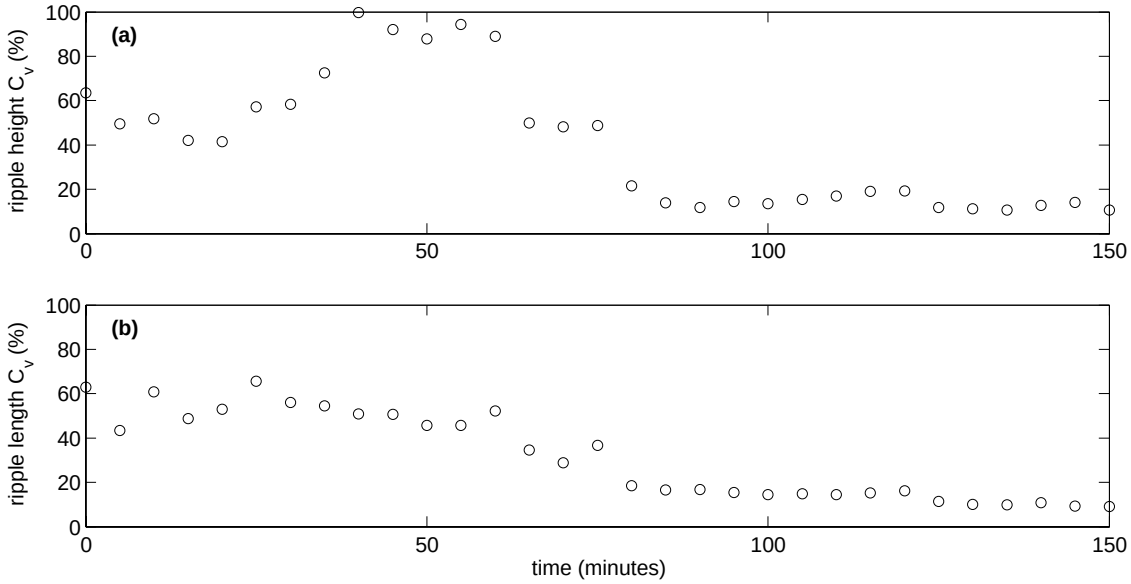

Figure 6.2 Change of the coefficient of variation with time for a growing ripple bed, where: (a) shows the change in the coefficient of variation for the ripples height; (b) shows the change in the coefficient of variation for the ripples length.

also be seen in the raw ripple data shown in Figure 3.5. As the ripple field develops the length increases more uniformly across the bed while the ripple height increases quickly in patches as a ripple starts to shed a vortex (i.e. the ripple moves from a rolling grain ripple to a vortex ripple). Hence, the high value of the ripple variation indicates that some ripples are still in the rolling grain phase while others have already achieved the vortex stage.

The ripple spectrum can be parameterised using previously derived water surface spectrum parameters as shown in Section 4.2.4. These two parameters are the spectral width factor (equation 4.3, page 86) and the spectral peakedness parameter (equation 4.5, page 86). As with the coefficient of variation it is useful to observe how these parameters change with time as the ripple spectrum is developing from a no-ripple condition. Figure 6.3 presents the spectral width factor and the spectral peakedness parameter calculated at each 5 minute time step for the ripple surface shown in Figure 3.5.

The interesting point about Figure 6.3 is the rapid increase in the spectral peakedness parameter between the times of 35 and 40 minutes. The value of the peakedness parameter

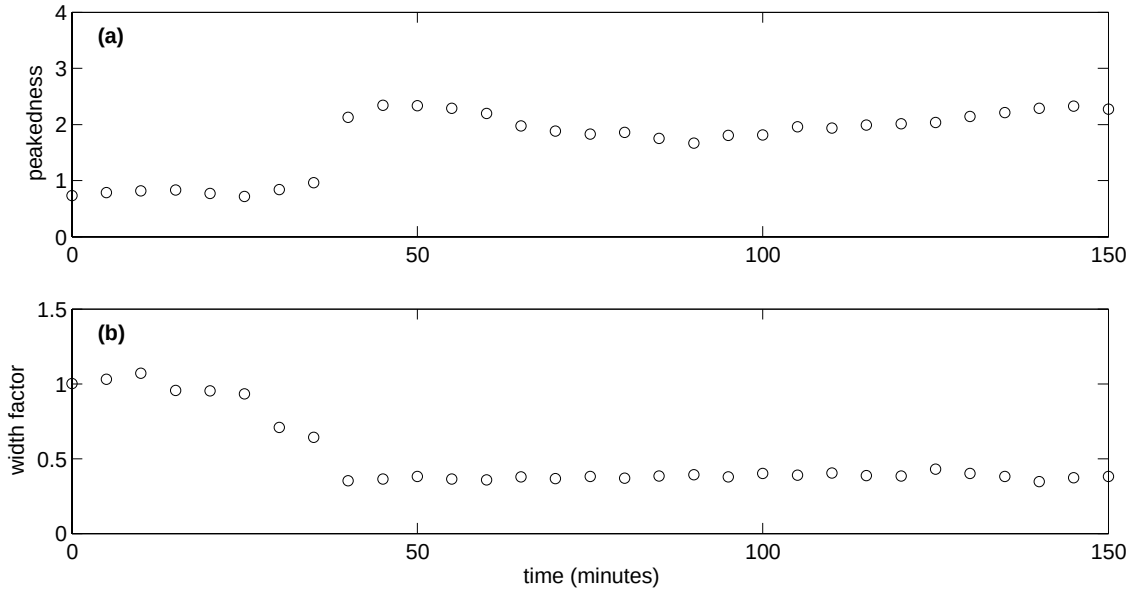

Figure 6.3 Change of the spectral parameters with time for a growing ripple bed where: (a) shows the change in the spectral peakedness parameter and (b) shows the change in the spectral width factor.

doubles from a value of 1 to a value of 2 in the space of 5 minutes. This jump between the times of 40 and 50 minutes is also seen in Figure 6.1 with a sharp increase in the spectral energy of the rippled bed. The spectral width factor shown in Figure 6.3 indicates an opposite trend compared with the spectral peakedness parameter. It starts at a high value then decreases steadily until a time of 40 minutes then is constant for the rest of the test. However, as with the peakedness parameter, the greatest change is between the times of 35 and 40 minutes.

As discussed in Section 5.3, a characteristic ripple height and length can be calculated from the ripple spectrum using equations 5.11 (page 111) and 5.12 (page 112). This was done so that a comparison could be made between the ripple spectrum prediction method and the more traditional ripple prediction relationships. These two equations also allow a time series to be plotted showing the growth of the more traditional ripple parameters with time. Figure 6.4 presents these relationships. A measure of the ripple steepness was calculated from the characteristic ripple parameters by simply taking the ratio of the ripple height over the ripple length. These estimates of ripple height and length are based

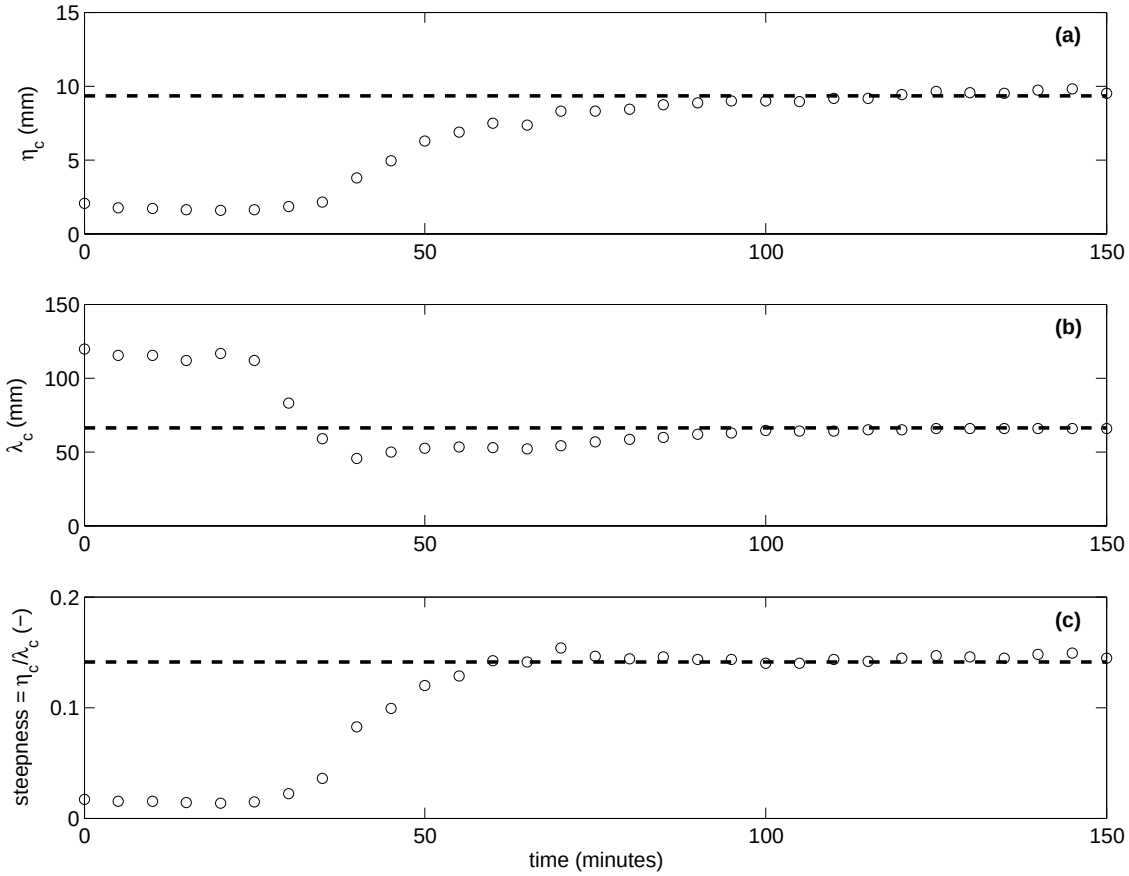

Figure 6.4 Change of the traditional parameters with time for a growing ripple bed, where: (a) is the characteristic ripple height; (b) is the characteristic ripple length and (c) is the ripple steepness. The bold dotted lines represents the equilibrium values predicted from equation 5.10.

on the bed as a whole and do not map the growth of individual ripples as done previously [see *Faraci and Foti*, 2002]. As with Figures 3.5 and 6.1, the data used to form Figure 6.4 came from test G05 shown in Table 3.2.

Figure 6.4 provides another way to view the ripple bed changing with time. The ripple length in Figure 6.4 starts off at a very high level, falls to a minimum and then rises again to an equilibrium level. The background spectral energy of the bed, although very small in energy, has a peak spatial frequency (length) which is much smaller than the spatial frequencies associated with ripple forms. As the ripples grow this background level of roughness is washed out and replaced with small ripples, which in turn lengthen into

equilibrium ripples. Hence the peak spatial frequency drops to a minimum from some background level then grows again. The ripple steepness is calculated here as the ratio of ripple height over the ripple length. Hence the unrealistic longer lengths calculated during the start of the test do not affect the steepness, as the ripple height is small during this period.

In Section 5.2.2 an empirical prediction method was derived for the equilibrium ripple spectrum based on the flow conditions and sediment bed properties (refer to equation 5.10, page 109) to which the rippled bed had reached an equilibrium state. The bold dotted lines, shown in Figure 6.4, represent the equilibrium values of the ripple height, length and steepness calculated from the theoretical spectrum by the use of equations 5.10, 5.11 and 5.12. As shown in Figure 6.4, there is a very good agreement between ripple parameters predicted by equation 5.10 and the characteristic ripple parameters estimated from the ripple spectrum at the end of the simulation, but poor agreement at the start of the simulation. The same surface wave conditions were used throughout this test. This highlights an important aspect of this study: while ripples are developing under a given flow condition they can not be adequately predicted by empirical methods which have been derived from equilibrium rippled beds.

6.2 RIPPLED BED TRANSITION

As outlined above, a number of authors have investigated the growth of rippled beds under the action of waves from a no-ripple condition. However, no study has been found that has parameterised the transition of rippled beds from one equilibrium state to another. The transition of ripples due to a change in wave direction or energy has been widely observed under field conditions [*Amos et al.*, 1988; *Wheatcroft*, 1994; *Drake and Cacchione*, 1989; *Bell and Thorne*, 1997; *Traykovski et al.*, 1999; *Doucette*, 2002; *Moore and Jaffe*, 2002]. How an established ripple bed will change under flow conditions that are no longer in equilibrium with the bed is important in understanding the mechanism of ripple evolution. The time a rippled bed will take to reach equilibrium with the new flow conditions is likely to be a function of the flow energy available and the energy that is required to move the

individual sand grains [*Wiberg and Smith*, 1985]. Understanding both the mechanism of change and the time a rippled bed will take to reach a new equilibrium is required to develop a ripple evolution model. This section presents a series of experimental results used to investigate the changes rippled beds undergo when in the process of actively changing from one equilibrium state to another.

Section 3.2.3, outlines the experimental method employed to observe ripple beds in transition between two equilibrium states. Table 3.4 (refer page 60) lists the experimental transition tests undertaken while Figure 3.7 (refer page 59) shows an example of the transient data that were obtained from the ripple transition tests. As was the case for the growth tests the Fourier band pass filter discussed in Section 4.2.2 was used to filter the transient ripple profiles prior to any analysis being undertaken.

Figure 3.7 presents two examples of rippled beds actively evolving under a changed surface wave spectrum. Figure 3.7a shows a rippled bed in transition from a higher energy state back to a lower energy state. The high energy state represents a bed formed under the experimental conditions listed in Table 3.2 as G05 while the low energy state is listed as T03 in Table 3.4. Figure 3.7b shows the opposite with the bed in transition from a lower state up to a higher energy state. The low energy state was formed by test T03 in Table 3.4 while the high energy state is listed as T07 in Table 3.4. The two examples were chosen because they were both generated using the same sediment diameter with similar surface wave heights.

The first thing that can be noticed in Figure 3.7 is the change in ripple length between the equilibrium states. In Figure 3.7a the number of ripples in the 400 mm section grows from 6 to 10 in the two hour period, while in Figure 3.7b the number ripples reduces from 10 to 7 during the transition. This change in ripple length is brought about by a change in the surface wave frequency used in each of experimental tests: a change from 0.8 to 1.2 Hz in Figure 3.7a and a change from 1.2 to 0.8 Hz in Figure 3.7b. This change in the surface wave frequency will correspond to a change in the length of the peak orbital excursion diameter. Small scale wave-formed ripples such as these will generally scale to the orbital excursion diameter [*Nielsen*, 1981].

The process by which this occurs is slightly different in each case. There is only finite space on the bed and the bed adjusts to this space by either creating new ripples or "swallowing" older ripples. In Figure 3.7a the mechanism of length reduction is one in which new ripples form between the remnant ripples. The remnant ripples first become very steep and flat bottomed with their sides being eroded. New ripples start to form in the inter-ripple spacings (troughs). This is shown at a test time of 30 minutes with an exact doubling of the number of ripples present on the surface (from 6 to 12 at time of 30 minutes). During this time there is an associated reduction in the ripple height as the sediment is redistributed between ripples. After this doubling the ripples then adjust to the flow conditions by growing slightly. This is achieved on the bed by a number of the newer ripples being "swallowed" by their neighbouring ripple. In Figure 3.7b, however, the ripples will start to lengthen as they attempt to reach an equilibrium with the new orbital excursion diameter. This lengthening process causes a number of ripples to be once again swallowed by their neighbouring ripple. As the ripples are swallowed the surviving ripples grow in height as the sediment is once more redistributed across the bed. Figure 3 in *Marsh et al.* [1999] also shows this process where a ripple is swallowed by an adjacent ripple as the bed is adjusting to the flow conditions.

Another observation gained from Figure 3.7 is the speed at which the ripples move. Figure 3.7 shows the ripples moved between 25 and 100 mm in the two hour period. As the ripple length changes there is also a slight change in their speed shown by the slope of the ripple crest line between each plot, hence the suggestion by *Jain and Kennedy* [1974] that ripples are dispersive is supported.

6.2.1 Ripple Spectra Transition

As with the ripple growth data, the ripple transition data can be viewed as a change in the spectral energy of the bed with time. Figures 6.5a and 6.5b show the ripple energy decreasing and were calculated from the data set shown by Figure 3.7a, while Figures 6.5c and 6.5d show the increase in the ripple energy and were calculated from the data shown in Figure 3.7b. As with Figure 6.1 the left hand side shows the dimensional spectra

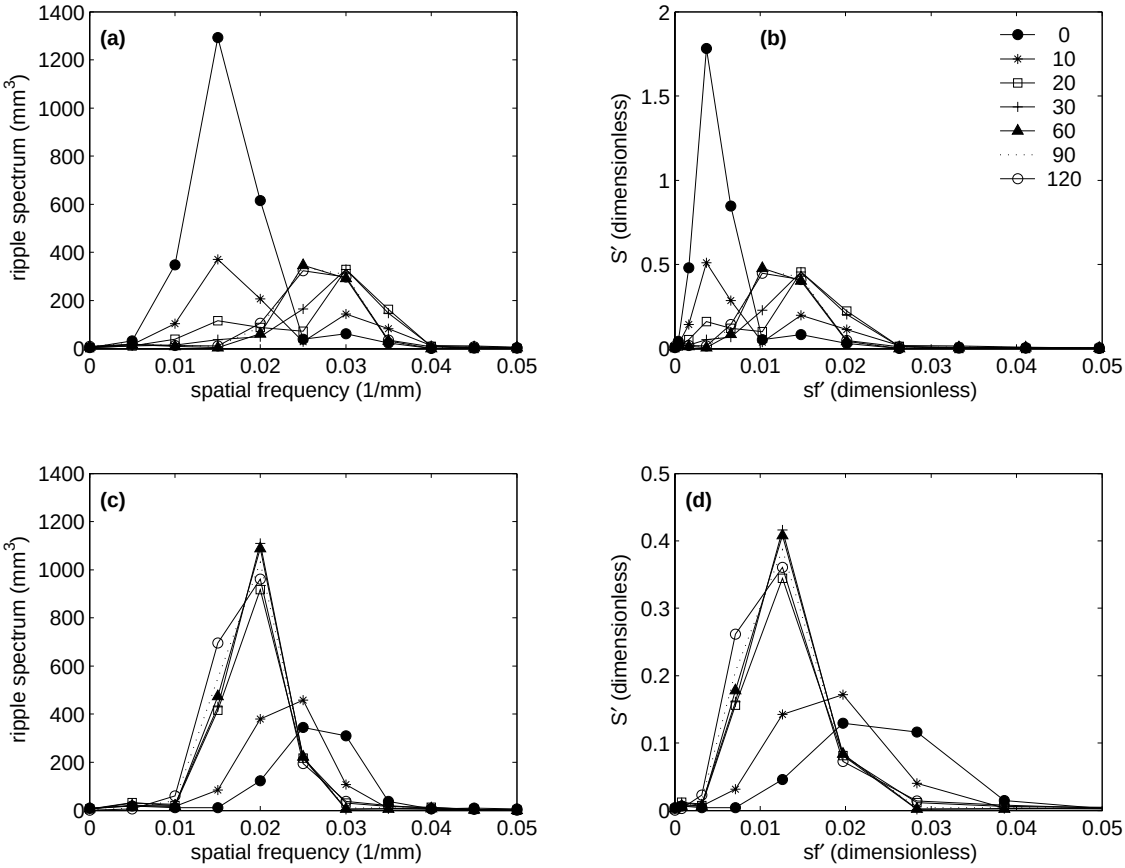

Figure 6.5 Example plots showing ripple spectra transition under the action of surface waves that are out of equilibrium with the rippled bed where: (a) the dimensional and (b) non-dimensional spectrum decreasing due to a lower wave energy state; (c) the dimensional and (d) non-dimensional spectrum increasing due to a higher wave energy state.

calculated from the bed while the right subplots show the non-dimensional spectra scaled by equations 5.6 and 5.7.

The same trends that were evident in Figure 3.7 can also be seen in Figure 6.5. Figures 6.5a and 6.5b show the reduction of ripple energy due to a change in the surface wave spectra. The peak spectral energy has dropped with a corresponding increase in the peak spatial frequency of the bed. This relates to the ripples getting smaller and shorter. The peak spatial frequency increases quickly and by 30 minutes it has doubled from a value of 0.015 to a value of 0.03. This was also evident in Figure 3.7a with a doubling in the number of ripple forms present on the surface by a time of 30 minutes. The bed then

further adjusts to the flow conditions with the ripples slightly increasing their length. This is shown in Figures 6.5a as a slight decrease in the peak spatial frequency to a final value of approximately 0.025. Figures 6.5a and 6.5b also show that the total area under the spectral curve has decreased, which represents an overall decrease in the potential energy of the bed. Figures 6.5c and 6.5d show an increase in the spectral energy of the bed due to a change in the surface wave field. As can be seen the bed has increased its peak spectral energy and there has been a decrease in the peak spatial frequency. This corresponds to an overall increase in the rippled beds height and length. The area under the spectral curve has also increased which suggests an overall increase in the potential energy of the bed. The transition to a higher energy state shown in Figures 6.5c and 6.5d is much smoother than the transition to a lower energy state, shown in Figures 6.5a and 6.5b. The ripples decreasing continuously, in Figures 6.7c and 6.7d, until they achieve their equilibrium peak spatial frequency. This is compared to Figures 6.7a and 6.7b which jump to a new energy level. However, the time for both example beds to achieve near equilibrium conditions is similar and was achieved after a run time of some 60 minutes.

6.2.2 Ripple Parameter Transition

Section 4.1.2 presents the method to calculate the coefficient of variation (equation 4.1, page 70) from a rippled surface using the zero up-crossing technique defined by *Goda* [2000]. Figure 6.6 presents the coefficient of variation calculated at each 5 minute time step for the ripple surfaces shown in Figure 3.7. In Figure 6.6 the open squares represent a decreasing ripple bed (refer to Figure 3.7a), while the filled circles represent an increasing rippled bed (refer to Figure 3.7b).

As can be seen in Figure 6.6, there is an approximate doubling of the coefficient of variation, from 20% to 40% for both parameters (the ripple height and length) as the ripples are in the process of actively changing from one equilibrium state to the other. However, once the bed has reached equilibrium with the flow conditions the coefficient of variation stays at a near constant level for the rest of the experimental period. Unfortunately the coefficient of variation provides little insight into the transition mechanisms

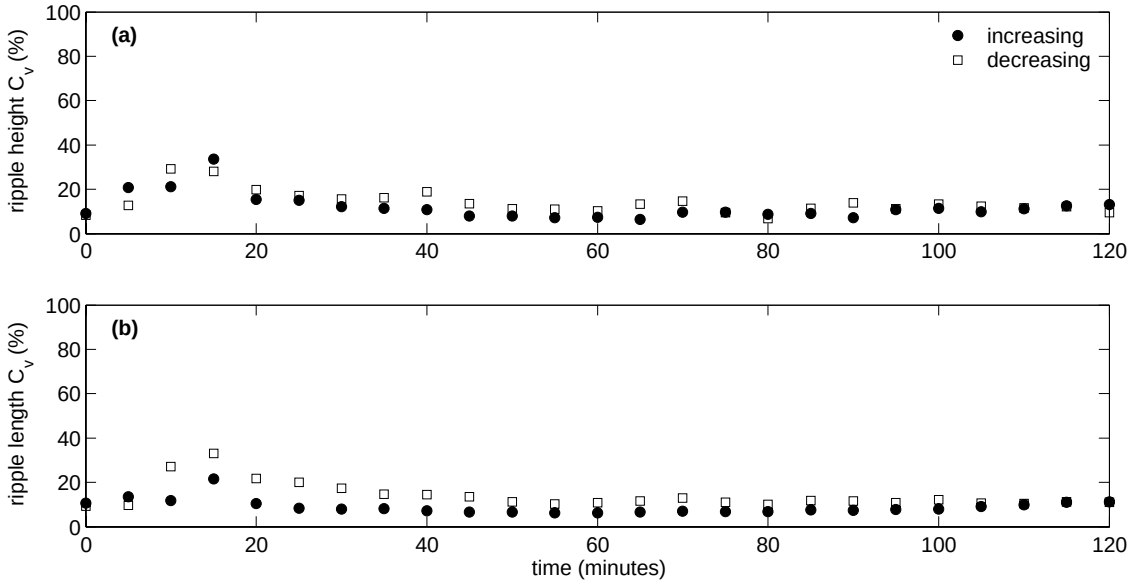

Figure 6.6 Change of the coefficient of variation with time for an evolving ripple bed, where: (a) shows the change in the coefficient of variation for the ripples height; (b) shows the change in the coefficient of variation for the ripples length. The two series show a decreasing bed (refer to Figure 3.7a) and an increasing bed (refer to Figure 3.7b).

that the rippled bed undergoes as it is moving between equilibrium states.

As was done in Section 6.1.2 for the growing ripple bed, the ripple spectrum can be parameterised using the spectral width factor (equation 4.3, page 86) and the spectral peakedness parameter (equation 4.5, page 86). It is useful to observe how these parameters change with time as the ripple spectrum is evolving between equilibrium states. Figure 6.7 presents the spectral width factor and the spectral peakedness parameter calculated at each 5 minute time step for the ripple surface shown in Figure 3.7.

There is little change shown in Figure 6.7 with both spectral parameters remaining at an approximately constant level throughout the 2 hour tests. However, there is a slight decrease in the spectral peakedness parameter and a slight increase in the spectral width factor as the test begins. This was probably due to the shift in the ripple spectra which occurred as flow conditions changed. The interesting point in Figure 6.7, however, is the decreasing trend in the spectral peakedness parameter as the test increases. This was not expected as it was thought that the ripple spectrum should have attained an equilibrium

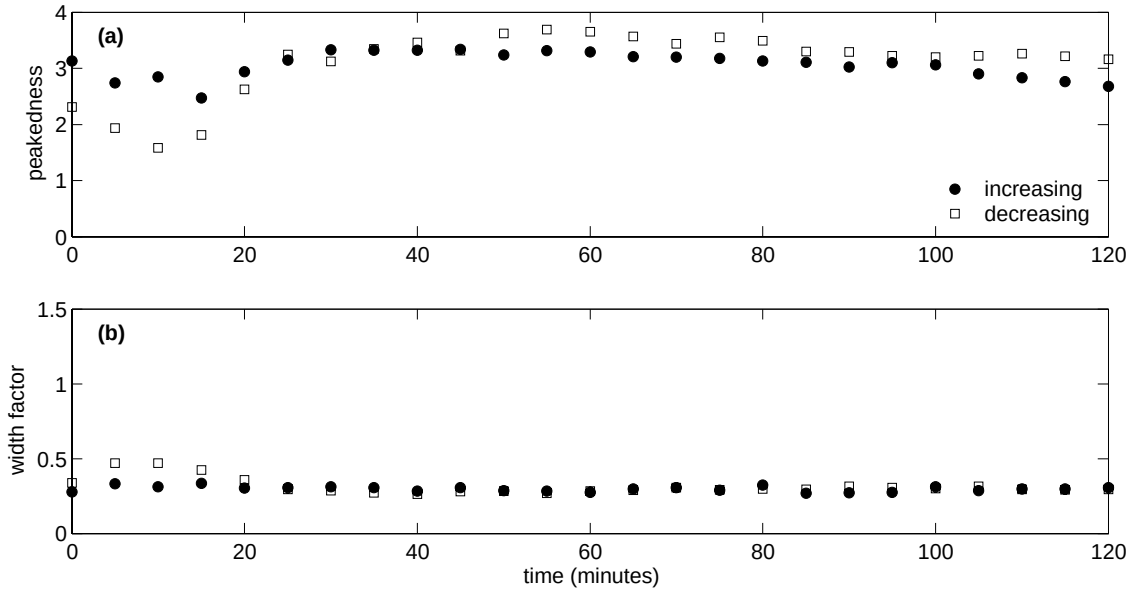

Figure 6.7 Change of the spectral parameters with time for an evolving ripple bed where: (a) shows the change in the spectral peakedness parameter and (b) shows the change in the spectral width factor. The two series show a decreasing bed (refer to Figure 3.7a) and an increasing bed (refer to Figure 3.7b).

shape and not changed further. This unexpected trend is also evident in Figures 6.5c and 6.5d with the bed attaining its highest value at a time of 60 minutes after which the spectral energy reduces and moves slightly towards a lower spatial frequency.

Figure 6.8 presents the characteristic ripple height and length which are calculated from the ripple spectra using equations 5.11 and 5.12. As with Figure 6.4 the ripple steepness is calculated as a simple ratio of the characteristic ripple height over the length in this figure.

Figure 6.8 shows the same trends as did Figure 3.7 and the other figures presented in this section. The change in ripple height for both situations is smooth from an original value to their new equilibrium value. The change in ripple length for the decreasing ripple bed is much more sudden than the corresponding lengthing of the increasing rippled bed. An interesting point in Figure 6.8 is the change in ripple steepness during the transition period. The ripple steepness is generally constant when the rippled bed is in an equilibrium state. However, as the ripples are in transition from one equilibrium state to

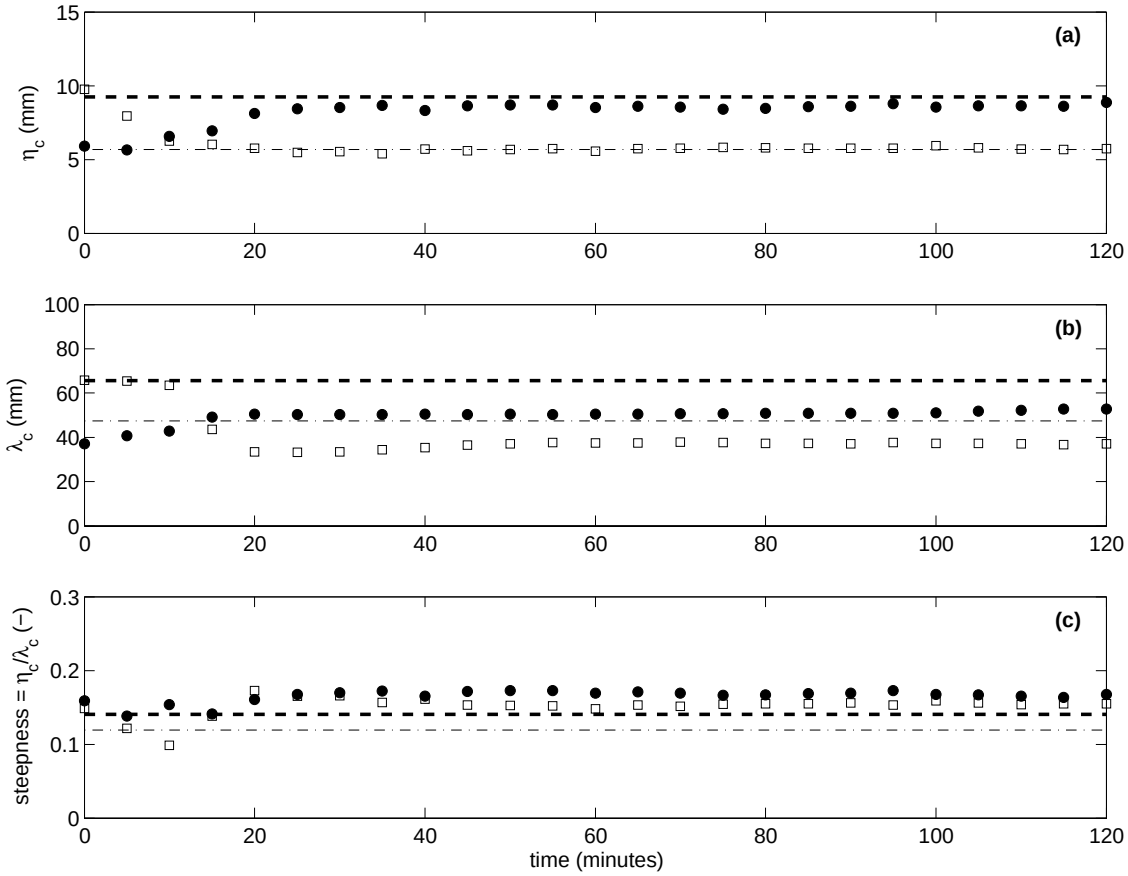

Figure 6.8 Change of the traditional parameters with time for an evolving ripple bed, where: (a) is the characteristic ripple height; (b) is the characteristic ripple length and (c) is the ripple steepness. The two series show a decreasing bed (light open series) and an increasing bed (bold filled series). The dotted lines represents the equilibrium values predicted from equation 5.10.

another there is a corresponding drop in the ripple steepness. This has implications for the modelling of bottom roughness as the roughness height due to ripple forms is generally assumed to be directly proportional to the ripple steepness [*Grant and Madsen*, 1982; *Swart*, 1974; *Raudkivi*, 1988; *Nielsen*, 1992] (refer to Section 2.2.1). Since under real field waves rippled beds may never attain equilibrium [*Traykovski et al.*, 1999] current moveable bed models could be overestimating the value of the bottom roughness height.

The dashed lines in Figure 6.8 represent the equilibrium values determined by applying equations 5.11 and 5.12 to the theoretical ripple spectrum derived in Section 5.2.2

(equation 5.10) using the flow and sediment conditions. As can be seen, there is very good agreement between the estimated and experimental ripple heights of the two tests in Figure 6.8a, but the ripple length is overestimated by approximately 10 mm for both tests shown in Figure 6.8b. As was seen in Figure 6.4 the method fails to predict the ripple parameters at the start of the simulation. The same surface wave conditions were used throughout this test and once again this shows that while rippled beds are actively changing they cannot be adequately predicted by empirical methods which have been derived from equilibrium rippled beds.

6.3 RIPPLED BED EVOLUTION MODEL

The development of a ripple evolution sub-model as part of a general moveable bottom roughness model requires that not only the growth of rippled beds from a no-ripple condition be parameterised, as has be done previously [*Nikora and Hicks*, 1997; *Baas*, 1999], but a more generalised approach be taken which will incorporate the transient nature of ripples between any two equilibrium states. This section develops a method in which the rate of change of the equilibrium spectrum given any two starting energy conditions can be estimated from the flow and sediment parameters.

Studies have been undertaken on the growth of current-formed rippled beds from *flat* bed conditions which have developed a functional dependence of this growth with time [*Nikora and Hicks*, 1997; *Baas*, 1999]. These functions have been based on the growth of ripples and, as such, do not take into account the situation presented in Figures 3.7a in which the overall energy of the rippled bed is reduced due to flow conditions. The formation mechanism of the two species of sediment ripples (current-formed and wave-formed) are very different so one would expect that the behaviour of these two species under changing flow conditions would also be different.

The ripple transition is driven by the ratio of the fluid energy which acts to move the sediment grains over the ability of the sediment grains to resist movement [*Wiberg and Smith*, 1985]. Previous studies that have developed expressions for equilibrium ripples have used non-dimensional ratios loosely based on this observation, for example:

the Mobility number, *Nielsen* [1981]; the period parameter, *Mogridge et al.* [1994]; and the ratio of the orbital excursion diameter over the sediment grain diameter *Wiberg and Harris* [1994]. There is a finite limit to the final potential energy level a rippled bed can achieve due to there being a finite energy level of the ratio discussed above. Based on the observations of rippled beds undertaken by this study, it has been determined that rippled beds display two stages of development as they are in the process of evolving to a new equilibrium state, with a point of inflection in the growth curve located between the two stages. For example as the ripples are growing from a no-ripple bed condition the first stage is characterised by the transition rate being proportional to the size of ripples present, while during the second stage the opposite is true, with the transition rate being inversely proportional to the size of ripples on the bed.

In Section 2.2.2, a number of ripple development or growth models were presented which derived a functional dependence for the development of current-formed ripples growing from a no-ripple condition. Figure 2.3 (page 31) presents a comparison of these methods. As discussed, only two of the relationships, those of *Shuliak* [1971] and *Baas* [1999], seem to provide a reasonable functional dependence, in that they predicted equilibrium values at times greater than the equilibrium time. Based on the wave-formed ripple growth tests undertaken by this study, these relationships fail to predict the change of growth rate (inflection point) rippled beds display as they start to grow from a no-ripple condition. Another major problem in using the previous ripple growth relationships is that they cannot be used to predict the situations shown in Figure 3.7 where an established ripple bed is evolving to a new equilibrium state due to a change in the flow conditions.

The observed growth of wave-formed rippled beds measured as part of this research and discussed above has been widely described in other areas of science. This type of non-linear growth is know as the Logistic or Verhulst (1804-1849) Growth Law. The Logistic non-linear differential equation has the form:

$$\frac{dE}{dt} = \alpha E(E_f - E) \tag{6.1}$$

where E is the non-dimensional spectral energy level of the bed, t is the time (minutes), α is the evolution rate (1/minutes) and E_f is the new equilibrium non-dimensional spectral

energy level of the bed. The non-dimensional energy of the bed is defined as:

$$E = \int_{f_{s1}}^{f_{s2}} S'(f'_s)\, df'_s \tag{6.2}$$

From equation 6.1 the rate at which rippled beds evolve can be thought of as a balance between the processes which act to build up the bed and the processes which act to flatten the bed. As the rippled bed is increasing in energy the factors which influence the growth of the rippled bed dominate over the processes that will cause the bed to flatten until equilibrium is reached and the two factors once again balance. Conversely as the rippled bed is decreasing in energy the processes which act to flatten the bed dominate over the growth processes until a new state of equilibrium is reached. The general solution to equation 6.1 is:

$$E = \frac{E_f E_0}{E_0 + (E_f - E_0)\exp(-\alpha E_f t)} \tag{6.3}$$

where E_0 is the starting non-dimensional spectral energy of the bed. Equation 6.3 has three fitting parameters: the starting and equilibrium spectral energy levels of the bed and the evolution rate. Figure 6.9 shows equation 6.3 fitted to the three example beds discussed as part of the previous two sections and presented in Figures 3.5 and 3.7. The three subplots in Figure 6.9 show equation 6.3 applied in three different situations using different values of E_f, E_o and α. These beds represent a bed evolving from a no-ripple condition to an equilibrium bed, a bed evolving from a higher equilibrium state to a lower one, and a bed evolving from a lower equilibrium state up to a higher one.

As can be seen in Figure 6.9, equation 6.3 fits the experimental data in the three situations very well with correlation coefficients greater than 0.8 for all cases. The horizontal dotted lines shown Figure 6.9 are the equilibrium values of the non-dimensional spectral energy as predicted by equation 5.9. The agreement between the measured and predicted final equilibrium values illustrates that equation 5.9 provides an effective method to predetermine the value of the equilibrium spectrum at times greater than the time it takes the bed to reach equilibrium with the flow conditions.

From equation 6.3 an estimate of the time a rippled bed takes to reach equilibrium can be derived. Based on a value suggested by *Baas* [1999] equilibrium was determined to

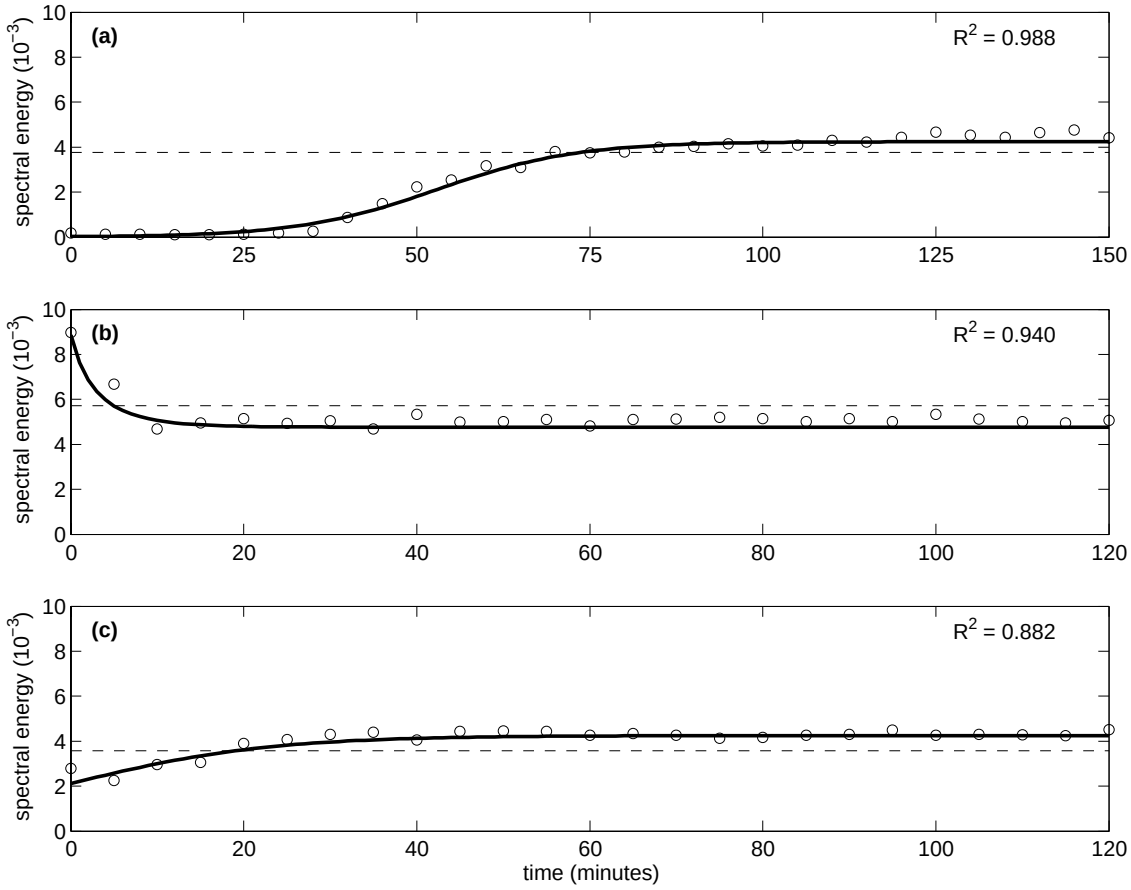

Figure 6.9 The growth of non-dimensional spectral energy with time, where: (a) is the data set shown in Figure 3.5; (b) is the data shown in Figure 3.7a and (c) is the data set shown in Figure 3.7b. The bold line shows equation 6.3 fitted to the data set while the R^2 value is the correlation coefficient of the fit. The dotted lines are the empirically derived equilibrium values (refer to equation 5.9).

have been reached when the energy level of the bed had reached 99% of its equilibrium value. Setting the left hand side of equation 6.3 to equal $0.99E_f$ and solving the equation for time gives:

$$t_e = \frac{-1}{\alpha E_f} \ln \left[\frac{0.01E_0}{0.99(E_f - E_0)} \right] \tag{6.4}$$

where t_e is the equilibrium time in minutes. The time a rippled bed takes to reach equilibrium will not only be a function of the evolution rate, but also of the initial and final conditions of the bed.

Table 6.1 shows the results of fitting equation 6.3 to all the data sets presented in Tables 3.2 (page 55) and 3.4 (page 60), including how the fit correlated with the data set and the time to reach equilibrium. Note that flow and sediment parameters for the tests starting with "G" (growth) are listed in Table 3.2 while those starting with "T" (transition) are listed in Table 3.4. In Table 6.1, all 29 tests fit equation 6.3 well with R^2 values ranging from 0.990 down to 0.588. The growth tests fitted equation 6.3 slightly better than did the transition tests which overall had lower R^2 values. The time for the bed to reach equilibrium calculated via equation 6.4 is also presented in Table 6.1. These times range anywhere from 12 minutes (T04) to 2680 minutes (G20). Test G20 was undertaken with deeper water and very low surface wave conditions and did not form a stable ripple bed during the test time. However, it is included here to show that the method will adequately model the ripple bed as long as there is a change in ripple conditions between the start and finish of the experimental test. The fact that a number of rippled beds, formed under lower flow conditions, did not achieve equilibrium with the flow conditions during the 2.5 hour growth and 2 hour transition tests was also discussed in section 5.2.2 in relation to the development of the non-dimensional form.

The main objective of this research is to enable the temporal changes that a rippled bed undergoes to be modelled. It is then important to be able to estimate the evolution rate from flow conditions and sediment properties. From the values listed in Tables 3.2, 3.4 and 6.1 functional relationships among six of the more widely used non-dimensional numbers and the evolution rate (α) can be examined.

Figure 6.10 presents the linear-linear relationships between the evolution rate and the six non-dimensional numbers listed in Tables 3.2 and 3.4. In this figure the filled circles represent growth tests (refer to Table 3.2) while the open squares represent transition tests (refer to Table 3.4). The bold line is the least squares straight line fit, while the dotted lines indicate the 95% confidence intervals of the straight line fit.

There is appreciable scatter in the data sets presented in Figure 6.10, this scatter is illustrated by the 95% confidence limits of the straight line fits in each subplot. None of the non-dimensional numbers plotted in Figure 6.10 provided a conclusive method to

Table 6.1 Summary of values obtain from fitting equation 6.3 to the data sets.

Experimental	Fitting Parameters			Regression	Equilibrium
Test ID	E_0	E_f	α	R^2	Time
	–	–	$mins^{-1}$	–	$mins$
G01	0.0004	0.0054	6.966	0.980	191.8
G02	0.0001	0.0032	90.116	0.923	30.3
G03	0.0005	0.0040	23.320	0.959	70.0
G04	0.0002	0.0042	36.977	0.989	50.4
G05	0.0000	0.0044	22.993	0.988	98.8
G06	0.0007	0.0043	34.848	0.936	41.5
G07	0.0001	0.0047	22.505	0.976	81.1
G08	0.0001	0.0045	45.676	0.985	42.3
G09	0.0001	0.0046	18.147	0.986	97.2
G10	0.0001	0.0037	47.325	0.977	46.8
G11	0.0002	0.0038	21.363	0.984	96.8
G12	0.0003	0.0051	15.764	0.990	90.7
G13	0.0037	0.0050	5.124	0.832	137.2
G14	0.0004	0.0045	36.185	0.962	42.0
G15	0.0003	0.0052	12.349	0.984	116.5
G16	0.0004	0.0044	9.279	0.953	166.8
G17	0.0003	0.0041	18.697	0.982	93.1
G18	0.0000	0.0059	9.698	0.981	230.7
G19	0.0003	0.0034	34.683	0.954	58.7
G20	0.0007	0.5856	0.007	0.813	2677.5
T01	0.0072	0.0042	56.478	0.588	15.7
T02	0.0100	0.0052	1.932	0.981	384.3
T03	0.0077	0.0042	49.432	0.940	18.6
T04	0.0068	0.0036	85.079	0.728	12.4
T05	0.0032	0.0051	7.282	0.911	108.9
T06	0.0025	0.0050	4.582	0.893	199.7
T07	0.0022	0.0043	20.233	0.882	52.6
T08	0.0025	0.0043	21.410	0.906	45.8
T09	0.0007	0.0047	21.235	0.989	64.1

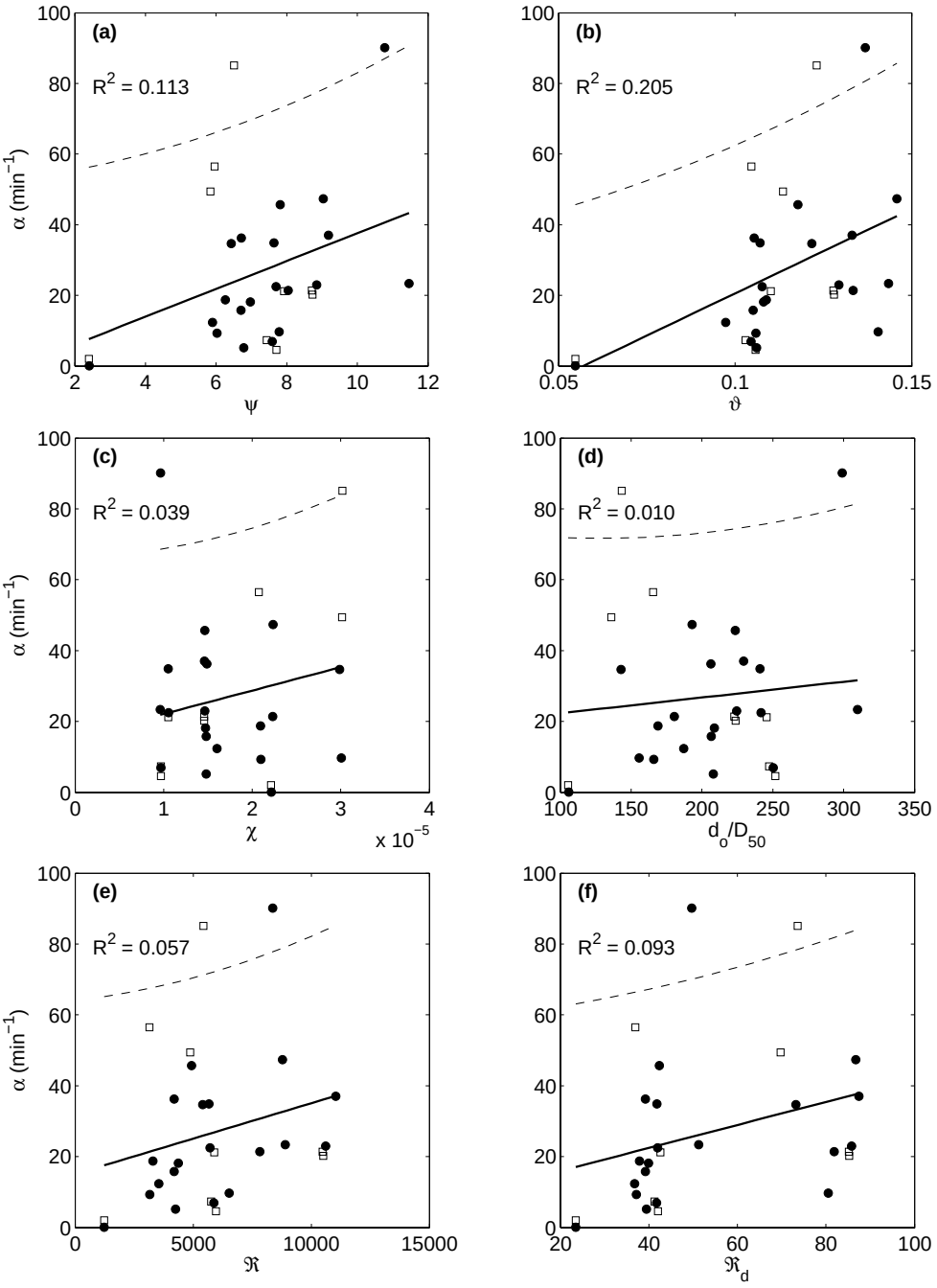

Figure 6.10 Linear-linear relationships for the evolution rate against six dimensionless parameters. The filled circles represent growth tests while the open squares represent transition tests. The bold line is the straight line of best fit, while the dotted lines indicate the 95% confidence intervals of the fit.

Table 6.2 Fits achieved for the functional dependence of the evolution rate.

Dimensionless	Linear-Linear Fits			Log-Log Fits		
Parameter	Slope	Offset	R^2	Exponent	Multiplier	R^2
ψ	3.938	-1.802	0.113	3.57	1.48×10^{-2}	0.502
ϑ	478.1	-27.25	0.205	5.79	$5.11 \times 10^{+6}$	0.583
χ	660030	15.50	0.039	-0.24	$1.04 \times 10^{+0}$	0.003
d_o/D_{50}	0.044	17.85	0.010	2.76	6.98×10^{-6}	0.189
$\Re$	0.002	15.08	0.057	1.97	7.13×10^{-7}	0.392
$\Re_d$	0.324	9.458	0.093	2.36	1.51×10^{-3}	0.289

estimate the evolution rate from the flow and sediment parameters with low correlations between the evolution rate and the non-dimensional parameters being calculated. The best fit, with the maximum correlation coefficient, is achieved by using the skin friction Shields parameter ($R^2 = 0.205$), however, this value of R^2 is very much lower than unity. Hence, it was concluded that there was little benefit of pursuing linear relationships for the evolution rate.

Figure 6.11 shows the log-log relationships between the evolution rate and the six non-dimensional numbers listed in Tables 3.2 and 3.4. As with the previous figure, in Figure 6.11 the filled circles represent growth tests, while the open squares represent transition tests. The bold line is the least squares straight line fit to the log of each variable, while the dotted lines indicate the 95% confidence intervals of the straight line fit in log-log space.

Once again there is appreciable scatter in the data sets with a wide spread of the confidence intervals about the linear fit lines. However, taking the log of the variables has improved the overall fit to the data sets with generally higher correlation coefficients being recorded for all variables. The two dimensionless parameters that achieve the highest correlations are the mobility number ($R^2 = 0.502$) and the skin friction Shields number ($R^2 = 0.502$). Table 6.2 presents a summary of the fits achieved in Figures 6.10 and 6.11. The slope and offsets were determined from the straight line fit in linear space while the exponent and multiplier were calculated from the slope and offset of the straight line fits undertaken in log space.

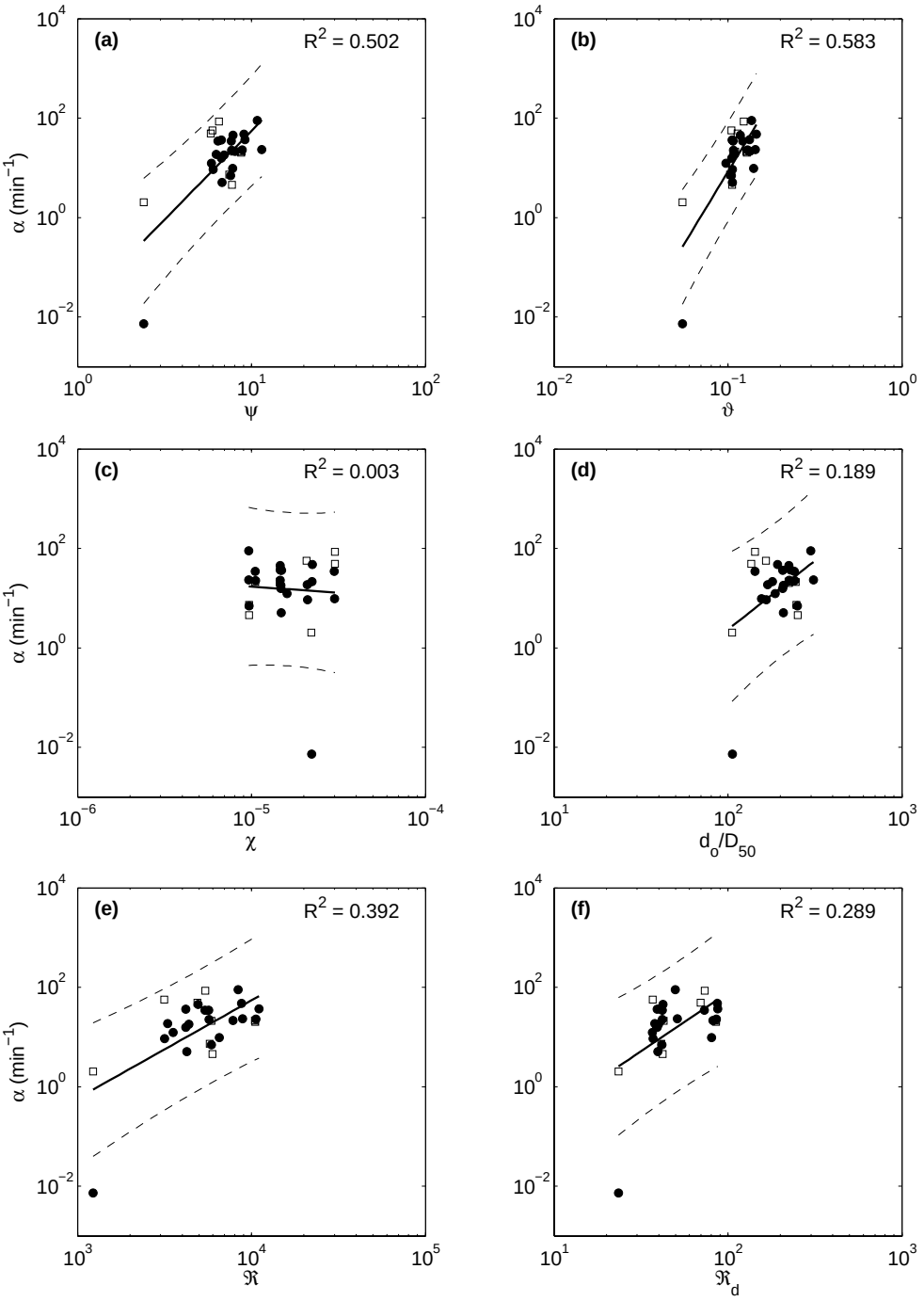

Figure 6.11 Log-log relationships for the evolution rate against six dimensionless parameters. The filled circles represent growth tests while the open squares represent transition tests. The bold line is the straight line of best fit, while the dotted lines indicate the 95% confidence intervals of the fit.

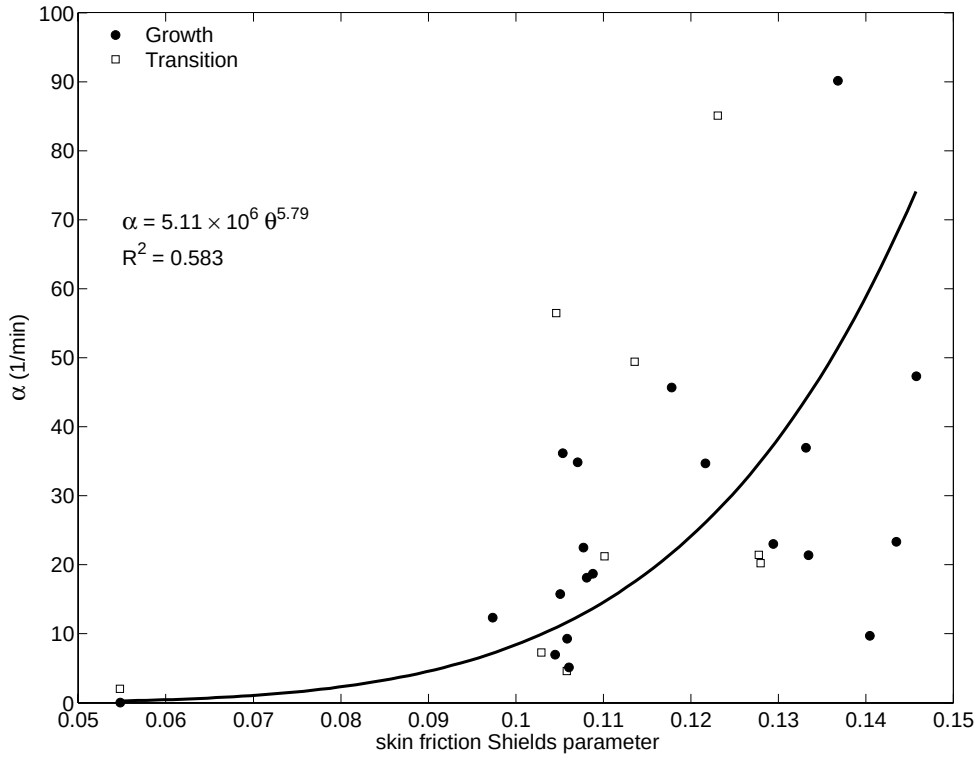

Figure 6.12 Relationship between the evolution rate and the skin friction Shields parameter. The filled circles represent growth tests while the open squares represent transition tests.

As can be seen in Table 6.2, of the six fitting parameters the log-log relationship of the skin friction Shields parameter (ϑ) provided the best correlation with the evolution rate. Figure 6.12 shows the log-log relationship developed between the evolution rate and the skin friction Shields parameter in linear-linear space.

There is a significant correlation ($p < 0.01$) in Figure 6.12 between the Shields parameter and the evolution rate, however, as discussed above the correlation was low with large experimental scatter shown in the data set. From the log-log relationship the evolution rate can be calculated as a function of the skin friction Shields parameter using the following relationship:

$$\alpha = 5.11 \times 10^6 \vartheta^{5.79} \tag{6.5}$$

This function shows that increasing the Shields parameter by a small amount will cause the rate of ripple evolution to increase at a substantially higher rate, which intuitively is

what would be expected (i.e a flow with greater energy relative to the energy required to move sediment particles would form a rippled bed faster than a flow with a lower flow energy).

A major conclusion to be drawn from the figures presented in this section is that there is no appreciable difference between the evolution rate determined from the growth tests and the transition tests. This indicates that ripple growth and transition can be considered to be the same process which is adequately modelled by the non-linear differential Logistic equation (equation 6.1).

6.4 SUMMARY AND DISCUSSION

This chapter has presented a new method that uses the spectral density function of small scale wave-formed rippled sediment beds to model the changes a rippled bed undergoes as it is actively evolves between two given equilibrium states due to a change in surface wave conditions. A ripple evolution model was developed from the well known Logistic growth law. Using this growth model, changes in the spectral energy level of the bed can be thought of as a balance between the processes which act to build up the bed and the processes which act to flatten a bed. Fitting the general solution of the Logistic non-linear differential equation to the experimental data enabled the evolution rate of the bed to be determined for each experimental test. A major conclusion of this chapter is that there is no appreciable difference between the evolution rate determined from the ripple growth tests and the ripple transition tests. This indicates that the two types of temporal change are special cases of the same evolution processes which are driven by the ratio of kinetic fluid forces over inertial sediment forces. A functional dependence was established between the ripple evolution rate and the Shields parameter. This allows the evolution rate to be estimated from flow and sediment properties.

As shown in Section 6.1, ripple forms do not develop uniformly over a sediment surface under the action of irregular surface waves, but initially appear as patches of ripples that merge together over time. The location where ripples will start to develop is impossible to estimate because of the heterogeneous nature of sediment beds and the random

fluctuations of flow properties under irregular surface waves. How quickly these patches of ripples merge and develop into a fully developed rippled bed will be dependent on the flow and sediment properties. Hence, current methods to parameterise rippled beds based on a single value for the ripple height and length will be prone to errors in situations where the rippled bed is actively growing from a no-ripple condition. A more complete way to describe transient rippled beds is to parameterise the whole bed in terms of its spectral density function. Changes in ripple parameters at one location of the bed do not determine the parameters for the whole bed, but are averaged out across a given area of the bed. This allows the spatial variability in ripple properties to be factored into the transient analysis of rippled beds.

Ripple transition experiments undertaken as part of this study could only focus on very small scale long crested ripples that were generated under a narrow range of surface wave conditions. This meant that rippled beds only evolved between two states that were in the same order of scale and that the ripple profile was only changing along the axis of the wave propagation. This was not seen as a constraint to the future application of the ripple evolution model to any given rippled bed that is in the process of actively changing between two equilibrium states. Recently *Lyons et al.* [2002] (refer to Section 2.3.2) described a method to characterise an area of the seafloor in terms of its two-dimensional spectrum. As is the case with estimations of the significant wave height from the water surface spectrum the area under the non-dimensional ripple spectrum could be calculated just as easily from a two-dimensional ripple spectrum instead of the one-dimensional spectrum as done in this study. However, to adequately non-dimensionalise a ripple spectrum calculated from an area of the sediment bed containing so called three-dimensional ripple forms would require the understanding of the formation mechanisms for these types of beds to be substantially improved. *Traykovski et al.* [1999] observed rippled beds, containing two very different scales of ripples, actively changing between energy states due to a change in the surface wave conditions at the LEO-15 site. From a spectral point of view this would give a double peaked spectral plot. Side scan sonar plots presented in *Traykovski et al.* [1999] showed smaller ripples growing on top of large older remnant

ripples. As the newer ripples developed the older ripples disappeared which suggests that there was a redistribution of spectral energy from low to high spatial frequencies in the spectral density function of this bed. As the spectral energy shifted, the total energy of the bed would certainly have changed and it is this change in spectral energy that the ripple evolution model seeks to describe. Hence, the application of the ripple evolution model is not constrained by the limited scale of measurements undertaken during this study.

The ripple evolution model described in Section 6.3 shows that the evolution of a rippled bed between two equilibrium states can be described mathematically in exactly the same way as a rippled bed growing from a no-ripple condition. There is no difference in the experimentally determined values of the evolution rate calculated from the ripple growth tests and the ripple transition tests (refer to Figures 6.11, 6.10 and 6.12). Through the use of equation 5.9 the non-dimensional spectral energy of the equilibrium rippled beds can now be estimated, while the rate at which these beds will change can be determined from the flow and sediment properties via equation 6.5. This allows the bed to be modelled with time, evolving between any two equilibrium states if the flow conditions and sediment properties are known.

Prior to the evolution model, described in Section 6.3, being applied in an operational wave forecasting model a number of practical issues need to be resolved or researched further. The most obvious issue is the estimation of the initial and final energy states of the sediment bed. An estimation method for the equilibrium non-dimensional ripple spectrum from flow conditions and sediment parameters was presented in Section 5.2.2. The application would proceed in much the same way as current moveable bottom roughness models proceed. At the end of each time step, in a transient wave model, a new bed configuration would be estimated based on the flow conditions and sediment bed properties calculated at the previous time step. However, there would not be the underlying assumption that the ripple field is in constant equilibrium with the wave field as is the case with current movable bed roughness models [*Tolman*, 1995]. Based on the flow conditions and time step length the ripple parameters and hence the bottom roughness height would scaled back from equilibrium values. This would allow the rippled bed to be modelled

more realistically as the simulation proceeds. Another issue in applying the ripple evolution model is the determination of a starting value for the non-dimensional spectral energy in the simulation. If the value of the initial state of the bed is set to zero, then equation 6.3 predicts zero energy for all subsequent values of t. Hence an initial value of E_o is required by the approach. In the current study the value of the non-dimensional spectral energy for the sediment beds in a no-rippled state were in the order of 10^{-4} which were generally an order of magnitude lower than the final states, hence, a similar small value could be used to start a modelling simulation from which the simulation would ramp up.

Issues such as bioturbated beds [*Wheatcroft*, 1994] could be incorporated into the evolution model by estimating the background spectral energy of such beds. If wave conditions were so low as not to cause the bed to evolve then the rate at which benthic organisms rework the bed could be incorporated into the analysis. *Amos et al.* [1988] suggests that benthic organisms will degrade rippled beds to a *flat* bed condition within 4 to 6 hours.

The next step forward would be to develop the evolution model into a full two-dimensional model which would incorporate a dependence on the peak surface wave direction. However, issues such as the isotropic nature of bioturbated or *flat* sediment beds would have to be factored into the analysis. As wave-formed ripples develop the sediment bed changes from isotropic to anisotropic in nature [*Briggs et al.*, 2002].

The estimation of the rate at which rippled sediment beds evolve under a variable sea state has the potential of leading to significant improvements in the way rippled beds evolve and hence how the bottom roughness is approximated in coastal wave models.

Chapter 7
Conclusions and Recommendations

This thesis presents an experimental based research project that investigated the spatial and temporal variation of wave-formed rippled beds. This chapter highlights the conclusions reached during this study and discusses a number of recommendations for future work in this field.

7.1 CONCLUSIONS

The work completed on the analysis of wave-formed sediment ripples using a spectral approach can be classified into three related categories: the spectral description and parameterisation of wave formed rippled beds; the prediction of the equilibrium ripple spectrum from flow conditions and sediment bed properties; and the description of the evolution of rippled beds as they are moving between equilibrium states. Conclusions for each of these categories are presented in this section and relate to the three result chapters of this thesis.

7.1.1 Rippled Bed Parameterisation

A new method was presented to parameterise wave-formed rippled beds in terms of their spectral density function so that the observed spatial variation of ripple parameters can

taken into account in ripple prediction and modelling applications. From the work undertaken in Chapter 4 the following conclusions were drawn:

- Traditional ripple prediction methods have a bias towards ripples formed under medium mobility conditions. At higher and lower mobility conditions ripples will be inherently variable with a distribution of ripple parameters existing on a given bed;

- The spectral method worked well for the data sets measured during this study. However, the selection of the banding frequencies was somewhat arbitrary and was based on a prior guess as to the value of the ripple's spatial frequencies. If the spectral method were to be applied to other data, especially field data, then some preprocessing of the data to set the banding frequencies would be necessary;

- The observed trends in ripple spectra formed under different flow conditions and on different beds were found to agree with the general theory of wave-formed ripple prediction;

- No definite dependence was found between the width factors derived from the ripple spectra of the 40 equilibrium surfaces scanned, and six of the more widely used non-dimensional numbers. A slight dependence was found between the peakedness parameters derived from the spectra and the non-dimensional numbers. The use of these two spectral parameters did not provide any useful application in the description of the ripple spectrum.

7.1.2 Rippled Bed Prediction

Two methods were introduced to predict wave formed rippled beds, from flow conditions and sediment properties, in terms of their spectral density function. From the spectral prediction methods presented in Chapter 5 the following conclusions were drawn:

- Directly comparing the water and the ripple surface spectra failed to produce a reliable functional dependence to predict the ripple spectrum. Higher level spectral

functions such as the cross spectral density and transfer functions were attempted, but also proved to be inadequate;

- The use of a non-dimensional form to describe the ripple spectrum provided an effective method to develop a functional dependence between the flow conditions, sediment bed properties and the ripple spectra;

- The non-dimensional method was compared with two more established ripple prediction methods and was found to be able to model small scale ripples with the same degree of accuracy as previously developed methods. However, based on a comparison of the method against widely accepted trends of ripple parameters at higher ripple scales it was found that the spectral method failed to predict these trends at larger ripple scales;

- The non-dimensional spectral method worked well over the range of experimental conditions that could be simulated during this study. However, there is little advantage in using the spectral method to predict ripple parameters under steady state flow conditions such as those generated in this area of the study. The strength of the spectral method lies in modelling evolving rippled beds as is done in the ripple transient chapter.

7.1.3 Ripple Bed Transients

A new method was derived that utilised the ripple spectrum to model the changes a rippled bed undergoes as it actively evolves between two given equilibrium states due to a change in surface wave conditions. From the spectral evolution model presented in Chapter 6 the following conclusions were drawn:

- Ripple forms do not develop uniformly over a sediment surface under the action of irregular surface waves, but initially appear as patches of ripples that merge together over time. Hence, current methods to parameterise rippled beds based on a single value for the ripple height and length will be prone to errors in situations where the rippled bed is actively growing from a no-ripple condition;

- Based on the observations of rippled beds undertaken during this study, it has been determined that rippled beds display two stages of development as they are in the process of evolving to a new equilibrium state, with a point of inflection in the growth curve located between the two stages;

- The evolution of a rippled bed between two equilibrium states can be described mathematically in exactly the same way as a rippled bed growing from a no-ripple condition. This allows any bed to be modelled with time evolving between any two equilibrium states if the flow conditions and sediment properties are known;

- There was no appreciable difference between the evolution rate determined from the ripple growth tests and the ripple transition tests. This indicates that the two types of growth are special cases of the same evolution processes which are driven by the ratio of kinetic fluid forces over inertial sediment forces;

- The ripple evolution rate and the Shields parameter were found to be correlated, but there was a substantial scatter in the two data sets. Hence the confidence in this functional dependence was low.

7.2 RECOMMENDATIONS FOR FUTURE WORK

It has to be emphasised that this body of research represents a first step in regards to using spectral methods to parameterise, predict and model wave-formed rippled beds and has been developed on only a relatively small data set with a limited range. There is a substantial amount of work to be completed before a general modelling approach that encompasses all ripple species found in shallow seas can be developed. Hence, this study proposes the following recommendations for future study:

- The spectral method was able to predict equilibrium ripple beds at small scales, but at larger scales further research needs to be undertaken on refining the fitting parameters of the empirically derived spectrum;

- More data, similar to that measured in this study, needs to be obtained under laboratory conditions and in the field. Measurements of this type would enable a better understanding of the variability of ripple parameters to be gained;

- The selection of the banding frequencies, to filter the lower frequency trends out of the spectrum, was somewhat arbitrary and was based on a prior estimate of the value of the ripples spatial frequencies. An improved method needs to be developed that is able to calculate the value of these banding frequencies more concisely so that larger ripple forms maybe analysed;

- The non-dimensional form of the ripple spectrum was based on the peak orbital diameter and the 50 percentile grain size diameter. A method is required that uses the bottom velocity spectrum and the distribution of the grain size in the spectral prediction method. In using these distributions the overall variability of the ripple generation mechanisms would be able to be taken into account;

- More work is required to determine the relationship between the ripple and surface wave spectra. It is felt that there should be some type of transfer function between the two linked spectra which is able to be exploited to predict the ripple spectrum more efficiently;

- The initial spectral energy of a rippled bed in a no-ripple state needs to be investigated further. This study assumed the initial state of the bed had a non-dimensional spectral energy in the order of 10^{-4} which was generally one order of magnitude lower than the fully developed rippled beds;

- Further research is required on bioturbated beds to determine the value of the spectral energy that is typical of these beds and to determine how fast these beds are likely to form after the onset of a calm period;

- More measurements are required to refine the prediction of the evolution rate rippled beds display with time. These measurements would allow a functional dependence between the ripple evolution rate and the Shields parameter to be developed

with a higher degree of confidence;

- The next step forward would be to develop the evolution model into a full two-dimensional model to incorporate a dependence on the peak surface wave direction. However, issues such as the isotropic nature of bioturbated or *flat* sediment beds would have to be researched further;